EXPERIMENTS ON AND WITH BACKSCATTERING INTERFEROMETRY

By

Stephen S. Dotson

Dissertation

Submitted to the Faculty of the

Graduate School of Vanderbilt University

in partial fulfillment of the requirements

for the degree of

DOCTOR OF PHILOSOPHY

in

Chemistry

May, 2008

Nashville, Tennessee

Approved:

Professor Darryl Bornhop

Professor Brian Bachmann

Professor David Cliffel

Professor Richard Haglund

To my parents who have provided me with everything I could ever need and to the rest of my family who have always been there for me.

ACKNOWLEDGEMENTS

This work was funded by NASA, Vanderbilt University, and NIH. I would like to thank my committee member for guidance and support. I am especially grateful to Dr. Bornhop for continually pushing me to accomplish more. Many former and present Bornhop group members have been very helpful in the advancement of this work. The fun times we shared as a group have been some of the most memorable of my life. Finally, I am grateful for my family for the support they have given me.

TABLE OF CONTENTS

Page

Chapter

LIST OF TABLES

Table Page

LIST OF FIGURES

LIST OF ABBREVIATIONS

RI	refractive index
PC-WG	photonic crystal waveguide
BSI	backscattering interferometry
LBA	laser beam analyzer
CCD	charged coupled device
HPLC	high-performance liquid chromatography
PDMS	poly(dimethyl)siloxane
FFT	fast Fourier transform
FT	Fourier transform
HEPES	(4-(2-Hydroxyethyl)piperazine-1-ethanesulfonic acid)
GUI	graphical user interface
LV	LabVIEW™
NI	National Instruments™
P	proportional
I	integral
D	derivative
CC	cross correlation
2D	two dimensional
ROI	region of interest
He-Ne	helium-neon (laser)
PEEK	polyetheretherketone

ee	enantiomeric excess
CPD	capillary polarimetric detector
DOCP	direct on-chip polarimetry
PAL	phenylalanine ammonia lyase
SOCP	side scatter on-chip polarimetry

CHAPTER I

REVIEW OF INTERFEROMETRY

1.1 Basics of Interferometry

Interferometry is the constructive and destructive interference of waves and the detection of differences between them. Interferometry is observed in any kind of waves including sound waves, light waves, and ocean waves. Interference can be visualized as adding waves together. Simple waves can be described by the number of cycles in a given time (frequency), size (amplitude), and alignment to a starting point (phase), see Figure 1.1[1,2].

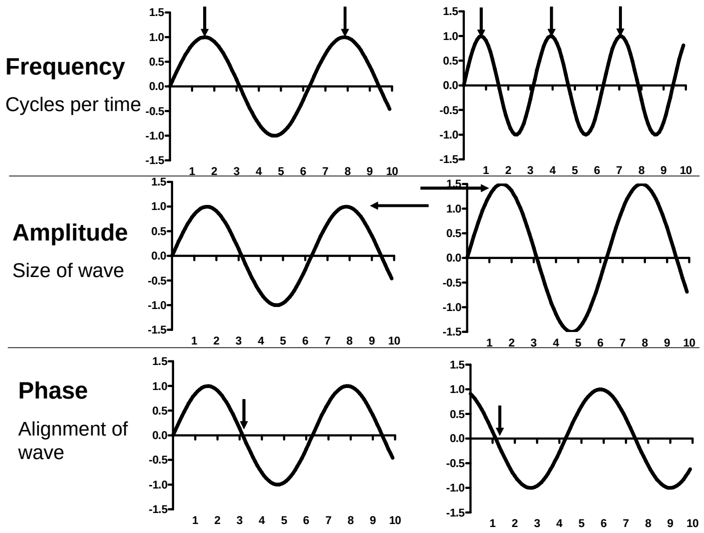

Figure 1.1. How harmonic waves are defined: frequency, amplitude and phase

The constructive and destructive interference of waves is dependent upon the frequency, amplitude, and phase of the waves. Figure 1.2 shows the constructive interference of two waves

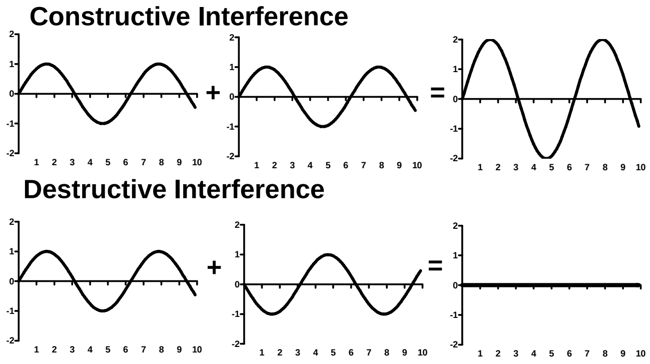

Figure 1.2. Constructive and destructive interference

that have the exact same frequency, amplitude, and phase. The two waves combine to form one wave with the same frequency and phase but with higher amplitude. Figure 1.2 also shows the destructive interference of two waves with the same frequency and amplitude but with different phases. The two waves completely cancel each other resulting in a flat line[1,3].

An interferometer typically takes a wave and splits it into two or more coherent (same amplitude, frequency, and phase) parts, which then travel different paths and are combined to produce an interference pattern. The interference pattern is dependent upon any factor that changes the phase of the wave, such as change in path length or refractive index (RI), which is a measure of the speed of light in the traversed medium. The early interferometers utilized white light sources, but modern interferometers typically utilize monochromatic sources, such as lasers[3,4].

1.2 Types of Interferometers

Several variations of interferometers have been created. Each utilizes some method to split the light source and then recombine the two waves. There is also the requirement of detection, or viewing of the pattern, in order to obtain information from the interference pattern.

1.2.1 Young Interferometer: Double-Slit

One of the earliest interferometers was the double-slit interferometer. A light source is shown onto a thin plate with two slits. As the waves spread out from the two slits, the light produces an interference pattern which is observed by a detector. Several factors change the appearance of the interference pattern including the distance between the slits, wavelength of light, and the distance to the detector.

A Young interferometer configuration splits a laser into two separate waveguides. Waveguides transmit light because there is a large difference in RI between the waveguide material and the media outside. The light escapes from the ends of the two waveguides and interacts to produce an interference pattern. The waveguide interferometer has two methods of measuring RI changes in samples. As shown in Figure 1.3, either 1) a flow cell can be placed at the waveguide exit which allows light to pass through the samples then form the interference pattern or 2) the flow cell is attached to or integrated into the surface of one of the waveguides. The second approach allows interaction of samples with the evanescent field of the light which couples out of the waveguide depending on the relative refractive indices of the waveguide and the sample (or outer surface). Integrated optic double-slit interferometery has been utilized to measure changes in RI in water and sugar solutions. RI changes in N_2 and CO_2 gases have also been monitored using this instrument. Resolution of about 10^{-5} RIU has been reported for this system[5].

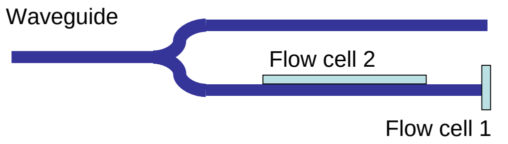

Figure 1.3. Waveguide with two different flow cell locations shown

1.2.2 Four Channel Young Interferometer

A four channel Young interferometer was constructed to allow for the simultaneous and independent monitoring of three processes. In this interferometer a laser beam is split into four independent paths that then escape the device to create an interference pattern. The microchannel device has four independent channels, allowing molecules to be immobilized on the surface and the binding events monitored. The interference pattern is captured by a CCD array[6].

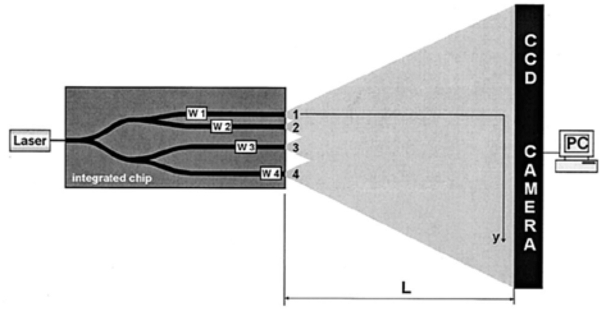

Figure 1.4. Four channel Young interferometer[6]

With a four channel system, the changes in the interference pattern are based on the interaction of light of all four channels. In order to acquire the information of the three channels independently (utilizing the fourth channel as the reference), the microchannel device must be properly designed. By spacing the outputs of the channels appropriately and positioning the detector at the proper distance, each channel has a unique spatial frequency that can be transduced by the camera. A Fourier transform can be utilized to monitor the three spatial frequencies, allowing for independent and simultaneous measurements of three separate samples[6].

Glucose solutions were chosen to analyze the 3-channels system so that a known RI change could be monitored. RI changes of 0.8 and 1.6 x 10^{-3} RIU were introduced into the system, in all three channels, demonstrating that the three channels produced similar results. Resolution of 8.5 x 10^{-8} RIU was observed. Long term stability measurements were about 5 times the resolution or 4.3 x 10^{-7} RIU[6].

1.2.3 Farfield Sensor

The Farfield sensor is based on a Young interferometer, however as shown in Figure 1.5, instead of two slits, the light source is split into two waveguides, providing both sensing and reference paths. As the light escapes the end of the waveguides, it diverges, interferes and creates an interference pattern. Materials placed onto the surface of the sensing waveguide cause a change in coupling efficiency by changing the RI interface, altering the path the light travels down the waveguide, modifying the interference pattern[7].

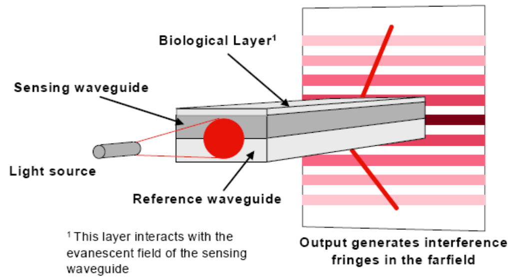

Figure 1.5. Farfield Sensor[7]

Sucrose solutions and water with a 1 x 10^{-3} RIU change were analyzed utilizing a Farfield sensor. A noise value of 3.6 x 10^{-7} RIU was measured. The effectiveness of the sensor in water is low since the sensor is designed for biological applications and surface measurements. Resolution for films like proteins was reported to be 1.5 x 10^{-7} RIU[8]. Water and isopropyl alcohol (IPA) were exchanged 10 times and a reproducibility of 8 x 10^{-6} RIU (1 σ) was reported[9].

Biotin-streptavidin is a well known binding pair that serves as a biological assay used to test many biosensors. The Farfield sensor has been utilized in the analysis of this pair by immobilizing biotin onto the surface of the sensor. Streptavidin is then introduced binding to the biotin, changing the surface mass and RI allowing the affinity of the binding to be measured. By using a streptavidin modified surface and biotinylated antibodies or antigens the sensor serves as an immunoassay system. The biotin-streptavidn binding was measured as a 50 picometer change in thickness with resolution better than ±0.01nm[10]. Human chorionic gonadotropin (hCG) binding has also been demonstrated with this technique[11].

The binding of calcium to transglutaminase was also performed with the Farfield sensor (AnaLight® Bio200). Transglutaminase was immobilized onto the sensor and $CaCl_2$ and NaCl were introduced. After the bulk RI changes (signal changes caused by the $CaCl_2$ and NaCl solution, not binding) were removed, the sensor showed binding specificity for $CaCl_2$, and no response from control (NaCl). The experiment was performed with several different concentrations of $CaCl_2$ allowing for the calculation of the affinity at 1.72 mM[10].

1.2.4 Mach-Zehnder Interferometer

The Mach-Zehnder interferometer uses an optical source which is directed at a beam splitter, creating two paths. The first light path travels to a mirror then to a second beam splitter where the two light paths combine and are then directed to a detector. The second light path is directed onto a mirror, then passes through a small sample, combines with the first light path at the beam splitter, and then proceeds to the detector. When no sample is present, the two waves have the same phase. However, when a sample is added a phase change occurs in the second beam path, resulting in a change in the interference pattern. The Mach-Zehnder interferometer has been used for RF modulators and optical switches.

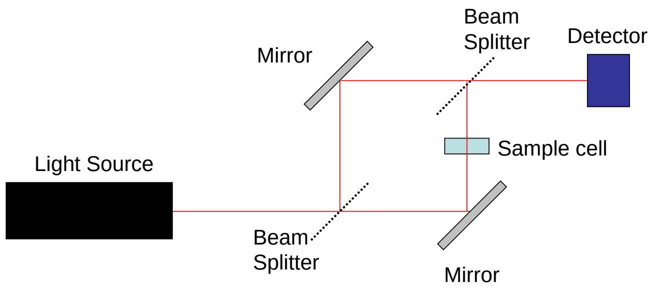

Figure 1.6. Mach-Zehnder Interferometer

The Mach-Zehnder interferometer was modified by the addition of an integrated optic. Light is split in the optic, with the two parts traveling a distance before being recombined. One path serves as a reference arm. Solutions are placed on the sample arm to be analyzed. RI resolution was determined at 5 x 10^{-8} RIU and long-term stability was calculated at 10^{-7} RIU[12].

A Mach-Zehnder interferometer was designed to allow the analysis of molecular binding. A waveguide chip with microfluidic channels was created where light was split in two channels and then recombined. A biotin layer was placed on the surface of the chip allowing for binding of streptavidin to be monitored by interferometry. Streptavidin was introduced into the channel and binding between the streptavidin and biotin was monitored[13].

1.2.5 Fabry-Perot Interferometer

The Fabry-Perot interferometer consists of two parallel highly reflecting mirrors, which allows for wavelength selection based on the distance between the mirrors. Transmission wavelength of the interfereometer corresponds to the wavelength of light resonating between the mirrors. The Fabry-Perot interferometer can be created in an optical fiber and has been used to sense temperature, vibration, acoustic waves, ac voltage, and magnetic fields. High sensitivity can be accomplished by utilizing long length fibers[14]. Fabry-Perot interferometry is the most common type of laser cavity.

1.2.6 Spinning-Disk Interferometry based on Far-Field Interferometry

A technique called spinning-disk interferometry utilizes far-field interferometry to monitor samples on a fabricated BioCD. Far-field (Fraunhofer) diffraction occurs when the source and observation point are at infinity. By positioning the detector a large distance from the source, it is possible to observe the interference pattern as far-field. Far-field diffraction is important in determining the nature of flaws in optics[3]. The BioCD is mounted on a photoresist spinner and a helium neon laser is focused onto the BioCD. The far-field diffraction is directed onto a photodetector. A digital oscilloscope measures the signal from the photodetector, which monitors the intensity of the far-field diffraction[15]. The BioCD is a silicon wafer and has gold ridges in a spoke pattern with a thickness of 79.1 nm ($\lambda/8$ for a He-Ne laser). The interference pattern is generated by the interaction of the reflection of light off the gold surface and the mirrored surface of the silicon wafer[16].

Antibodies are easily immobilized onto the gold ridges. When bovine serum albumin (BSA) is immobilized onto the surface of the gold, there is a decrease in the intensity of the far-field diffraction. Anti-mouse IgG was bound to the BioCD and then part of the disk was exposed to the mouse IgG and the other part BSA. The mouse IgG showed binding while the BSA produced no significant change[16].

1.2.7 Waveguide Spectroscopy

Total internal reflection is a principle that is utilized in waveguides, such as fiber-optics. By choosing a waveguide with the appropriate thickness compared to the wavelength of light to be used, the number of internal reflections can be as high as 10^3-

10^4 reflections. Waveguide interferometry utilizes changes in the physical structure of the waveguide by adsorption of proteins to the surface[17].

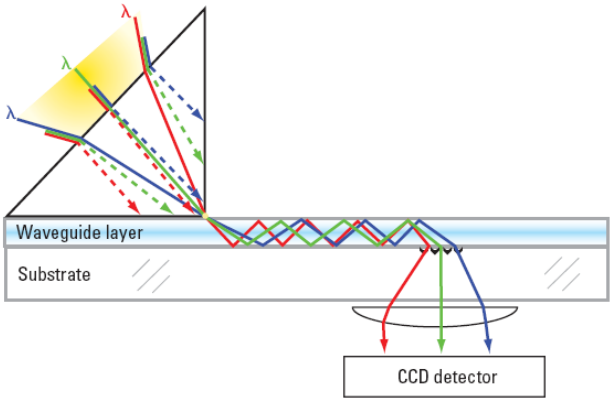

Figure 1.7. Waveguide spectroscopy[17]

A single wavelength system is more sensitive than a broad-band, but requires correct angular alignment. Broad-band systems can provide information about physicochemical properties. A xenon lamp was used to measure horse-heart cytochrome c adsorbed onto the waveguide surface[17].

Two helium-neon lasers (543.4 and 632.8 nm) were aligned with the xenon lamp and simultaneously emitted into the waveguide. Again cytochrome c adsorbed onto the surface was measured. The addition of lasers produced an improvement in bandwidth and performance of the instrument[17].

1.2.8 Photonic-Crystal Waveguide (PC-WG) Biosensor

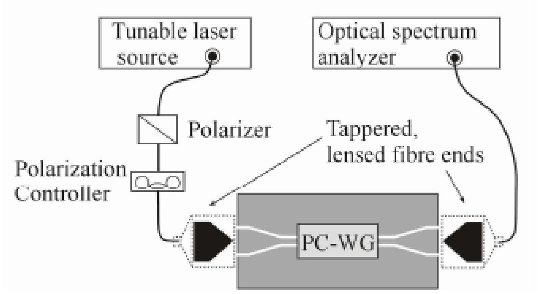

Figure 1.8. Photonic-crystal waveguide[18]

A photonic crystal (PC) has a given bandwidth of light which can be passed through the waveguide. A tunable laser source passes light through the PC-WG and then an optical spectrum analyzer measures the transmission. For a given sample, the drop-off in transmission is dependent on the RI. The PC-WG is fabricated using a silicon-on-isolator wafer and adding a silicon layer with air holes on the wafer[18].

Solutions of water and two oils (RIs of 1.33, 1.48, and 1.518) were measured using the PC-WG. Sample volumes of 6 μL were applied to PC-WG. Cutoff frequencies compared well to simulated data. Bovine serum albumin (BSA) was also introduced into the system. Concentrations of 10 μM and 1.5 μM were measured with the PC-WG. Water was reintroduced into the system after the BSA and the signal from the BSA remained, demonstrating that the protein was adsorbed onto the surface[18].

1.2.9 Backscattering Interferometry

Backscattering interferometry (BSI) is a powerful technique that monitors change in RI of liquids in small volumes such as capillaries or microfluidic chips. BSI is a unique tool (shown in Figure 1.9a) consisting of a laser, a fluidic container (either capillary or microfluidic chip), and detector. The beam produced by the laser is directed onto the fluidic cavity covering the width of the fluidic channel producing a fringe pattern

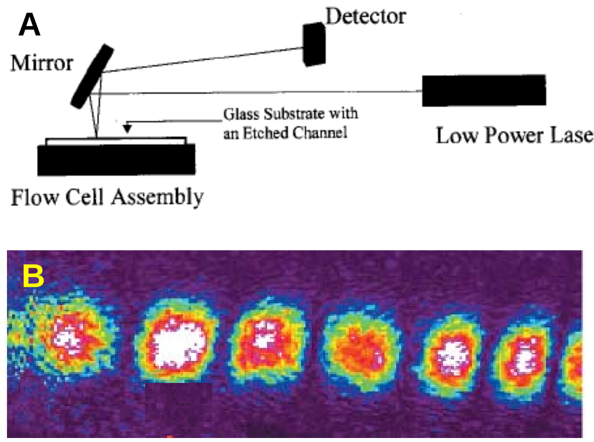

Figure 1.9. A) Block diagram of chip BSI system B)False color image of fringe pattern[19]

(Figure 1.9b), a series of bright and dark spots, in a plane 360° around the fluidic container. The power of BSI is the ability to detect small RI changes in the fluidic channel by monitoring the shift in the fringe pattern[19].

To try to demonstrate how the fringe patterns are created and provide high sensitivity, a number of modeling techniques have been utilized[20-24]. The fringe pattern is produced by the reflection and refraction of light from each optical surface and the constructive and destructive interference of the light. Figure 1.10 shows a model with a trace of three rays on a cross section of a capillary. Using only three input rays, limited to three splits each, the escaping arrays produced (arrows from the capillary) are in several different directions and pass through the sample fluid (center of the capillary) many times[22]. Refraction at the optical interface changes as the RI of the sample change causing the fringe pattern to shift. Fringes produced in capillaries have shown the detection of RI changes at the 10^{-7} RIU level with a simple slit and photodetector[19].

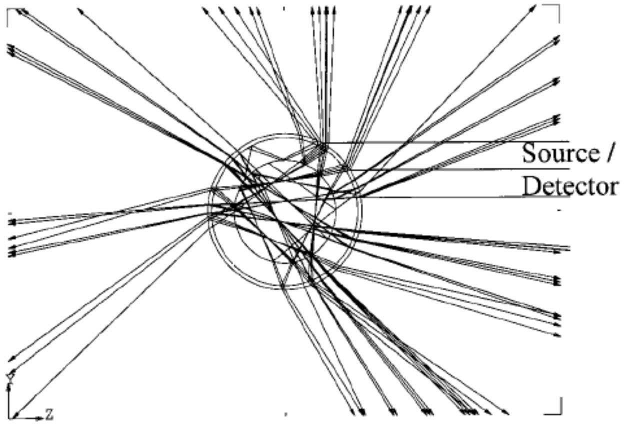

Figure 1.10. Trace of three rays on a capillary[19]

BSI serves as a universal detector, which means that any perturbation in the system that produces a RI change will also produce a signal, which requires the control of temperature to a certain degree, since a change in temperature will produce a change in RI (for water 1.0×10^{-4} RIU/°C)[25]. A temperature controller is used to drive a thermoelectric cooler, based on the resistance readings of a thermistor, which allows the operator to not only control temperature, but also to generate calibration curves based on temperature[26].

Detection Methodologies

One of the most important aspects of BSI is how the fringe position or shift is determined. Several different methods have been employed each with limitations. The same capillary configuration was utilized in order to compare the detection limits of each shift calculation methodology.

Using a CCD camera with a laser beam analyzer (LBA) allows the operator to image an entire section of the fringe pattern. Shift of the fringes can be determined from the resulting images. Using the CCD and LBA, the detection limits were 5 x 10^{-5} RIU. Detection limits can be improved to 6.7 x 10^{-6} RIU by utilizing minimum tracking to monitor the fringe shift[20,27].

A bicell is a detector containing two rectangular photodiodes separated by a small gap and the output from both photodiodes are monitored. When the fringe pattern is centered on the bicell, the output from the two photodiodes is equal. When the fringe pattern shifts, one photodiode will see an increase in intensity while the other sees a decrease. Any intensity fluctuation of the laser is the same in the two photodiodes. Using the equation $S = (A-B)/(A+B)$, the signal for BSI is calculated. Detection limits of 4 x 10^{-6} RIU are calculated with the bicell detector. One limitation of the technique is that the there is a finite amount that the fringe can move before the bicell signal is nonlinear[27].

One major advancement to BSI was the use of a linear CCD array to obtain a line profile of several fringes. By aligning the detector in the correct region of the fringe pattern, so that the fringes appear sinusoidal, it was possible to perform a Fourier transform and determine the positional shift of the fringe pattern. As the fringe pattern shifts, the frequency of the fringes remains the same. By locking in on the frequency of the fringe it is possible to monitor the phase change and measure the shift of the fringe pattern. The Fourier technique provides an easy method of determining fringe shift with improved detection limits of 7 x 10^{-8} RIU[27]. Table 1.1 shows a summary of the detection methodologies [27].

Table 1.1. Comparisons of 3σ detection limits for different interrogation methods in BSI

Fringe Interrogation Method	**Detection Limits, RIU**
Bicell	4 x 10^{-6}
Slit-photodetector w/reference arm	1.5 x 10^{-7}
CCD/LBA	5 x 10^{-5}
CCD array w/minimum tracking	6.7 x 10^{-6}
CCD array w/ Fourier phase detection	7 x 10^{-8}

Capillary Applications

Capillary BSI has been utilized as the detector in several applications including electrophoresis, HPLC, and flow measurements. BSI was utilized to measure the separation of four cations (K^+, Ba^{2+}, Li^+, and Na^+)[28], three carbohydrates (Maltose, Lactose, and D-Ribose) with detection limits of tens of micromolar[29], three dyes (Bromothymol Blue, Thymol Blue, and Bromocresol Green)[29], and even the concentration of caffeine in several common beverages [29]. BSI has also been utilized as a detector for packed capillary high-performance liquid chromatography (HPLC) with detection limits of the samples in the picomolar range[30]. A non-invasive flow measurement technique in capillaries was developed utilizing an IR laser with a shutter to introduce a pulsed heated plug in a flowing stream. BSI was used to monitor temperature from the plugs as they pass through the probed region. Flow rates of 1 to 10 μL/min were measured with detection limits of 42.8 nL/min[31].

In order to enhance the sensitivity of BSI, a sample and reference system was designed. Two capillaries were positioned in close proximity and a single laser was used to illuminate both capillaries. The capillaries were tilted in opposite directions so that the two backscatter fringe patterns were positioned above and below the laser. Using two bicells, it was possible to monitor both fringe patterns simultaneously. Performing a temperature ramp, detection limits were determined to be 6.9×10^{-9} RIU. Detection limits for a glycerol calibration were 6.17×10^{-8} RIU[32].

Fused Silica Chip

A modification of BSI was the replacement of the capillary with a fused silica microfluidic chip. Microfluidic chips are created by isotropically etching a fused silica wafer and fusing another wafer to close the channel. Channels created have a general shape of a hemisphere (or a half circle containing a flat section). A laser directed onto these chips produces a fringe pattern. The shift of the fringe pattern is related to the RI of the sample. Detection limits ranged from 18 to 0.7 mM (glycerol is 0.0104 RIU per M[25] resulting in $1.9 \cdot 10^{-4}$ to $7.3 \cdot 10^{-6}$ RIU) of glycerol depending upon the laser and detector utilized[21].

On-chip BSI was utilized to monitor the change in temperature in water, 100 mM Tris/30 mM boric acid, and 20 mM HEPES (4-(2-Hydroxyethyl)piperazine-1-ethanesulfonic acid)[33]. Temperature changes were induced by application of voltage charges to the chip and the samples. BSI is able to directly detect Joule heating on a fused silica chip. As the voltage was switched on, a change in signal was observed, the opposite signal was observed when the voltage was switched off. The signal change, along with a calibration curve allows for measurement of temperature change resulting from the applied voltage[34].

The next logical step was to utilize BSI to perform on-chip electrophoresis. Using fused silica chip with a T-shaped channel, samples of fluorescein (Figure 1.11), sucrose, raffinose, and caffeine were detected with BSI. RI changes were detectable at the 10^{-6} level[35]. A mixture of calmodulin, α-lactalbumin, pepsinogen, egg albumin, and BSA was injected by pinched injection and separated on chip. The concentration detection limits were in the hundreds of nanomolar for each of the samples[36].

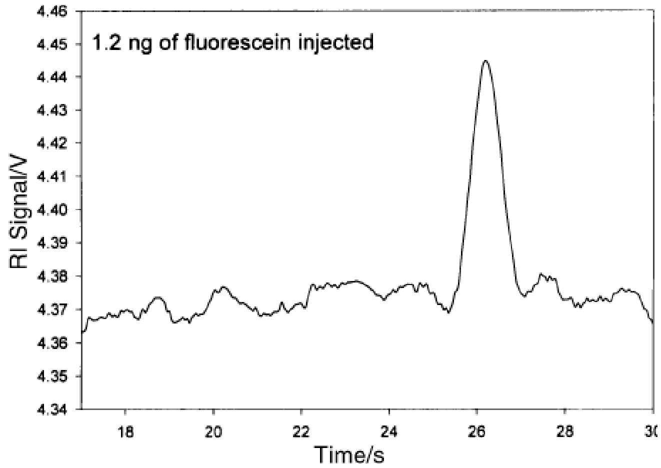

Figure 1.11. BSI chip scale results of electrophoresis of fluorescein in a 40 µm channel[35]

The fused silica chip BSI system was also used to monitor flow. The system was aligned similarly to the capillary flow experiment. Once again an IR laser was used to heat a flowing stream of fluid before the probe beam of BSI. The IR laser was pulsed by means of a shutter and shutter frequency was used to determine the frequency of the signal to be monitored. On-chip flow sensor was used to monitor flow rates of 3 to 6 µL/hour with detection limits of 0.127 nL/s. Sensitivity of the on-chip BSI system was also analyzed. A two degree temperature change was used to calibrate the system and detection limits of 7×10^{-6} RIU. The temperature calibration and glycerol calibration curve produced similar results[26].

PDMS Chip

The next modification to BSI was the use of chips molded in poly(dimethyl)siloxane (PDMS). PDMS chips have the advantage of being inexpensive and allow for the fabrication of different types of channels. The disadvantage of PDMS chips is that, as an elastomer, pressure fluctuations can cause the channel walls to change position, and the chip manufacturing must be reproducible to obtain chips that give consistent results[37].

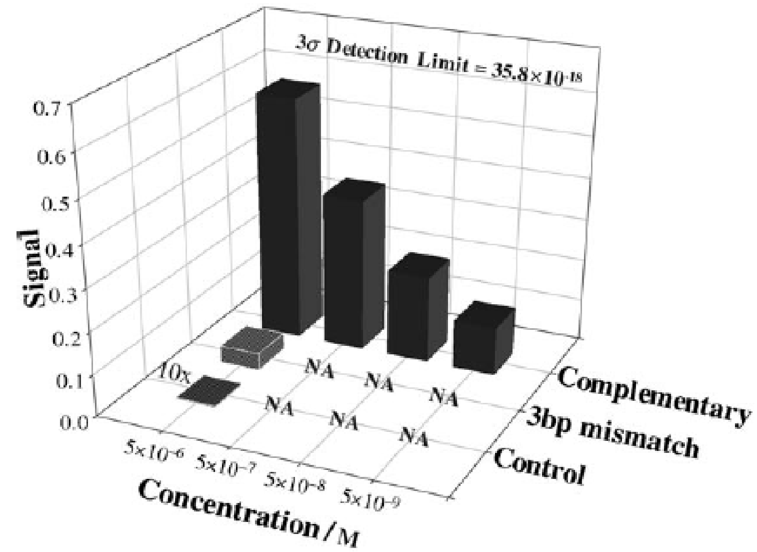

Figure 1.12. BSI DNA experiments[38]

Surface chemistry interactions were monitored utilizing the new PDMS system. The surface of the PDMS chip was modified to bind streptavidin on the surface. BSI was used to observe the interaction of biotin and streptavidin by monitoring the fringe pattern before and after the biotin was introduced. A fluorescently labeled biotin was used to monitor the interaction for comparison; the percent signal change in fluorescence and BSI corresponded well. Biotinylated protein A was placed onto the surface and IgG was introduced. The change in signal was monitored by BSI with femtomole detection limits[37]. New surface chemistry was developed to provide a two fold improvement in the detection limits of the protein A-IgG interaction. BSI was also used to quantify the hybridization of complimentary strands of DNA to a 30-mer of mActin over a range of concentrations. A 3 base pair mismatch was also measured for comparison, a 7 % signal of the complimentary strand was observed (Figure 1.12)[38].

The most recent application of BSI free-solution label-free molecular interaction assays. A PDMS chip with a serpentine mixer and restriction was used to mix two interacting species on chip by drawing the samples into the channel with a vacuum. The probe beam is position directly after the mixer. Once the mixed samples are in the probe volume, the vacuum is removed and the interaction of species can be monitored in real time. Binding affinities for calmodulin (CaM) and calcium ion (Ca^{2+}), CaM and trifluoperazine dihydrochloride (TFP), CaM and calcineurin (CaN), CaM and the M13 peptide, P_A-IgG, and interleukin-2 (IL-2) and its antibody (Figure 1.13) were determined by BSI. The K_d values determined by BSI, ranged from 4 µM to tens of picomolar and correspond with values reported in the literature. Further, BSI showed detection limits of zeptomoles of IL-2 within the probe volume of 350 pL, demonstrating that 12,600 molecules of IL-2 and 0.6 attomoles of antibody could be detected with BSI. This data demonstrates that molecular interaction assays can be performed in free-

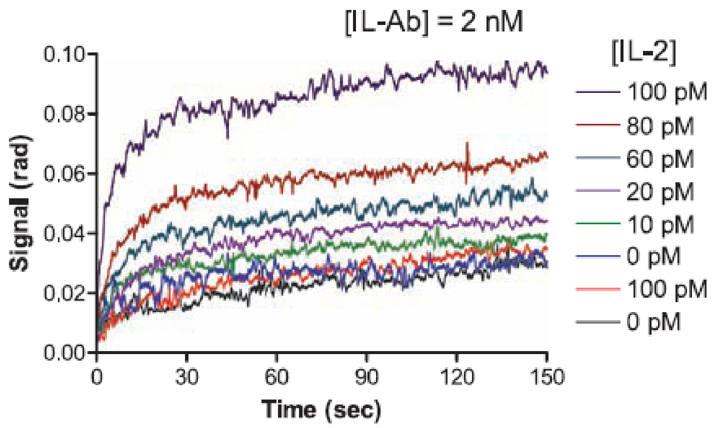

Figure 1.13. IL-2-Ab binding in cell free media[39]

solution label-free in a short amount of time and utilizing only a small amount of sample[39].

1.3 Summary

The interaction of coherent light produces interference patterns. Interferometry utilizes this property of light in the analysis of samples. Interference patterns can be utilized to monitor temperature[14], vibration[14], noise[14], electric fields[14], flow rates[26], and RI changes in samples[21]. Label free molecular interaction have been monitored by interferometry in picoliter volumes[39], providing a valuable tool for protein interaction assays. Advancements in interferometry have allowed for measurements not previously possible and with volumes that are be prohibited by other techniques due to limited sample size.

1.4 References

1. Elmore, W.C. & Heald, M.A. *Physics of Waves*, (Dover, New York, 1985).

2. Moore, T.A. *Six Ideas that Shaped Physics*, (WCB/McGraw-Hill, Boston, 1998).

3. Born, M. & Wolf, E. *Principles of Optics*, (Cambridge University Press, Cambridge, 1999).

4. Harvey, D. *Modern Analytical Chemistry*, (McGraw-Hill, Boston, 2000).

5. Brandenburg, A. & Henninger, R. Integrated Optical Young Interferometer. *Applied Optics* **33**, 5941-5947 (1994).

6. Ymeti, A. et al. Realization of a multichannel integrated Young interferometer chemical sensor. *Applied Optics* **42**, 5649-5660 (2003).

7. FarfieldSensorLtd. The Fundamental Principles of the AnaLight System. (http://www.farfield-scientific.com/index.asp).

8. FarfieldSensorLtd. Refractive Index Sensitivity of the AnaLight System. (http://www.farfield-scientific.com/index.asp).

9. FarfieldSensorLtd. Repeatability of Measurement Using the AnaLight System. (http://www.farfield-scientific.com/index.asp).

10. FarfieldSensorLtd. Real-Time Detection of Small Molecule Interactions and Associated Conformational Changes in Proteins. (http://www.farfield-scientific.com/index.asp).

11. FarfieldSensorLtd. Preparing a Farfield Sensor for Bioanalysis. (http://www.farfield-scientific.com/index.asp).

12. Heideman, R.G. & Lambeck, P.V. Remote opto-chemical sensing with etreme sensitivity: design, fabrication and performance of a pigtailed integrated optical phase-modulated Mach-Zehnder interferometer system. *Sensors and Actuators B* **61**, 100-127 (1999).

13. Weisser, M. et al. Specific bio-recognition reactions observed with an integrated Mach-Zehnder interferometer. *Biosensors & Bioelectronics* **14**, 405-411 (1999).

14. Yoshino, T., Kurosawa, K., Itoh, K. & Ose, T. Fiberoptic Fabry-Perot-Interferometer and Its Sensor Applications. *Ieee Journal of Quantum Electronics* **18**, 1624-1633 (1982).

15. Varma, M.M., Nolte, D.D., Inerowicz, H.D. & Regnier, F.E. Spinning-disk self-referencing interferometry of antigen-antibody recognition. *Optics Letters* **29**, 950-952 (2004).

16. Varma, M.M., Inerowicz, H.D., Regnier, F.E. & Nolte, D.D. High-speed label-free detection by spinning-disk micro-interferometry. *Biosensors & Bioelectronics* **19**, 1371-1376 (2004).

17. Bradshaw, J.T., Mendes, S.B. & Saavedra, S.S. Planar integrated optical waveguide spectroscopy. *Analytical Chemistry* **77**, 28a-36a (2005).

18. Skivesen, N. et al. Photonic-crystal waveguide biosensor. *Optics Express* **15**, 3169-3176 (2007).

19. Bornhop, D.J. Microvolume Index of Refraction Determinations by Interferometric Backscatter. *Applied Optics* **34**, 3234-3239 (1995).

20. Swinney, K., Markov, D., Hankins, J. & Bornhop, D.J. Micro-interferometric backscatter detection using a diode laser. *Analytica Chimica Acta* **400**, 265-280 (1999).

21. Swinney, K., Markov, D. & Bornhop, D.J. Chip-scale universal detection based on backscatter interferometry. *Analytical Chemistry* **72**, 2690-2695 (2000).

22. Swinney, K., Markov, D. & Bornhop, D.J. Ultrasmall volume refractive index detection using microinterferometry. *Review of Scientific Instruments* **71**, 2684-2692 (2000).

23. Sorensen, H.S., Pranov, H., Larsen, N.B., Bornhop, D.J. & Andersen, P.E. Absolute refractive index determination by microinterferometric backscatter detection. *Analytical Chemistry* **75**, 1946-1953 (2003).

24. Tarigan, H.J., Neill, P., Kenmore, C.K. & Bornhop, D.J. Capillary-scale refractive index detection by interferometric backscatter. *Analytical Chemistry* **68**, 1762-1770 (1996).

25. *Handbook of Chemistry and Physics*, (CRC Press, Inc., Boca Raton, 1996-97).

26. Markov, D.A., Dotson, S., Wood, S. & Bornhop, D.J. Noninvasive fluid flow measurements in microfluidic channels with backscatter interferometry. *Electrophoresis* **25**, 3805-3809 (2004).

27. Markov, D., Begari, D. & Bornhop, D.J. Breaking the 10-7 Barrier for RI Measurements in Nanoliter Volumes. *Analytical Chemistry* **74**, 5438-5441 (2002).

28. Swinney, K., Pennington, J. & Bornhop, D.J. Ion analysis using capillary electrophoresis with refractive index detection. *Microchemical Journal* **62**, 154-163 (1999).

29. Swinney, K., Pennington, J. & Bornhop, D.J. Universal detection in capillary electrophoresis with a micro-interferometric backscatter detector. *Analyst* **124**, 221-225 (1999).

30. Kenmore, C.K., Erskine, S.R. & Bornhop, D.J. Refractive-index detection by interferometric backscatter in packed-capillary high-performance liquid chromatography. *Journal of Chromatography A* **762**, 219-225 (1997).

31. Markov, D.A. & Bornhop, D.J. Nanoliter-scale non-invasive flow-rate quantification using micro-interferometric back-scatter and phase detection. *Fresenius Journal of Analytical Chemistry* **371**, 234-237 (2001).

32. Wang, Z.L. & Bornhop, D.J. Dual-capillary backscatter interferometry for high-sensitivity nanoliter-volume refractive index detection with density gradient compensation. *Analytical Chemistry* **77**, 7872-7877 (2005).

33. Swinney, K. & Bornhop, D.J. Noninvasive picoliter volume thermometry based on backscatter interferometry. *Electrophoresis* **22**, 2032-2036 (2001).

34. Swinney, K. & Bornhop, D.J. Quantification and evaluation of Joule heating in on-chip capillary electrophoresis. *Electrophoresis* **23**, 613-620 (2002).

35. Swinney, K. & Bornhop, D.J. A chip-scale universal detector for electrophoresis based on backscattering interferometry. *Analyst* **125**, 1713-1717 (2000).

36. Wang, Z.L., Swinney, K. & Bornhop, D.J. Attomole sensitivity for unlabeled proteins and polypeptides with on-chip capillary electrophoresis and universal detection by interferometric backscatter. *Electrophoresis* **24**, 865-873 (2003).

37. Markov, D.A., Swinney, K. & Bornhop, D.J. Label-free molecular interaction determinations with nanoscale interferometry. *Journal of the American Chemical Society* **126**, 16659-16664 (2004).

38. Latham, J.C., Markov, D.A., Sorensen, H.S. & Bornhop, D.J. Photobiotin surface chemistry improves label-free interferometric sensing of biochemical interactions. *Angewandte Chemie-International Edition* **45**, 955-958 (2006).

39. Bornhop, D.J. et al. Free-solution, label-free molecular interactions studied by back-scattering interferometry. *Science* **317**, 1732-1736 (2007).

CHAPTER II

LabVIEW™ DATA ACQUISITION AND ANALYSIS PROGRAMS FOR BACKSCATTERING INTERFEROMETRY

2.1 Introduction

For the backscattering interferometer to function as a sensitive instrument it is critical to effectively interrogate the fringe pattern. The fringe pattern must be displayed to aid in alignment, and the results quantified to transduce the signal. Over the years, Dr. Bornhop's group has implemented several different acquisition and analysis procedures, including the use of a slit-photo detector assembly[1], a bicell[2], and a commercial laser beam analyzer[3]. In each case the output was collected in a time-consuming manner and the user interface was cumbersome or required a great deal of expertise.

We recently published[4-6] an approach that employs a linear CCD array and a fast Fourier transform (FFT) to acquire a fringe pattern and determine the positional shift with a change in RI. This method of measuring the change in position of the fringes works because a shift in the fringe pattern does not change the frequency of the pattern. Yet this approach is limited because a) it requires aligning the system so that the camera interrogates a sinusoidal region of the fringe pattern and b) these fringes don't shift spatially as much as those closer to the center of the pattern which are not a single frequency. Functionally the FFT approach works by having a slice of pixels from the middle of the fringe pattern sampled, and then a Fourier transform is performed to generate a frequency vs. amplitude output. With the appropriate alignment of the fringes, a single frequency can be sampled. Phase of the frequency is related to the shift in the pattern. Using the Fourier transform method, detection limits of 7 x 10^{-8} RIU were obtained with BSI using a fused silica capillary[4].

Until now, there was no graphical user interface (GUI) for the instrument and data analysis was performed off-line using an Excel program. A program to perform the necessary calculation in real time was designed, implemented, and evaluated. The code necessary to allow a simple graphical interface so the BSI can be used easily was developed using LabVIEW™ (LV) 8.2 from National Instruments™ (NI).

The programs created in LV have a graphical user interface (GUI) to allow the user to control different aspects of the program. The GUI is a graphical representation of commands such as buttons that start or stop functions in the program, and also allows the user to monitor the output of the program in real time.

2.2 Fourier Transform Program

The Fourier transform program written in LV performs the same function as the program that was previously written, e.g. the FFT and allows the utilization of the Garry 3000 linear CCD array (Ames Photonics, Inc.). A flow diagram of the FFT program is shown in Figure 2.1 (LV code is shown provided in the appendix). The FFT code was divided into different sections; which include initialization, setup mode, acquisition mode, timer, and saving data. At the

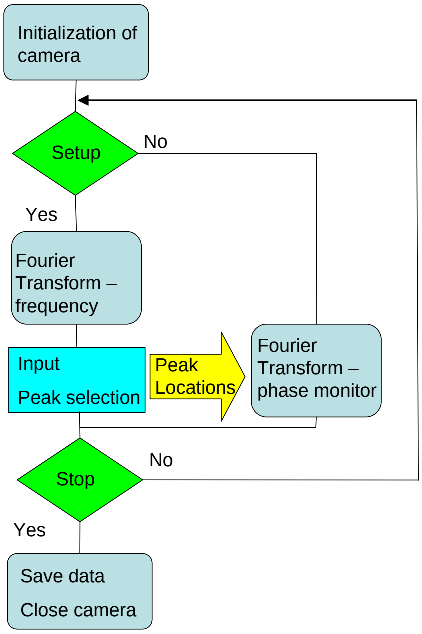

Figure 2.1. Flow diagram of FT program

start of the program, the camera is initialized so that the computer can communicate with the Garry 3000 or Garry 3000SD (Ames Photonics, Inc.) linear CCD. In the setup mode, a Fourier transform is performed on the raw data from the camera and the frequencies to be monitored are input by the user. In the data-acquisition mode, the phases of the selected frequencies are measured over time. When the program is stopped, the data are saved and communication with the camera ceases. When writing the program, a major consideration was to insure that the final speed at which the data can be acquired was high enough to prohibit truncation of the signal. A speed of 68 frames per second (fps) was accomplished with this program, which was adequate for our measurements.

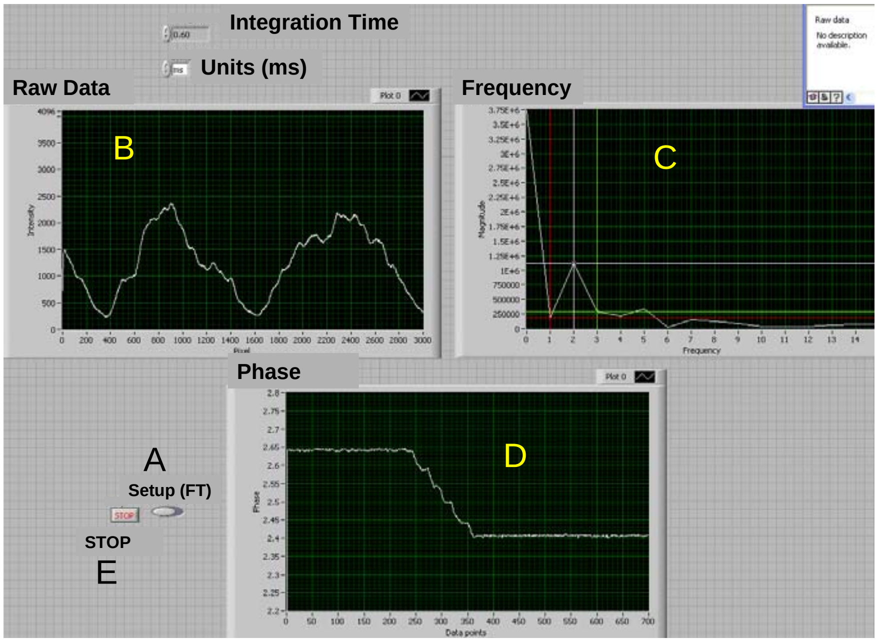

Figure 2.2. Front panel of LV Fourier transform data acquisition program for BSI. A) setup switch B) raw data C) Fourier frequency spectrum D) phase over time E) stop button

Figure 2.2 presents a screen dump of the front panel of the program. There is a setup switch, a real-time fringe pattern display, a panel showing the FFT amplitude vs. frequency for the fringe pattern, and a real-time tracing of the phase (position or shift) vs. time.

2.2.1 Program Operation

Toggling *setup* switch (Figure 2.2A) to “True” and running the program activates the setup mode, which takes the raw data (Figure 2.2B) from the CCD and performs a FFT with resulting frequency data displayed in Figure 2.2C. As shown in Figure 2.2B, there are two fringes on the detector. The corresponding frequency in Figure 2.2C is two cycles per 3000 pixels. The user selects the frequencies to be monitored by use of three cursors. With the *setup* switch to “False”, the phases of the selected frequencies are measured. The first cursor phase is displayed in Figure 2.2D in real time. The *stop* button (Figure 2.2E) ceases the program and the user is prompted to save the data. The data file contains: the phase values from the selected frequencies, a time stamp for each point, and the initial and final fringe pattern.

2.2.2 Program Evaluation

The program was tested by comparing system calibration performance to the previous Fourier transform program utilized in the Bornhop laboratory. Glycerol samples were introduced into the on-chip BSI system to produce a known RI change in triplicate measurements and the signal was observed using both the old Fourier program and the new LV program. The detection limit for the old program was 3.7 x 10^{-5} RIU and 1.3 x 10^{-5} RIU for the LV program, demonstrating the functionality of the new LV program. One reason for the improvement of the detection limits is the LV program utilizes the number of points provided without zero padding or truncating where as the old Fourier transform program required 2^n samples. This data analysis requirement limits the program to zero padding the fringe pattern which can result in noise in the measurements[4].

2.3 Temperate Control Program

A program was written to control and monitor temperature over time. BSI experiments utilize temperature controllers to maintain a constant temperature because small variations in temperature result in a shift of the fringe pattern due to a relatively high dn/dT for most fluids. These temperature fluctuations produce false signals such as drift and short-term noise. The Wavelength Electronics (model LFI-3751) temperature controllers utilized in the laboratory have LV drivers so it is possible to integrate control within the graphical user interface program. The temperature controllers read the resistance of a thermistor, located in the middle of the chip holder. A thermal electric cooler (TEC) is used to heat (or cool) the chip holder. Once calibrated, the temperature controller produces values in degrees Celsius instead of resistance which is the output from the thermistor. Most experiments using BSI are performed at 25°C so that the temperature controller is kept slightly above room temperature (active control). Real-time monitoring and control of the temperature is necessary to determine if temperature variation is a cause of signal fluctuations.

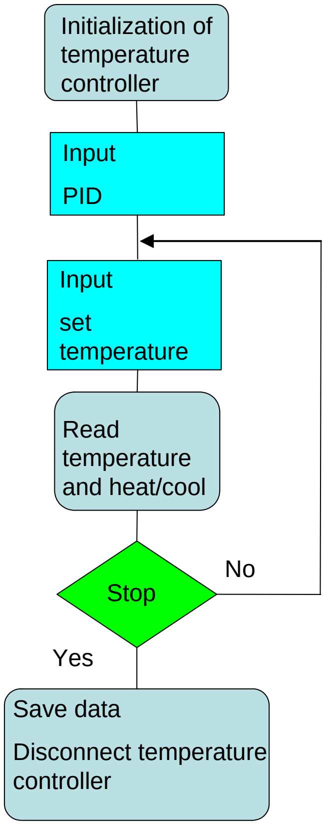

Figure 2.3. Flow diagram of temperature control program

Two versions of a temperature control and monitoring program were written. One program in which the set temperature/PID (proportional band, integral, and derivative) settings are read only at the beginning of the program and one program in which the temperature/PID can be set at any time (this decreases the speed of the data acquisition). If the proportional band (P) is too high, the actual temperature will not reach the set point, and if it is too low, the actual temperature will overshoot or undershoot the set point. The integral (I) setting adjusts P with respect to the set point to compensate for drift. The derivative (D) adjusts the P to minimize overshoot or undershoot[7] with respect to the set point.

Figure 2.3 shows the flow diagram of the temperature controller program with input PID only at the start of the program. The initialization allows the computer to talk to the temperature controller (Wavelength Electronics). The user inputs the PID settings and the set temperature. The reading of actual temperature is compared to the set temperature value and the temperature is adjusted by heat or cold through the TEC to reach the set temperature. Without depressing the stop button, the program returns to reading the set temperature. Once the stop button

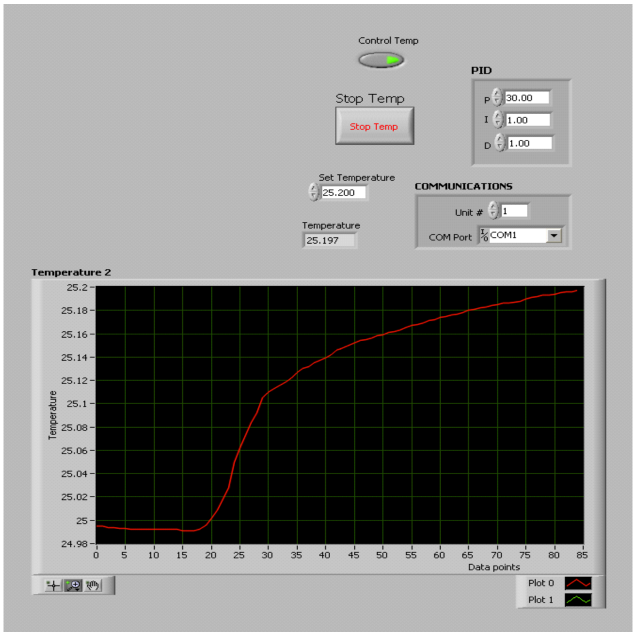

P 30.00
I 1.00
D 1.00
Set Temperature 25.200
Temperature 25.197
Unit # 1
COM Port COM1

Figure 2.4. Front panel of temperature control program

is activated, the data is saved and the communication to temperature controller is disconnected.

Figure 2.4 shows a screen shot of the GUI for the temperature controller program. The communications section provides information for the initialization of the temperature controller. User inputs for the PID and set temperature are utilized to control the temperature. A temperature indicator displays a numerical temperature reading and the graph displays the temperature in real time. When the *stop* button is pushed, the program will prompt the user for a file name in which to save the temperature and time data.

Initially, this program was combined with the Fourier transform so that a temperature measurement was obtained for each data point. However, the temperature controller program runs at about 1 Hz (one point a second), greatly decreasing the speed of the Fourier transform program. If the temperature-control program is completely separate, the decrease in speed is minimal, so the temperature control and data acquisition were decoupled (example shown in Figure 2.8).

2.4 An Alternative Fringe Shift Transductions Method - the Cross Correlation Technique

Fourier transform technique has been beneficial in measuring the changes in the position of the fringe pattern. However, the Fourier technique has limitations, including the necessity that the fringe pattern appear sinusoidal, which requires significant alignment time. An alternative pattern analysis technique was investigated to analyze the positional shift of the fringe pattern. One promising technique for high resolution position sensing is based on a cross correlation (CC)[8]. In a CC the position of a fringe is measured by comparing how two signals have changed, or how well they correlate.

Previous correlation technique measured shifts in the correlation by determining the centroid location in the correlation graph. The correlation technique we developed calculates shifts with high pixel resolution by calculating the center of gravity of the correlation[9]. The advantage of the new CC technique is that it can have very high resolution with respect to positional shift (sub-micropixel) and the analysis method is not dependent on the fringe pattern being sinusoidal so instrument alignment is greatly simplified.

2.4.1 How to Measure a Fringe Shift with the New CC Function

Correlation of two functions F(x) and G(x) is defined as:

$$C_{FG}(x) = \int_{-\infty}^{+\infty} F(x_1)\, G(x_1 + x)\, dx_1 \tag{1}$$

Weighting function is an odd function, such as W(x) = x

$$W(x) = -W(-x) \tag{2}$$

If G(x) is a shifted version of F(x),

$$G(x) \propto F(x + \sigma) \tag{3}$$

then the shift, σ, is given by

$$\sigma = N \frac{\int_{-\infty}^{+\infty} W(x)\, C_{FG}(x)\, dx}{\int_{-\infty}^{+\infty} C_{FG}(x)\, dx} \tag{4}$$

where N is a normalization constant determined by shifting the reference function F(x) a known amount, one pixel for example[9].

Initially a reference pattern is chosen and for simplicity the same pattern will be used as the sample. The cross correlation of the two patterns is performed (Figure 2.5).

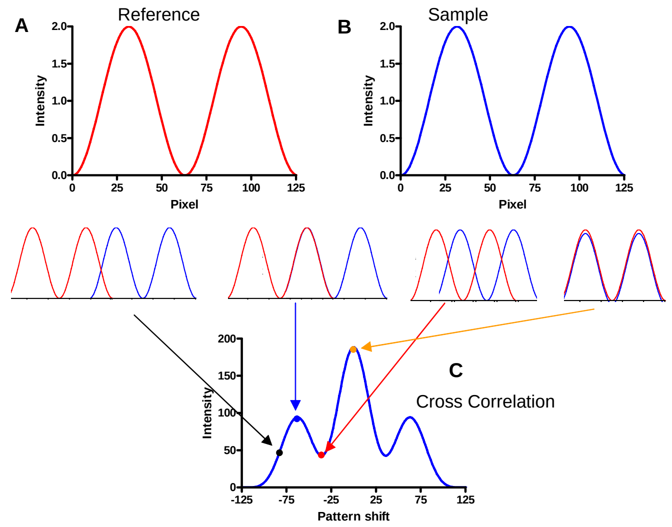

Figure 2.5. Reference (A) and sample (B) patterns with resulting cross correlation (C) with selected points demonstrated

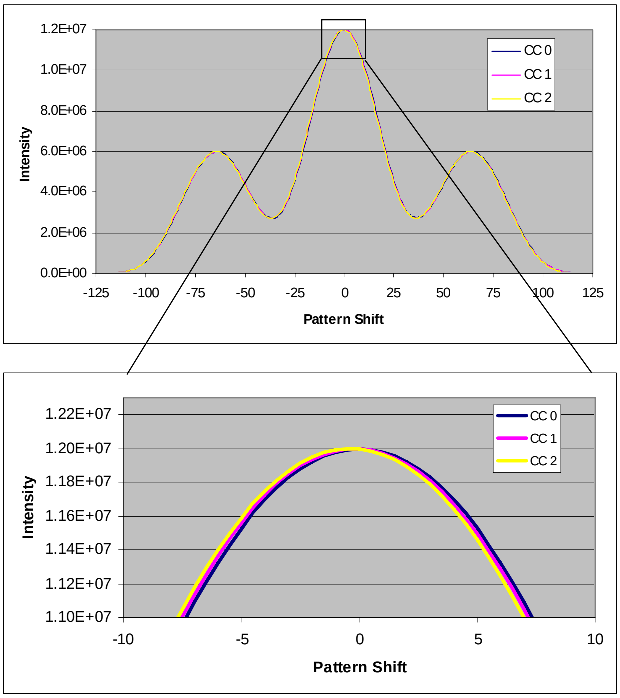

Figure 2.6. Cross correlations of three different samples, with close view of the peak

As the sample pattern shifts with respect to the reference, the cross correlation pattern also changes. For small changes, the cross correlation appears similar (Figure 2.6) but a close inspection of the peak demonstrates that there is a shift in the pattern. In order to measure this shift in the correlation, the center of gravity is calculated as shown in Figure 2.7. The correlation pattern (Figure 2.7A) of the sample and reference patterns is multiplied by a weighting function (Figure 2.7B), which is a line with a slope = 1 that has the same correlation (x) values. The pixel shift between the sample and reference is calculated by the sum of the weighted values (Figure 2.7C) divided by the sum of the correlation values in the correlation of the sample and reference patterns, resulting in the normalization of the data

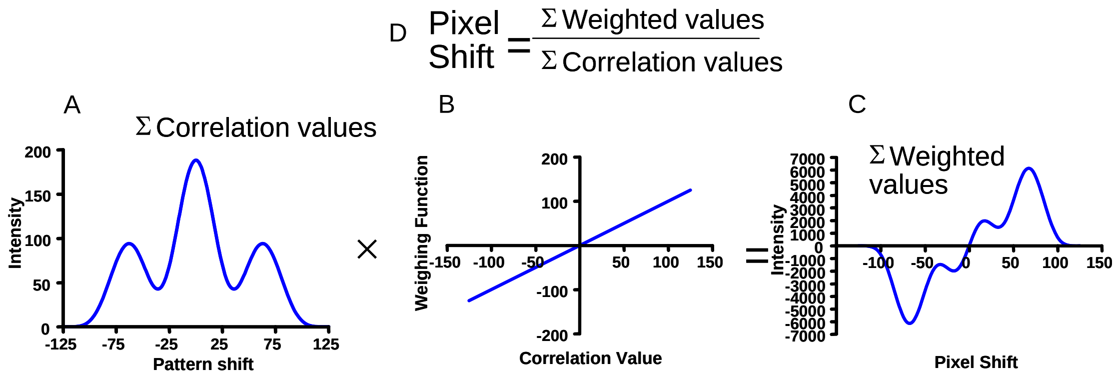

Figure 2.7. Calculation of the pixel shift from correlation pattern. A) cross correlation pattern B) Weighting function C) A x B D) equation for pixel shift (sum C / sum A)

so that intensity fluctuations do not affect the pixel shift values. The theory of the cross correlation technique works with even small changes in the sample pattern calculating pixel shifts with high resolution.

2.5 Correlation Program

At the same time that a CC for fringe shift analysis was implemented, a version of BSI was constructed (to further increase S/N) which employed both a sample and reference channel[2]. In order to do so, the optics were modified (as described in Chapter 3) and a two-dimensional CCD array (2D CCD) was utilized to monitor two separate fringe patterns simultaneously.

A flow diagram of the new CC program is shown in Figure 2.8. The program was written to facilitate the use of the CC for BSI. The temperature control portion of the program works as described previously. Initialization of the camera allows the computer to communicate with the 2D CCD (Basler). In the setup mode, the user defines the number of frames to average and two region of interest (ROI) are selected to be monitored. When the setup mode is turned off, the two ROIs are selected from the

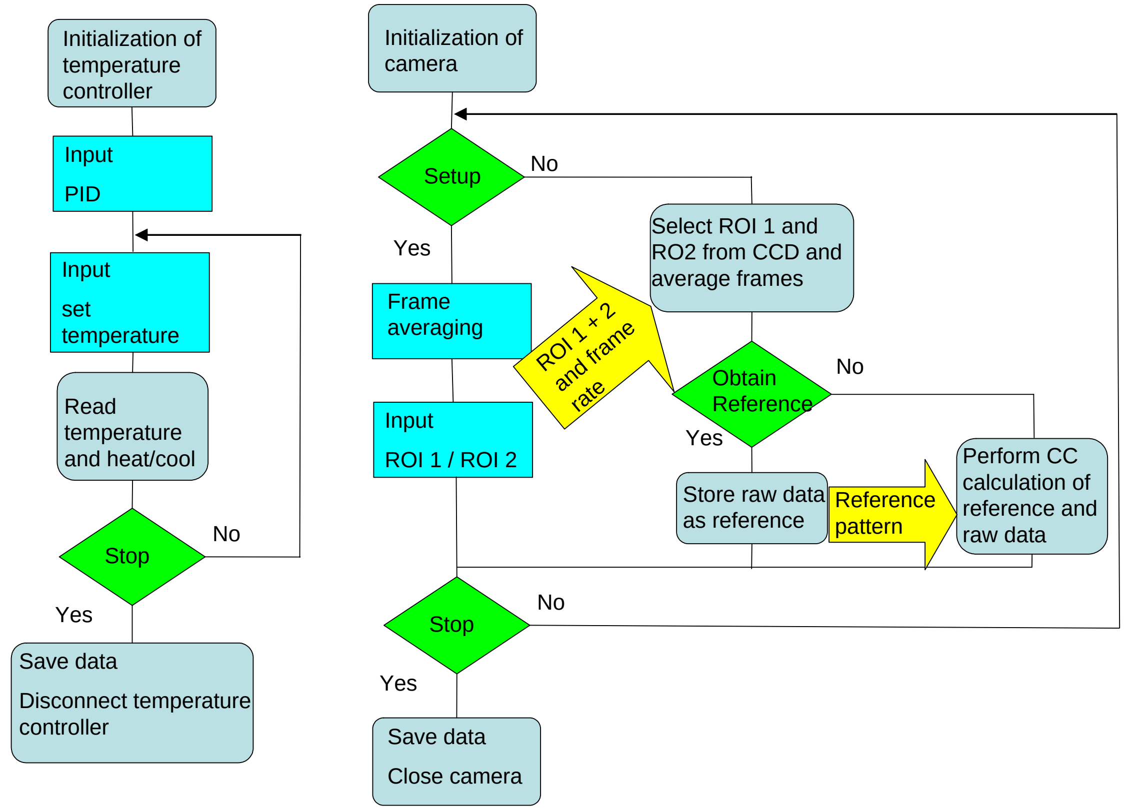

Figure 2.8. Flow diagram of the CC program with temperature controller

camera frame and the specified number of frames is averaged. With the obtain reference switch on, the program saves the raw data as the reference pattern. With the "obtain reference" switch set to "No" results in the CC calculation between the reference pattern and the raw data from the camera being performed. When the stop button is depressed, the data are saved and the communication with the camera is ceased. LV code is shown in the appendix.

The screen shot of the setup tab from the program (Figure 2.9) displays the image from the two dimensional CCD and allows the user to draw a green rectangle on the image to select sections for analysis. Two regions can be analyzed simultaneously, for the two-channel system. On the front panel are six options to aid the user in analysis and collection of data. 1) The dark pixel value is used to remove the value of the pixels when

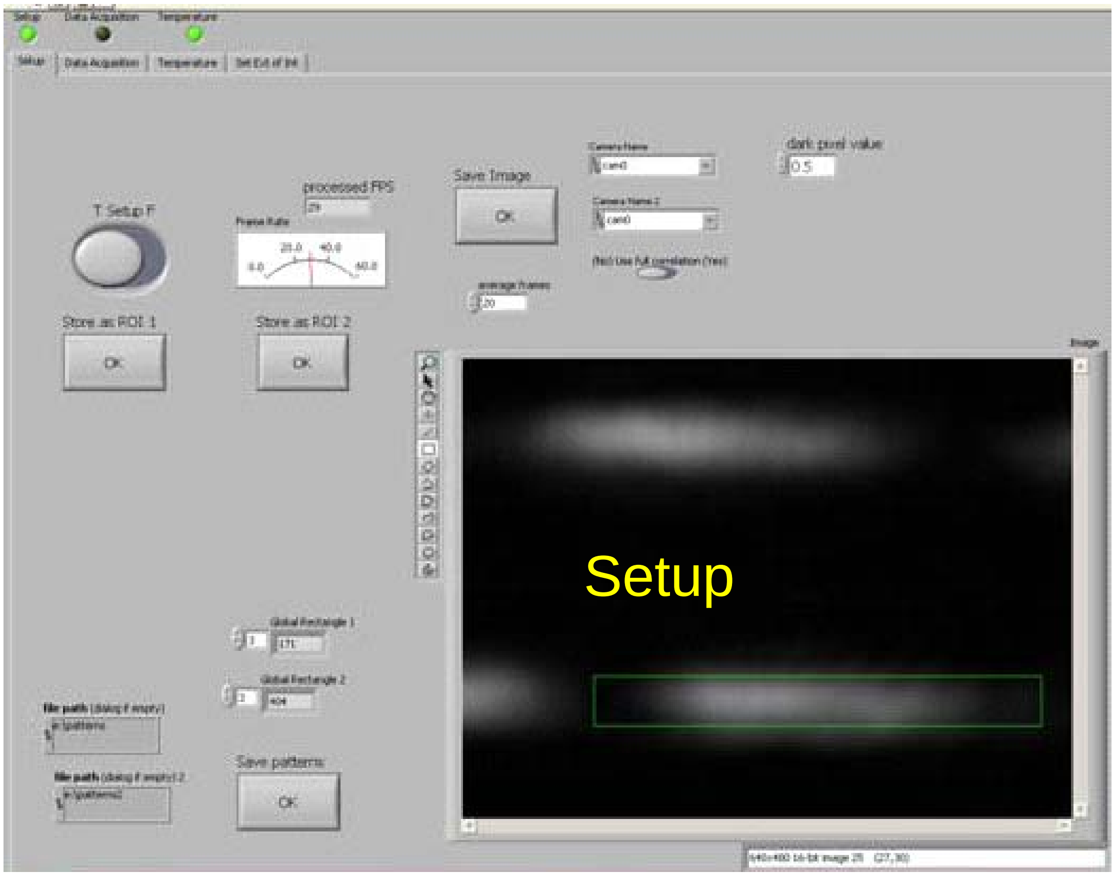

Figure 2.9. Setup screen of the correlation program

the camera is covered, which is only about 0.5 intensity for the CCD camera (Basler) used in BSI. 2) The *average frames* option is used to average frames in order to reduce noise. 3) The *save image* button will prompt the user for a location to save the 2D CCD image. 4) The *save patterns* button will save the two fringe patterns generated from the image in the specified locations in the two text boxes. 5) The two global rectangles display the region of interest (ROI) indices for the user. 6) The frame rate display shows the user the rate of the camera.

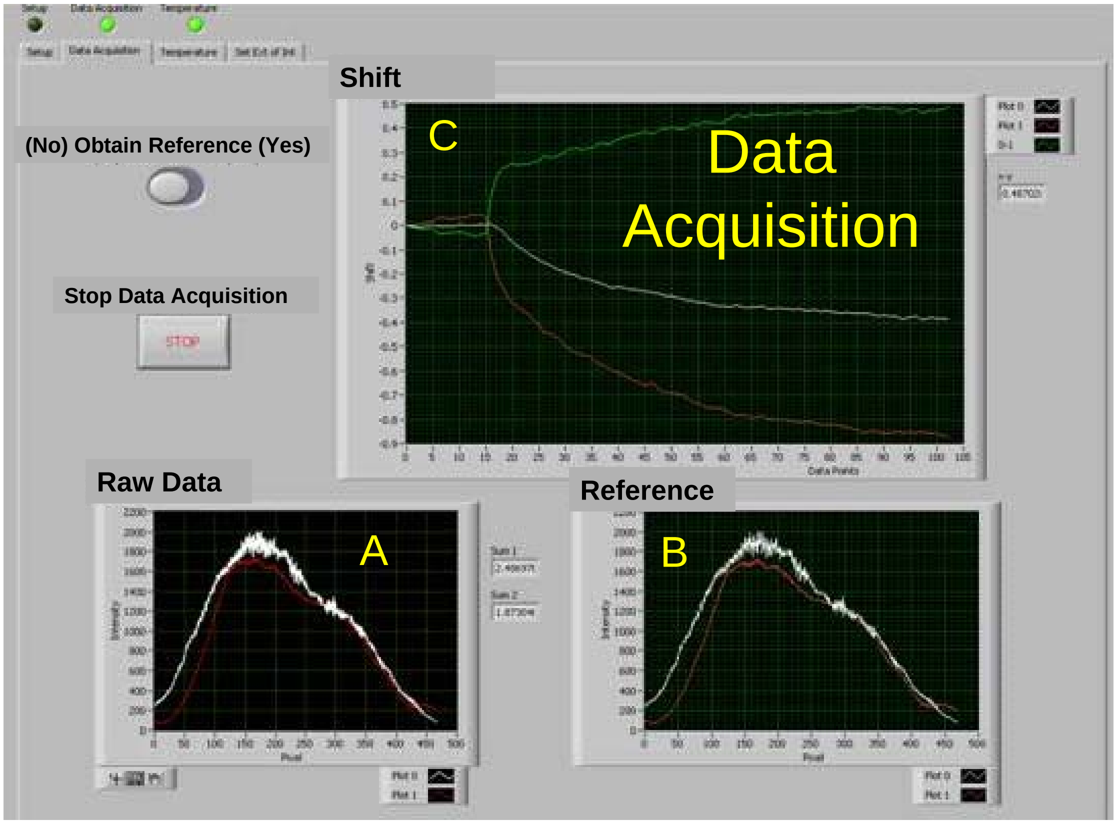

Figure 2.10. Data acquisition screen of the correlation program with A) raw data, B) reference, and C) shift over time graphs

Figure 2.10 shows the data acquisition screen for the CC analysis software. Reference patterns are shown in the lower right graph, raw patterns are shown in the lower left graph. The reference pattern is defined from the raw data graph when the *obtain reference* switch is set to yes. The line profiles of the fringes shown in the graphs are calculated from the ROI by averaging the rows in each rectangle. The correlation technique (Figure 2.7) is used to calculate the pixel shift which is displayed in Figure 2.10C. The ROI 1 corresponds to the white pattern and the ROI 2 corresponds to the red pattern. The white pixel shift corresponds to the white pattern and the red pixel shift corresponds to the red pattern. The green pixel shift is equal to pixel shift 1 – pixel shift 2. The user is prompted to save the temperature data when the *stop* button is depressed.

The temperature tab (Figure 2.11) allows the user to control the temperature controller (Wavelength Electronics). Temperature versus data point is displayed in the graph. PID settings can be input only before the program is started. The set temperature can be changed at any time, thus allowing the user to perform temperature calibration curves. The temperature function runs separate from the data analysis function and has a *stop* button as well.

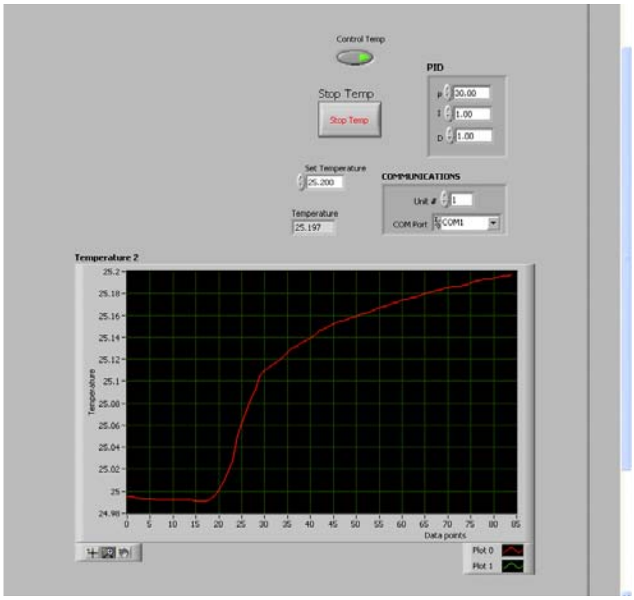

P 30.00
I 1.00
D 1.00
Set Temperature 25.200
Temperature 25.197
Unit # 1
COM Port COM1

Figure 2.11. Temperature control tab

2.5.1 Cross Correlation Evaluation

To test the correlation technique compared to the Fourier transform technique, the BSI system was aligned so that the fringe pattern selected was not perfectly sinusoidal. The RI of the fluid within the channels was changed as in a calibration run and the response of the FFT and CC were compared. Figure 2.12 displays the results of this experiment where a 0.5°C temperature change was introduced to impart RI change for the fluids in the chip and the results for the Fourier transform and CC are calculated. Figure 2.12A and 2.12B show the fringe patterns used. Figure 2.12C shows the Fourier frequency pattern and Figure 2.12D shows the CC correlation pattern. As shown in Figure 2.12E when the sample RI is changed, the FFT performs poorly with respect to the detection of the rather large change in RI signal. When the same experiment was performed (changing the RI by increasing the temperature) the correlation technique responds well giving a substantial signal (Figure 2.12F). Since the Fourier transform results are in radians and the correlation results are in pixel shift, the noise of the two results were scaled to have the same noise level (10 pixel shift = 1 radian) allowing the direct comparison of the two position sensing methods. In summary, these results demonstrate the limitation of the Fourier transform program to calculate shift of a pattern that is not sinusoidal or a single frequency. The correlation program shows about an eight fold improvement of the signal to noise ratio. Several other fringe patterns were analyzed and the correlation performed better or the same as the FT in every case, even when the fringe patterns where aligned to be sinusoidal or single-frequency patterns.

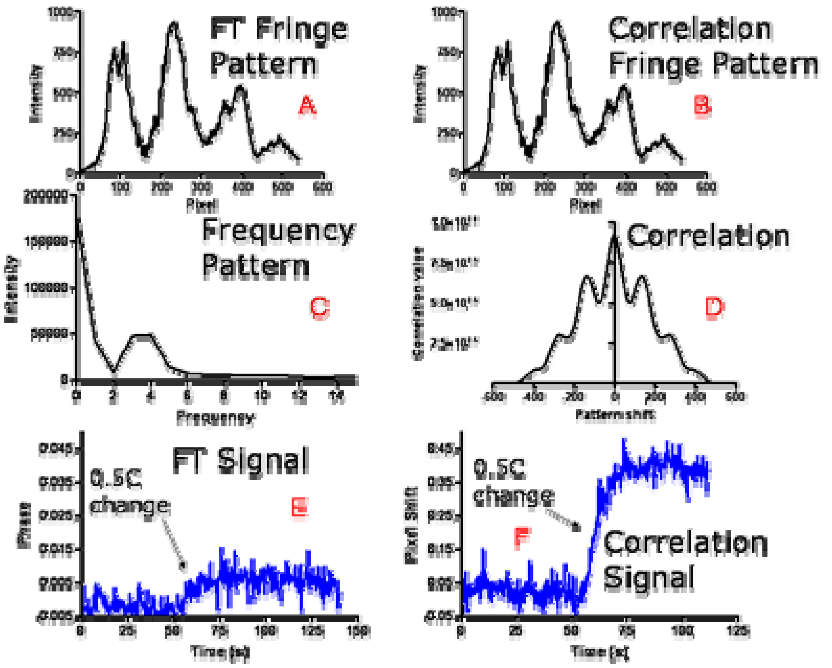

Figure 2.12. (A) Fringe pattern for the Fourier Transform (B) Fringe pattern for correlation (C) Fourier frequency pattern (D) CC correlation pattern (E) FT noise and signal for 0.5°C (F) Correlation noise and signal for 0.5°C

2.6 Data Analysis Program

To have a fully functional BSI instrument, the software program must not only allow collection and display of the data, but also must provide an analytically useful output. Prior to the work presented here, converting the data into a presentable form required the use of multiple programs and was extremely time consuming. Therefore, a program was designed and written in LV to facilitate the analysis of the data generated with BSI.

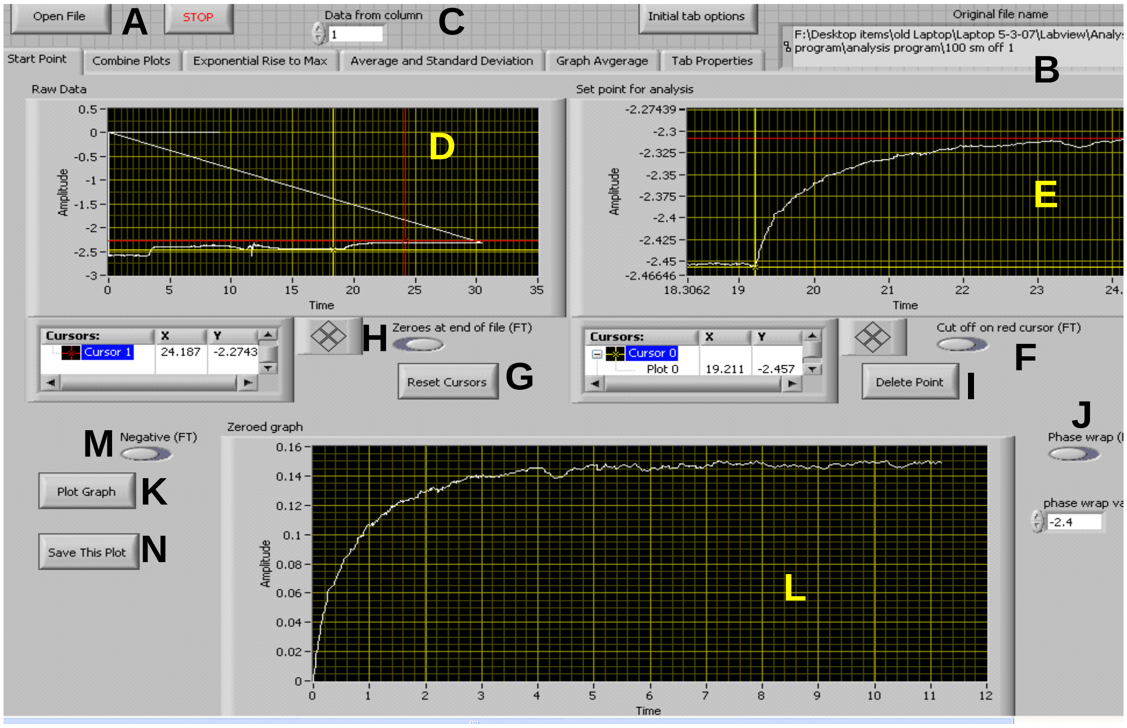

Data from column: 1

Original file name: F:\Desktop items\old Laptop\Laptop 5-3-07\Labview\Analy program\analysis program\100 sm off 1

Cursor 1: X 24.187, Y -2.2743

Cursor 0, Plot 0: X 19.211, Y -2.457

phase wrap va: -2.4

Figure 2.13. Start point tab of data analysis program. A) open file B) file path text box C) data column input D) raw data graph E) zoom in of raw data F) cut off on red cursor switch G) reset cursor button H) zeroes at end of file switch I) delete point button J) phase wrap switch and value K) plot graph button L) zeroed graph based on options M) negative value switch N) save this plot button for zeroed graph

The LV code in the appendix shows the architecture of the entire program, while Figure 2.13 shows the screen shot of the first tab of the graphical user interface (GUI). The LV program is split into sections accessed by the tabs at the top of the program as shown in Figure 2.13. The entire program is started by the LV run button. By depressing the *Open File* button (Figure 2.13A) data from a file specified by the user is read. Any changes to the data by the LV program will not overwrite the original file. For convenience, the file location and name is displayed in a text box located in the top right corner of Figure 2.13 (B). The first column of the data file is used for the time values (the x axis). A number input (Figure 2.13C) is used to select any column of the data file (the y axis). The programs written to monitor BSI, such as the FT and correlation program (described previously), save data so that they can be directly read by the data analysis program.

In the "starting point" tab, the top left graph (Figure 2.13D) displays the raw data from the file. This graph has two cursors (free floating) that are used to define a window where the min and max values of both the x and y values of the cursors are utilized for a second graph (top right, Figure 2.13E). The program determines maximum and minimum values of the two cursors so the order does not matter. Thus the second window (Figure 2.13E) is a zoomed view of the first graph (Figure 2.13D) defined by the cursors. The second graph (Figure 2.13E) also has two cursors. The yellow cursor of the second graph (Figure 2.13E) defines an x value to start the analysis. The red cursor defines the x value for an optional cutoff point so that only a section of the data is sampled. A *cutoff on red cursor* true-false switch (Figure 2.13F) is used to toggle between the option to either remove the rest of the data file or include it. A *reset cursor* button (Figure 2.13G) repositions the cursors to preset locations (minimum and maximum values on Figure 2.13D and ½ and ¾ x values for Figure 2.13E).

LV requires all columns to have the same number of points for data files and can result in the data and time columns having zeroes written to the end of each column. A true-false switch (Figure 2.13H) allows the user to remove the zeroes. When the switch is set to false, the program does not change the data. When the switch is set to true, the program will locate the first zero point (base line of camera is normally above zero) and cut off the data past that point. If the switch is set to true and there are no zeroes at the end of the file, the program does not change the data.

Sometimes there exist spikes or rapid transients in the signal which can be a single point or set of points that obviously do not follow the trend of the data. Sources of such noise include accidentally bumping the experiment, particles passing through the laser beam or random electronic transients. The *delete point* button (Figure 2.13I) allows for the removal (not replace with zeroes) of both the x and y values defined by the first cursor in graph Figure 2.13E.

For the Fourier transform program, phase wrapping can occur when very large RI changes occur in the sample making the fringes shift a large distance. Under these circumstances a large jump from -π to π can occur because the phase value of the Fourier Transform program can only be between -π and π. A *phase wrap* true-false switch (Figure 2.13J) and user set value is used to correct for these jumps. When the switch is set to false, the data is not changed. When the switch is set to true, the program will subtract "2 * π" from any phase value over the user set value.

Using the data defined, the *plot data* button (Figure 2.13K) allows data to be graphed according to the cursors and options defined by the user (Figure 2.13L). The data point defined by the yellow cursor of the graph Figure 2.13E is zeroed (in both x and y values), the rest of the data is adjusted relative to that point and the results are plotted in Figure 2.13L. Since the start point is zeroed, this graph allows the user to easily see binding curves (as shown in Figure 2.13L).

System alignment, such as the orientation of the camera, can result in arbitrarily produce negative values. For example, a fringe shift with a negative response would generate a positive response when the camera is rotated 180 degrees. Species binding analysis requires the binding be expressed as a positive signal. A *negative* true false switch (Figure 2.13M) was implemented so that all values can be multiplied by –1. The *save this plot* button (Figure 2.13N) brings up a text box so that the user can save the data from the graph.

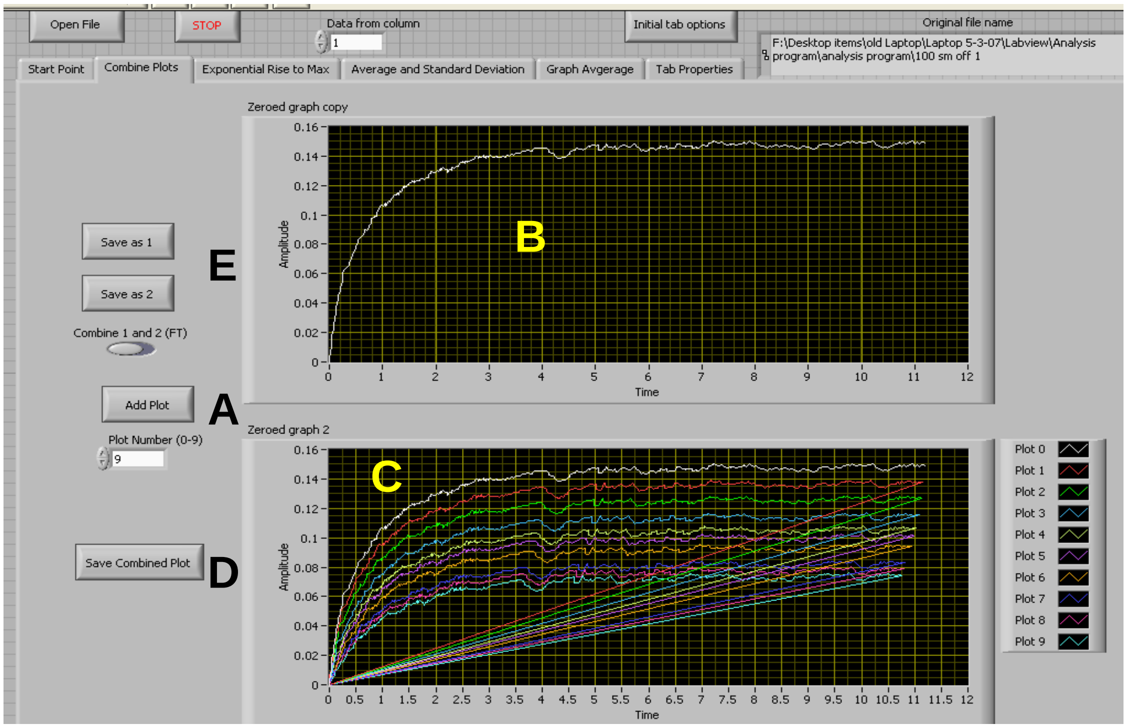

Data from column: 1

Original file name: F:\Desktop items\old Laptop\Laptop 5-3-07\Labview\Analysis program\analysis program\100 sm off 1

Plot Number (0-9): 9

Figure 2.14. Combine plots tab of data analysis program. A) add plot to bottom graph button B) zeroed graph copy C) combined data graph D) saved combined plot button E) save as 1, save as 2, and combine data switch

The start point tab allows the user to zoom in, select, modify (remove phase wrapping, invert, or delete a point), and zero the starting point. These options make the data processing faster and easier than performing similar manipulations off-line with a spreadsheet. Initially, these options were written for real-time binding studies and have since been altered to allow other measurements such as temperature or glycerol calibrations. The start point tab defines the section of data that is used for the rest of the program.

The “combine plots” tab (Figure 2.14) displays a copy of the zeroed graph from the previous tab. The *add plot* button (Figure 2.14A) will take the data from top graph (Figure 2.14B) and copy it in the bottom graph (Figure 2.14C) based on the plot number value input by the user, allowing the user to replace a plot or add a new one. Up to ten graphs can be placed on the bottom graph (Figure 2.14C). The *save combined plot* button (Figure 2.14D) allows values both x and y for all the plots to be saved. The *save as 1* and *save as 2* buttons (Figure 2.14E) save the data from the top graph in a temporary location. The save as buttons in conjunction with the *combine 1 and 2* switch (Figure 2.14E) allow the user to combine two binding curves. The combining data option is designed for binding-dissociation data. Data *saved as 1* is used to store a binding curve. The first point of the data *saved as 2* is set to the value (both x and y) of the last point of the data *saved as 1* and all the values *saved as 2* are changed the same amount. The two data sets are combined and are plotted in the bottom graph (Figure 2.14C). The “combine data” tab allows the user to combine several sets of curves onto one graph. The code was written for the display of binding reaction for multiple runs and saving of the data.

Real time binding experiments have been performed in BSI and the exponential rise to max program was written to facilitate the analysis of these data sets. The fit for a real time binding curve is based on the following equation:

$$Y = Y_{\max} \times \left(1 - e^{(-k \times X)}\right) \qquad (5)$$

Where k is the observed rate constant, Ymax is the maximum Y value, and X is time[10].

The “exponential rise to max” tab (Figure 2.15) is used to calculate the Ymax and k_{obs} values of a real time binding curve. The *exponential rise to max* button (Figure 2.15A) fits a curve to the data from the start point tab and plot both the data and curve in the top plot (Figure 2.15B). LV utilizes a nonlinear fit command to optimize the parameters in equation 4 to fit the data.

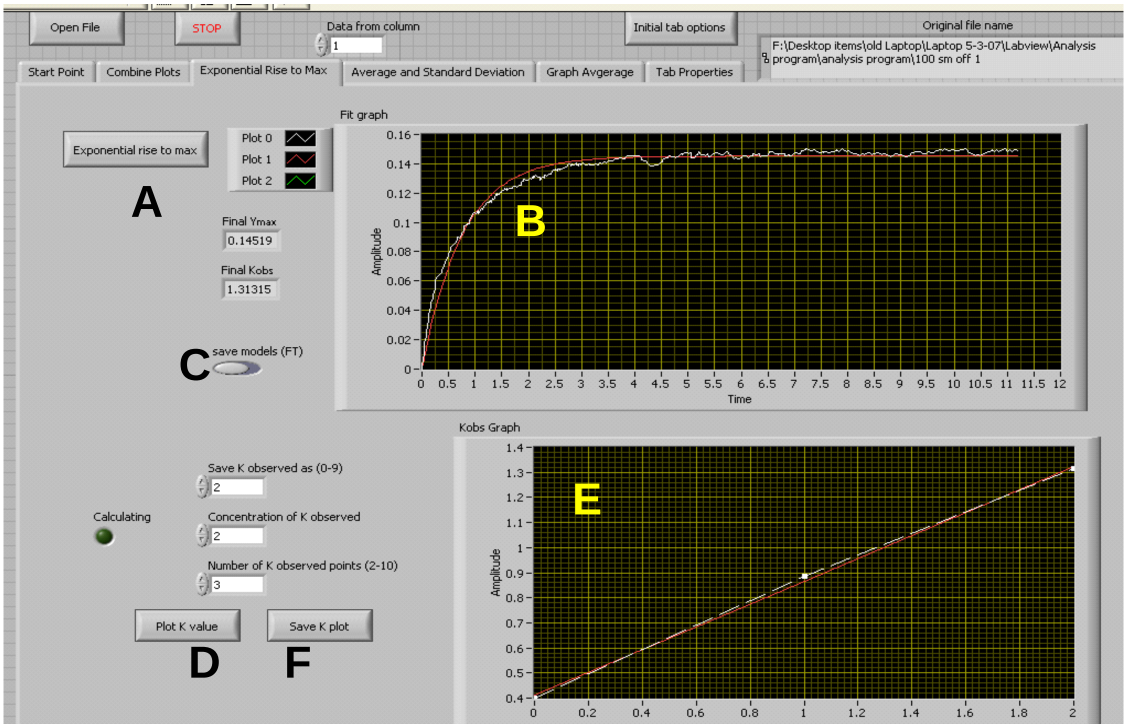

Data from column
1

Original file name
F:\Desktop items\old Laptop\Laptop 5-3-07\Labview\Analysis program\analysis program\100 sm off 1

Final Ymax
0.14519

Final Kobs
1.31315

Save K observed as (0-9)
2

Concentration of K observed
2

Number of K observed points (2-10)
3

Figure 2.15. Exponential rise to max tab of data analysis program. A) exponential rise to max button for fit graph B) plot of data and fit C) save switch D) plot k value button E) k_{obs} plot F) save k plot

The exponential rise to max fit is used to determine the kinetic information for real time binding. The Ymax and k_{obs} values are saved by setting the *save model* switch (Figure 2.15C) to true while depressing the *exponential rise to max* button and naming a file. A small green indicator light shows that the program is computing the Y_{max} and k_{obs}.

The bottom graph (Figure 2.15E) allows the combination of up to ten points of k_{obs} values by using the *plot k value* button (Figure 2.15D). After all the k values are entered, the values and a linear response are plotted on the bottom graph (Figure 2.15E). The plot is saved by the *save k plot* button (Figure 2.15F). The linear plot allows the calculation of K_D (=k2/k1) by dividing the intercept by the slope[5].

The "average and standard deviation" tab (Figure 2.16) allows the analysis of a section of the selected data. When the *run average calculation* switch (Figure 2.16A) is set to false, this calculation is disabled. When the *run average calculation* switch is set to true, there are several parameters that allow the user to calculate an average on a selected section of the plot data (Figure 2.16B). The program displays the number of points

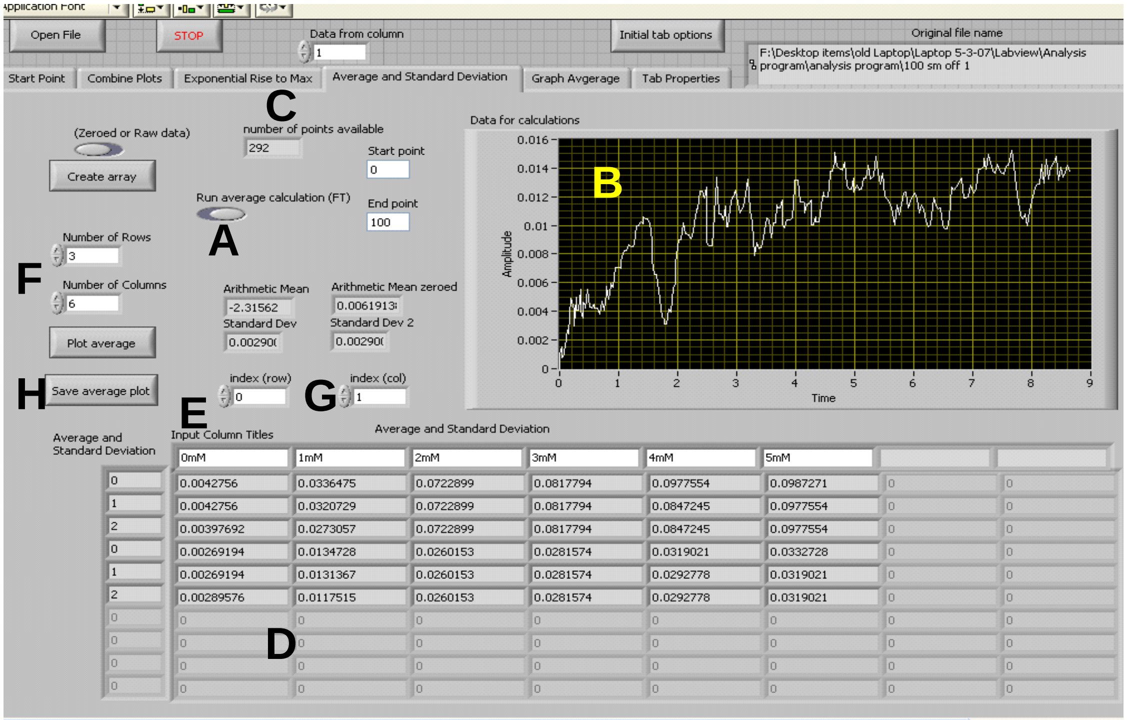

Data from column: 1

Original file name: F:\Desktop items\old Laptop\Laptop 5-3-07\Labview\Analysis program\analysis program\100 sm off 1

number of points available: 292

Start point: 0

End point: 100

Number of Rows: 3

Number of Columns: 6

Arithmetic Mean: -2.31562

Standard Dev: 0.00290

Arithmetic Mean zeroed: 0.0061913

Standard Dev 2: 0.00290

index (row): 0

index (col): 1

Average and Standard Deviation

Input Column Titles

Average and Standard Deviation	0mM	1mM	2mM	3mM	4mM	5mM		
0	0.0042756	0.0336475	0.0722899	0.0817794	0.0977554	0.0987271	0	0
1	0.0042756	0.0320729	0.0722899	0.0817794	0.0847245	0.0977554	0	0
2	0.00397692	0.0273057	0.0722899	0.0817794	0.0847245	0.0977554	0	0
0	0.00269194	0.0134728	0.0260153	0.0281574	0.0319021	0.0332728	0	0
1	0.00269194	0.0131367	0.0260153	0.0281574	0.0292778	0.0319021	0	0
2	0.00289576	0.0117515	0.0260153	0.0281574	0.0292778	0.0319021	0	0
0	0	0	0	0	0	0	0	0
0	0	0	0	0	0	0	0	0
0	0	0	0	0	0	0	0	0
0	0	0	0	0	0	0	0	0

Figure 2.16. Average and standard deviation tab of data analysis program. A) run average calculation switch B) selected data graph C) number of points available display D) average and standard deviation table E) column titles input F) column and row inputs to build table G) position inputs to insert average into table H) save average plot button

available (Figure 2.16C) and the user inputs the start and end points within this point range. The average and standard deviations for both the raw and zeroed data are then displayed for this range. Individual average and standard deviations are saved in the first tab using the *save this plot* button (Figure 2.13N).

The user has the ability to create a table (Figure 2.16D) of averages and standard deviations. Columns titles can be entered by the user (Figure 2.16E). The user defines the size of the table (Figure 2.16F) and selects where each average is placed (Figure 2.16G). The standard deviation data is placed below the average data. The entire table is saved by pressing the *save average plot* button (Figure 2.16H). The average and standard deviation tab allows for the analysis of any data (as compared to binding data alone).

The "graph averages" tab (Figure 2.17) is to graph the table from the "average and standard deviation" section of the program. The user can plot the individual points, the average of the runs, the average with a linear fit, and the average with a hyperbola fit (Figure 2.17A). The hyperbola fit is utilized for endpoint binding assays to determine the kinetic information using the equation:

$$Y = \frac{(B_{Max} \times X)}{(K_D + X)} \tag{6}$$

Where B_{max} is the maximal density of receptor sites and K_D is the equilibrium dissociation constant[10].

These display options allow the user to view the individual plots or the average of the data points for the plots. The linear fit to the averages is for samples such as glycerol or protein calibrations. The hyperbolic fit is designed for the analysis of endpoint assays of binding pairs[5].

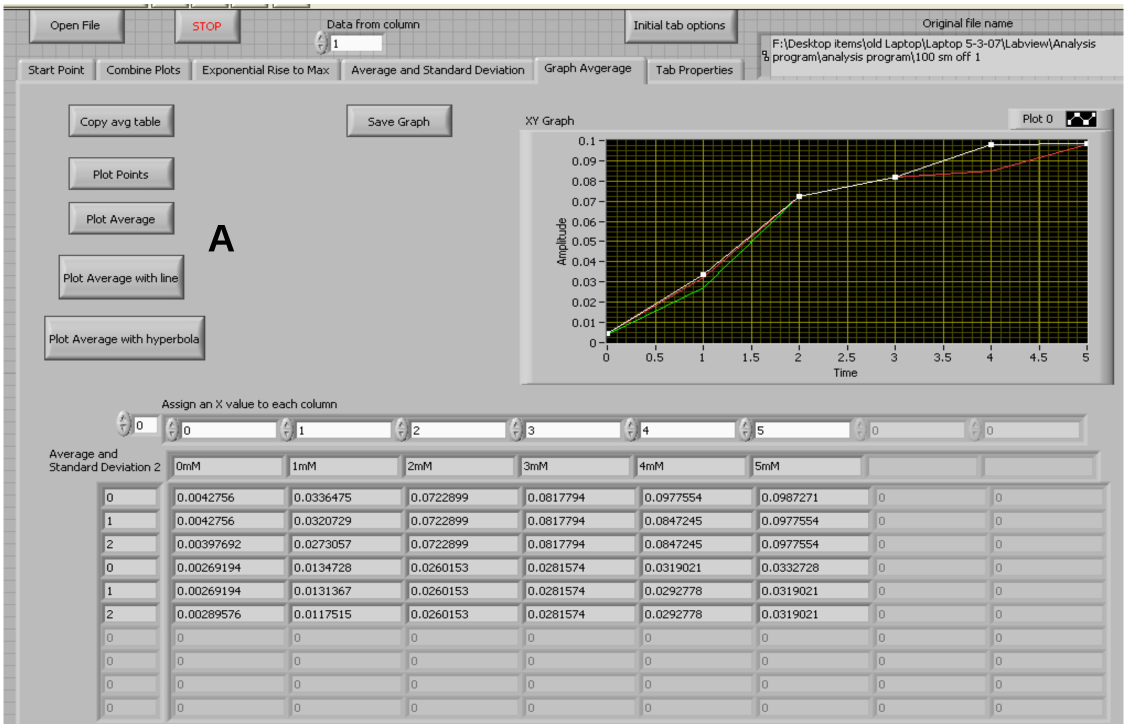

Data from column: 1

Original file name: F:\Desktop items\old Laptop\Laptop 5-3-07\Labview\Analysis program\analysis program\100 sm off 1

Assign an X value to each column: 0 | 0 | 1 | 2 | 3 | 4 | 5 | 0 | 0

Average and Standard Deviation 2	0mM	1mM	2mM	3mM	4mM	5mM		
0	0.0042756	0.0336475	0.0722899	0.0817794	0.0977554	0.0987271	0	0
1	0.0042756	0.0320729	0.0722899	0.0817794	0.0847245	0.0977554	0	0
2	0.00397692	0.0273057	0.0722899	0.0817794	0.0847245	0.0977554	0	0
0	0.00269194	0.0134728	0.0260153	0.0281574	0.0319021	0.0332728	0	0
1	0.00269194	0.0131367	0.0260153	0.0281574	0.0292778	0.0319021	0	0
2	0.00289576	0.0117515	0.0260153	0.0281574	0.0292778	0.0319021	0	0
0	0	0	0	0	0	0	0	0
0	0	0	0	0	0	0	0	0
0	0	0	0	0	0	0	0	0
0	0	0	0	0	0	0	0	0

Figure 2.17. Graph average tab of data analysis program. Copy avg table button copies data from previous tab into table. A) plot points, plot average, plot average with line, and plot average with hyperpola buttons are all plotted in the same graph (top right). Save graph button saves the data from graph.

The "tab properties" (Figure 2.18) portion of the program allows the user to change several properties of the program tabs. Options include the tabs color, enabled or disabled, or whether to display a tab. The *initial tab options* button (Figure 2.18A) return all the tab options to default (especially necessary if the user removed the tab properties display). Tab options are included to increase the speed of analysis by removing unnecessary portions of the code for a given analysis or add color to tabs so that they are easily distinguishable.

Testing of the analysis program was necessary to ensure that the correct values were reported. The start and cutoff positions of a kinetic binding curve were compared with the raw data processed in Excel to ensure that the correct location was being obtained. The selection of a point and zeroing the data function of the LV program was

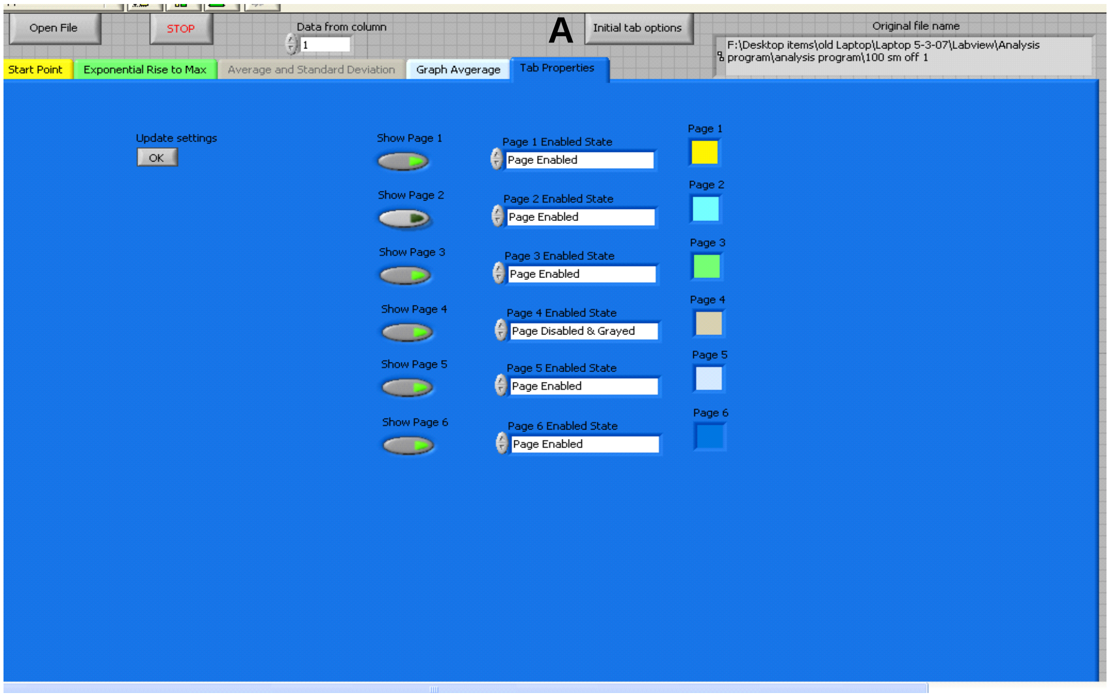

Data from column: 1

Original file name: F:\Desktop items\old Laptop\Laptop 5-3-07\Labview\Analysis program\analysis program\100 sm off 1

Page 1 Enabled State: Page Enabled
Page 2 Enabled State: Page Enabled
Page 3 Enabled State: Page Enabled
Page 4 Enabled State: Page Disabled & Grayed
Page 5 Enabled State: Page Enabled
Page 6 Enabled State: Page Enabled

Figure 2.18. Tab properties tab of data analysis program. Options to show page, disable and gray, and change colors are present for each tab. The update settings button will enable selected options. A) initial tab options returns all tabs to gray and displayed (default).

mimicked in Microsoft® Excel by selecting the same point in both programs and then zeroing the data. The difference between the Excel data and the LV data was determined to be 10^{-15} signal difference. This small discrepancy is attributed to computer round-off. The combination of multiple data sets onto a single graph produced the same results in LV and Excel. Both the average and standard deviation values for the zeroed and raw data were the same in LV and Excel. From the graphing tab, the plot points, plot averaging, and the plot average with line were all duplicated in Excel and provided the same values, demonstrating the ability of the LV program to perform the same functions.

The exponential rise to max calculation and hyperbolic fit functions were checked against Prism (GraphPad), with several different curves. For the exponential rise to max, the values for the K_{obs} and Ymax compared well between LV and Prism. The differences observed were in the number of decimals calculated, causing slight variations in the last digit (the K_{obs} value from LV rounds to the Prism value, Ymax value is different by 0.001). The graphing of a hyperbola was also compared to Prism. Again there was a difference in the number of decimal places (2 digits) reported but the values compared well (the difference in values is 0.0001 for Bmax and the K_D rounds correctly).

2.7 Summary

Programs created:

1. Fourier Transform Program
    a. Detectors: Garry 3000, Garry 3000SD, 2D CCD
    b. Modifications: Temperature monitor, speed increase
2. Correlation Program
    a. Detectors: Garry 3000, Garry 3000SD, 2D CCD
    b. Modifications: Temperature monitor
    c. Other: Correlation extent of integration analysis programs
3. Fourier Transform-Correlation Program
4. Data Analysis program

The work demonstrated here has allowed the use of several different cameras; Garry 3000, Garry 3000SD (Ames Photonics), and three different 2D CCD (Cohu, Basler, AVT). Programming utilized in the laboratory has included the use of a DAQ board, an IMAQ board, and Vision software (NI).

A variety of other programs were written in LV that were not discussed here, including programs to run syringe pumps, test averaging of frames, averaging of pixels, programs to generate sin wave patterns, induce noise to test the correlation program, and further modifications to the Fourier transform and correlation programs. In addition, a program was written that allows control of a multimeter.

The programs reported here have allowed a significant advancement of BSI technology, facilitating the use of new hardware with improved detection limits and the transfer for commercialization and use in other research labs. With the data analysis program, processing data into a presentable form is now significantly less time consuming. Overall, the LV programs have provided the functionality absolutely necessary to expand the use of BSI so that it can be employed to perform real-world molecular interaction studies.

2.8 References

1. Swinney, K., Markov, D. & Bornhop, D.J. Chip-scale universal detection based on backscatter interferometry. *Analytical Chemistry* **72**, 2690-2695 (2000).

2. Wang, Z.L. & Bornhop, D.J. Dual-capillary backscatter interferometry for high-sensitivity nanoliter-volume refractive index detection with density gradient compensation. *Analytical Chemistry* **77**, 7872-7877 (2005).

3. Swinney, K., Markov, D., Hankins, J. & Bornhop, D.J. Micro-interferometric backscatter detection using a diode laser. *Analytica Chimica Acta* **400**, 265-280 (1999).

4. Markov, D., Begari, D. & Bornhop, D.J. Breaking the 10-7 Barrier for RI Measurements in Nanoliter Volumes. *Analytical Chemistry* **74**, 5438-5441 (2002).

5. Bornhop, D.J. et al. Free-solution, label-free molecular interactions studied by back-scattering interferometry. *Science* **317**, 1732-1736 (2007).

6. Latham, J.C., Markov, D.A., Sorensen, H.S. & Bornhop, D.J. Photobiotin surface chemistry improves label-free interferometric sensing of biochemical interactions. *Angewandte Chemie-International Edition* **45**, 955-958 (2006).

7. http://www.omega.com/prodinfo/temperaturecontrollers.html. Temperature Control: Tuning a PID Controller.

8. Born, M. & Wolf, E. *Principles of Optics*, (Cambridge University Press, Cambridge, 1999).

9. Patent Filed.

10. Motulsky, H. & Christopoulos, A. *Fitting Models to Biological Data using Linear and Nonlinear Regression*, (Prism, GraphPad, 2003).

CHAPTER III

TWO-CHANNEL SYSTEM

3.1 Introduction

On-chip backscattering interferometry (BSI) has been shown to be useful for numerous determinations[1-14], including the study of molecular interactions label-free and in free-solution[1]. In the past on-chip measurements have been performed in PDMS and fused silica chips with similar detection limits; 8.3 x 10^{-6} RIU[4] and 7.2 x 10^{-6} RIU[3] respectively. In both cases these measurements were performed in a single-channel configuration, eg. no reference arm to compensate for environmental noise such as temperature fluctuations which is well known to limit the performance of refractive index detectors[15,16].

Several years ago it was shown that significant improvements to the detection limits of BSI could be realized, when using two fused silica capillaries configured in a sample and reference format[15]. By placing the capillaries in essentially identical physical environments and simultaneously illuminating them with a single laser, a detection limit of 5 X 10^{-9} change in RIU was quantifiable. This observation represents a nearly fifty-fold improvement in minimal detectable quantity. In addition, the sample and reference configuration allowed for analyses over very large temperature ranges (>5^0C)[15], thus enabling direct observation of protein folding.

A two-channel on-chip system with a simple optical train giving improved detection limits and substantially reduced sensitivity to environmental conditions which allows broad implementation of BSI, was developed. Advancements realized here, such as mechanical and optical isolation, as well as simplified alignment have also led to improvements that allow expanded use of the single channel configuration of BSI.

3.1.1 Methods

There are numerous approaches to beam splitting, ranging in complexity from a simple flat piece of glass, such as a microscope cover slip, to diffractive optics. When it is desirable to produce two beams of equal intensity, as with the two-channel embodiment of BSI, the most attractive approaches to beam separation consist of a bifurcated fiber optic, a diffractive optic, or a piece of calcite. The use of a bifurcated fiber optic and a calcite polarizer were investigated. For brevity only the approach which used a calcite beam displacer will be described.

3.2 Optical Configuration for Two-Beam BSI

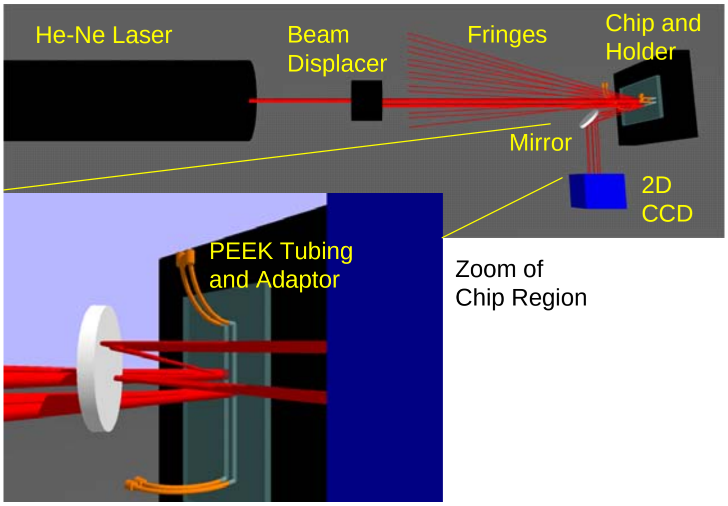

Figure 3.1. Block diagram of two-channel experiment

A block diagram of the experimental setup is shown in Figure 3.1. A linearly polarized He-Ne laser (632.8 nm) is used as the illumination source which is directed at a vertically mounted chip. The beam produced by the He-Ne laser was split by the calcite beam displacer (beam split is based on polarization). The two beams are separated both vertically and horizontally to allow the two beams to impinge on two different channels on a chip, creating fringe patterns. A mirror is used to direct a portion of the fringe patterns onto a two dimensional CCD.

3.2.1 Alignment Procedure

Rotating the laser made it possible to produce two beams of equal intensity by balancing the two polarization states. The two channels on the chip are 1 mm apart. The two beams were aligned with the two channels.

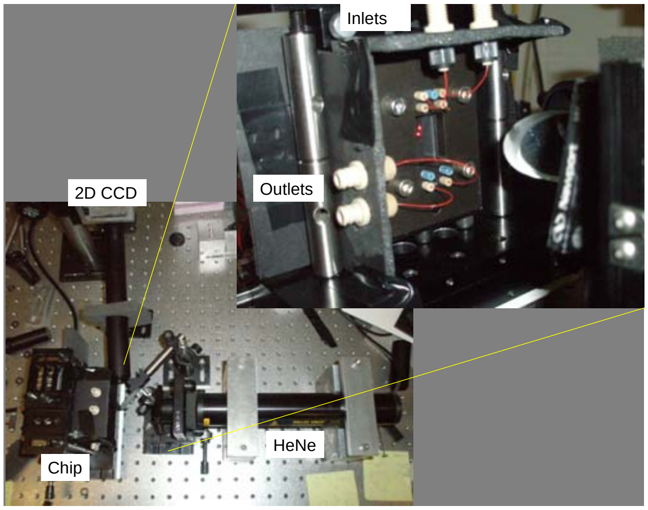

Figure 3.2. Photograph of two-channel BSI system

A mirror was positioned so that a portion of the fringe patterns near the centroid (the direct backscatter region) were directed towards the camera. Instead of a linear CCD array, which could only image one fringe pattern, a two-dimensional CCD camera was utilized to capture the patterns. The camera is positioned about 14 inches away, allowing only one fringe from each channel to appear on the detector. Figure 3.2 shows pictures of the two-channel system.

The two-beam BSI system was modified by mounting the chip vertically (see Figure 3.2). With the chip mounted vertically and with the use of PEEK tubing (which allows access to the channels, see section 3.3), it was possible to build a box around the system that isolated the beam path, optics, and the chip-temperature control assembly. The box serves to minimize the influence of environmental temperature changes (heat: laser and CCD camera, cold: heat sink), thus isolating the system/beam from temperature fluctuations. The box is built in two parts: a foam insulation box to help thermally insulate the system and a black poster-board box to keep the light out, Figure 3.3. The new setup allows experiments to be performed with the room lights on and with other individuals working in the laboratory, which was difficult prior to these modifications.

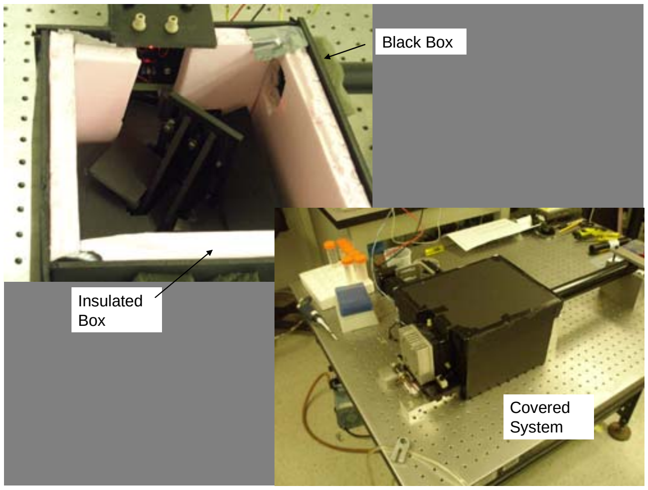

Figure 3.3. Box around BSI system

3.2.2 Position Sensing

While valuable, the Fourier transform (FT) previously utilized[1,17] for BSI fringe position sensing required that the fringe pattern be sinusoidal in order to produce a single frequency, a limitation that required that the outer fringes to be employed. There are two reasons for using the new correlation program described in Chapter 2 to monitor the shift of the fringes in the two-beam experiment: 1) real estate is a premium and 2) it has been found that the inner fringes shift more for the same RI change than the outer, more uniform fringes. As shown in Chapter 2 the correlation approach provides improved results when compared to the FFT methodology.

3.3 New chips

To perform a two-channel BSI experiment it was necessary to construct new dual channel microfluidic chips. After much modeling, these chips were designed and then manufactured by Micronit Microfluidics (Enchida, Netherlands). The chips were made from Borofloat (borosilicate) glass that was isotropically etched[18] to have channels that are about 90 μm wide and about 40 μm deep. As shown in Figure 3.4A the shape of the channels takes the form of a hemisphere.

Serpentine mixers have proven to be useful for mixing on-chip[1]. Three designs of two-channel chips were created (Figure 3.4), one that has two mixers and one outlet, a second that has two mixers and two outlets, and a third with four straight channels. Well locations were determined based on a template provided by Micronit (Figure 3.4B). The two channels were separated by 1 mm in all the designs. Figure 3.4C shows a two-channel chip that has two inlets for each channel, a serpentine mixer, and a single outlet. This design turned out to be problematic as it allowed for cross contamination between the channels because the fluid in the waste well was drawn by capillary action into the channels after injection. The design in Figure 3.4D is similar

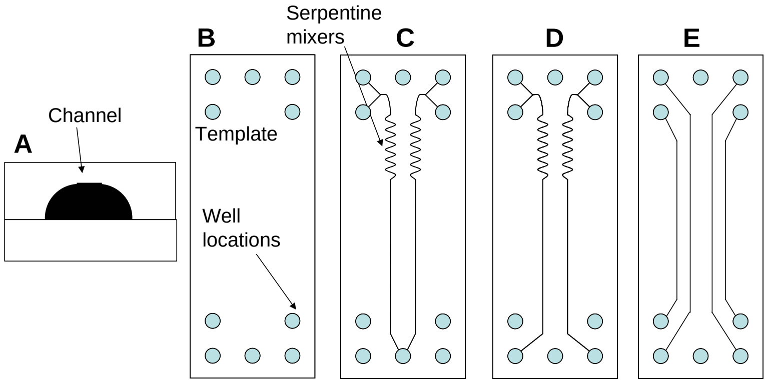

Figure 3.4. New two-channel microfluidic chip designs A) channel cross section B) template C) serpentine mixers, one outlet D) serpentine mixers two outlet E) straight channels

to 5C except that the two channels have individual outlets. The chip depicted in Figure 3.4E is the simplest design consisting of four straight channels.

A new chip mounting assembly was designed and is shown in Figure 3.5. The chip holder serves many functions, including that it allow the chip to be mounted such that it does not move when introducing a sample and it provides a means for low volume microfluidic connections (Upchurch), Figure 3.5. Originally, the holder was to be utilized in the horizontal position as we had done in the past; however, the design was modified to allow for a vertically mounted chip by moving the mounting holes. A thermoelectric cooler, thermistor, heatsink, and temperature controller were still used to control the temperature of the chip holder, chip, and samples in the channels.

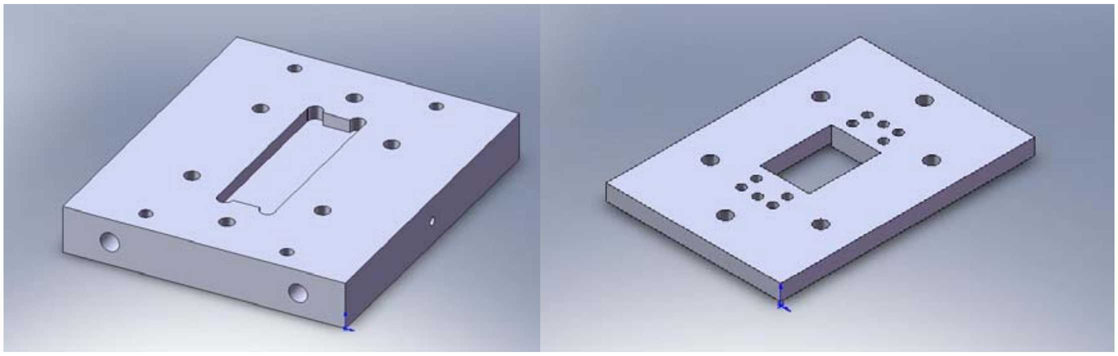
Base Plate
Face Plate

Figure 3.5. Design of the chip holder in SolidWorks

Different types of microfluidic connectors (Upchurch) were utilized to hold the chip in place. Three cone-shaped adaptors were screwed into the face plate and fit into wells that were not connected to the channel (or channels) being used in the experiment. Ferrules and blunt adaptors were used to connect the channel to PEEK tubing and hold the chip against the chip holder. Two methods have been investigated to introduce samples into the chip: 1) PEEK tubing, syringe adaptors, and syringe pumps to push samples into the channel and 2) a syringe adaptor to connect the bottom well by PEEK tubing and a union to connect the top well by PEEK tubing. The top half of the union was removed and the cone-shaped recess was used as a well. A vacuum pump was applied to the syringe adaptor to pull sample into the channel. The flow is stopped and the sample is monitored for one minute.

3.4 Determination of Analytical Figures of Merit

Several experiments were performed to test the new system, including temperature and glycerol calibration curves. The temperature calibration shows how the two channels responded and how well temperature perturbations can be compensated. The glycerol calibration experiments allowed evaluation of sensitivity and reproducibility for the system.

Capitalizing on the fact that dn/dT is on the order of 1×10^{-4} per ^{o}C, a response curve for BSI can be generated by simply changing temperature of the chip. This response plot was generated by placing water into both channels and ramping the temperature of the Peltier unit to change the density (RI) of the fluid in the chip while monitoring the signal (fringe position). A stepwise experiment was done and signal was monitored for one minute at each temperature. Depending on the degree of temperature change, a certain waiting time was necessary for the temperature equilibration (two to five minutes for temperature changes below 0.5°C). Temperature data from BSI was calculated by taking the average and standard deviation of the one minute sections before the temperature was changed.

Figure 3.6 is the result of the experiment of a one degree change made in 0.2°C increments. The green line shows the response of the temperature controller (temperature on right axis). The black and blue lines show the response from the two channels of BSI (signal on left axis). The red line is the trace for C1-C2 displaying the difference between the two channels. The two channels responded similarly; C1-C2 is essentially a flat line. These data demonstrate that over a one degree change, the two-channel system compensates for the temperature change. The average and standard deviations of one minute sections were calculated and the 3σ detection limit based on the noise was determined to be 8.7 x 10^{-7} RIU.

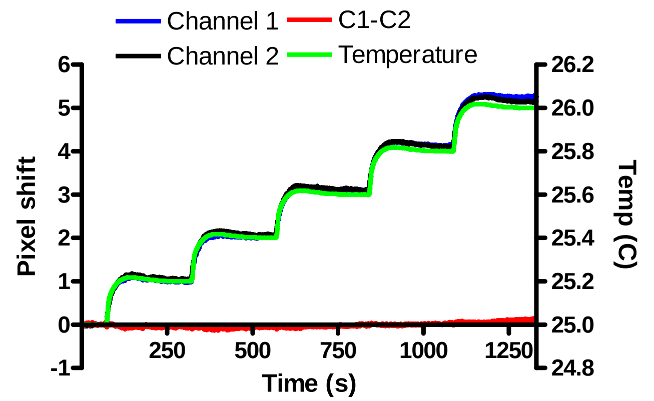

Figure 3.6. BSI results from temperature calibration

To further test the sensitivity of the two-beam BSI, a smaller temperature change was utilized. It is noteworthy that the temperature controller is able to change the temperature by 0.01°C increments manually. It was possible to modify the LV program (Chapter 2) to add a digit to both the set and read temperature that allowed changes and measurement in temperature by 0.001°C increments, which was the smallest increment measurable

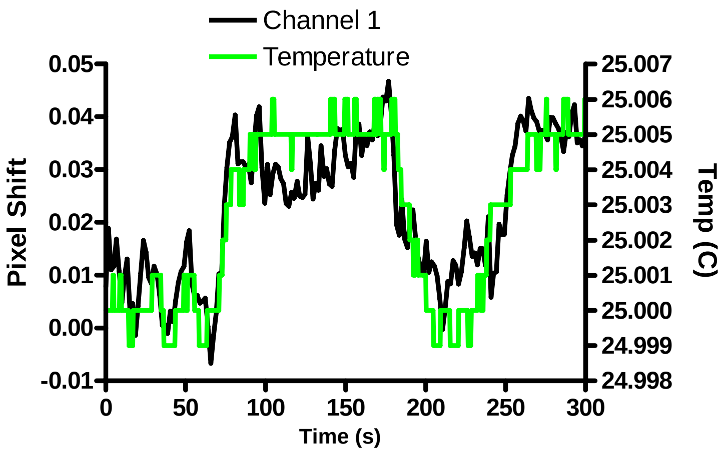

Figure 3.7. BSI results 0.005°C temperature change

with the temperature controller (resulting in digitization of temperature signal in Figure 3.7). The temperature controller was changed by 0.005°C (5 x 10^{-7} RIU). The temperature trace and BSI output are overlaid in Figure 3.7 showing that the signal tracks the temperature change and illustrating that this temperature change was visible over the noise. These data also demonstrate how sensitive BSI is to temperature fluctuations.

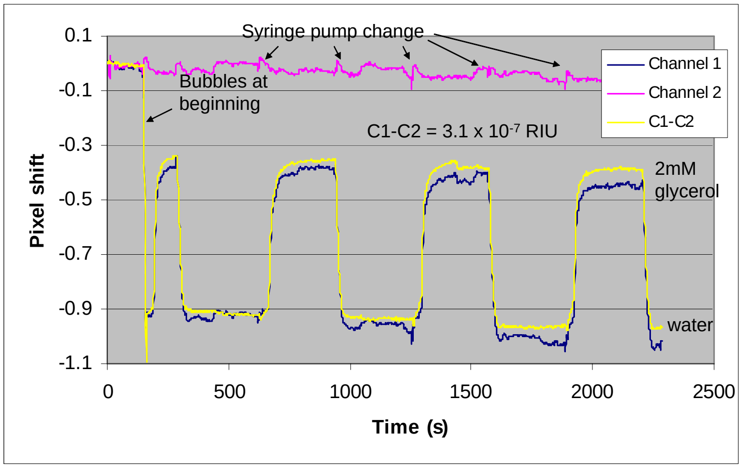

Figure 3.8. BSI measurement of water and 2mM glycerol with syringe pump injection

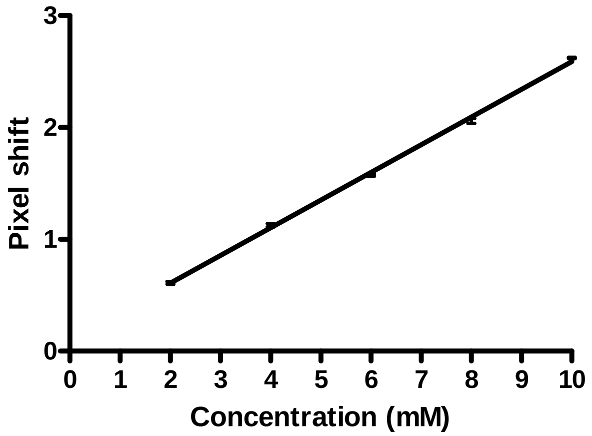

Figure 3.9. BSI syringe pump injection results

For glycerol calibration, the temperature was set at 25°C. Typically five or six glycerol concentrations were used. Initially, syringe pumps were utilized to introduce samples into the channel by pushing sample through. A two-channel mixer chip was used so that two inlets on one channel could be utilized to introduce two separate samples. One syringe pump was used to introduce water and the second syringe pump would introduce a concentration of glycerol. Figure 3.8 shows the response of BSI to repetitively changing the composition of the fluid in the channel between pure water and

2 mM glycerol. Under the conditions employed the detection limit was found to be 3.1 x 10^{-7} RIU. Figure 3.9 shows the results from the triplicate measurements of glycerol with syringe pump sample introduction. The detection limits were calculated as 2.9 x 10^{-6} RIU for the entire run. It was determined that utilizing the syringe pumps allowed mixing between the glycerol and water, causing dilution of samples before analysis. Figure 3.8 shows the advantage of utilizing the two-channel data over a single channel system. The perturbations observed when the syringe pumps were switched on are observed in both the sample and reference channels. As a result, the Ch1-Ch2 data was much smoother, eliminating the noise caused by the syringe pump switch.

To simplify and speed the sample introduction, new adaptors were utilized to introduce samples. A union was connected to the PEEK tubing at the top of the chip and a syringe adapter at the bottom. The union has the top half removed, creating a cone shaped well. Samples are placed into the union and then a vacuum is applied to the syringe adaptor at the bottom, drawing the sample into the channel. This technique allows volumes as low as 1 μL to be placed in the union and easily introduced into the channel by applying a vacuum to the waste reservoir. The glycerol experiment was repeated using this sample introduction method. To further test the system, 0.2 to 1 mM glycerol by 0.2 mM increments were analyzed. Water was

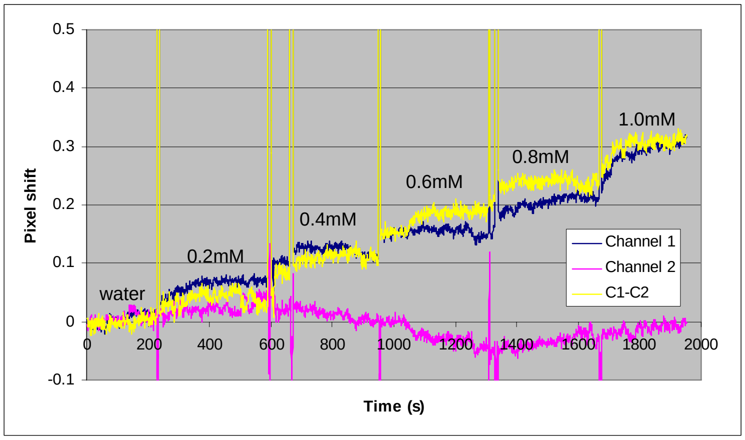

Figure 3.10. BSI results from glycerol calibration

introduced and the fringe pattern was used as a reference for the correlation program. The signal was monitored for one minute. Water was then removed from the channel and the lowest concentration (0.2 mM) of glycerol was introduced into the channel and the signal was monitored again for one minute. The process was repeated for the 0.4, 0.6, 0.8, and 1.0 mM concentrations of glycerol (Figure 3.10). The entire glycerol sample set was analyzed three times.

The average and standard deviation for each one-minute run was calculated for the three runs. The results of the three runs were averaged and a new standard deviation was calculated based on the ability of the system to generate the same value for the same sample, which measures the reproducibility of the system. Measurements were performed in triplicate (Figure 3.11) and the detection limits were 8.3×10^{-7} RIU. For the same data, without reference compensation (Figure 3.12), a detection limit of 4.1×10^{-6} RIU (4.1 mM glycerol) was observed. The data demonstrate a 5x improvement in detection limits by utilizing a sample and reference system. The

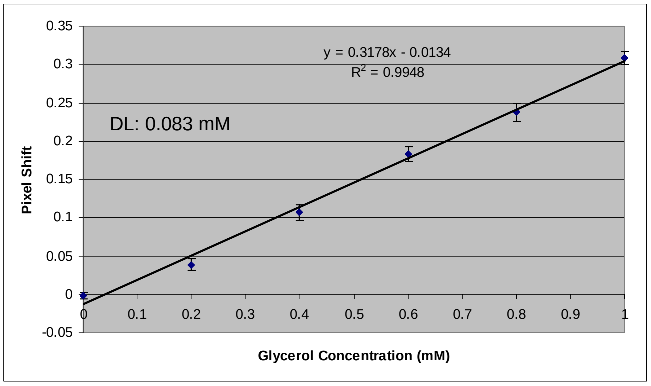

Figure 3.11. BSI results from glycerol calibration (triplicate)

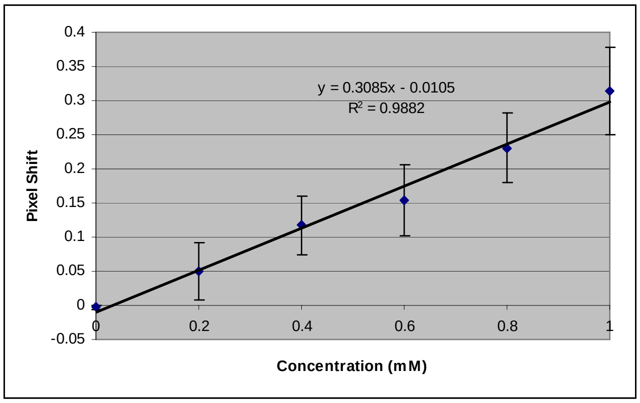

Figure 3.12. Uncompensated glycerol calibration experiment run in triplicate

compensated results are approximately an order of magnitude improvement over previous on-chip BSI experiments.

To further evaluate the ability of the two-channel system to compensate for large environmental perturbations, a glycerol (2-10 mM by 2 mM increments) calibration curve was performed in triplicate. A fourth run of the glycerol curve was performed with the temperature change to 25.2°C for the 4 mM glycerol and then returned to 25°C for the 6 mM glycerol. Similarly, the temperature was changed to 25.5°C for the 8 mM. These two points represent a large environmental change resulting in incorrect measurement utilizing a single channel (Figure 3.13). The fourth run of the 4 and 8 mM glycerol obviously produced a different response than the other runs. By utilizing the sample and reference system, the temperature changes in the samples are compensated (Figure 3.14). These data demonstrate the ability of the two-channel system to compensate for relatively large temperature changes, while monitoring RI changes in samples.

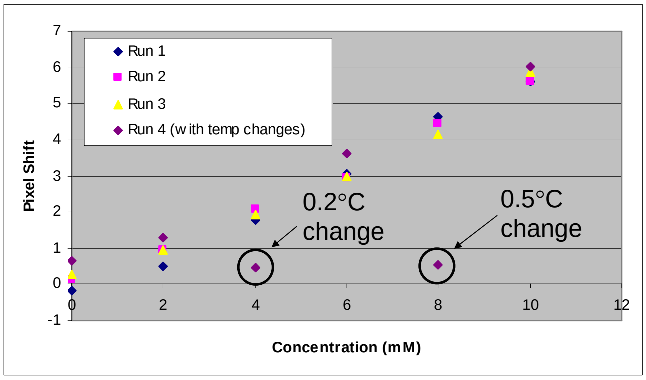

Figure 3.13. Glycerol results from channel 1 with induced temperature changes circled

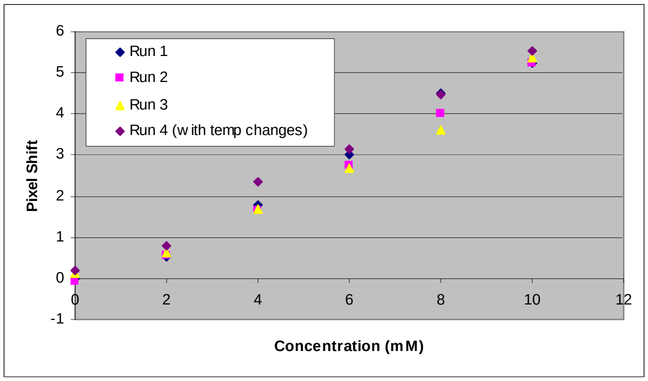

Figure 3.14. BSI glycerol results from compensated data with induced temperature

3.5 Binding Experiment

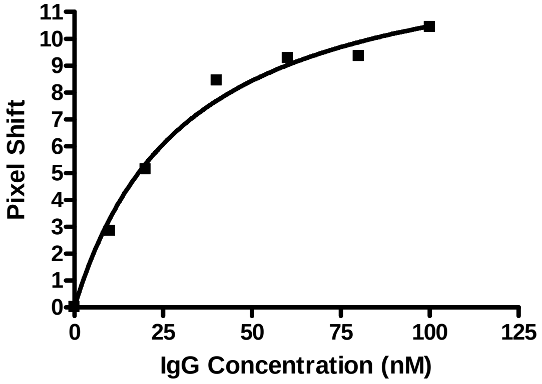

Figure 3.15. Protein A – IgG endpoint binding curve from two channel BSI

The next experiments used to test the new two-channel system were endpoint binding assays. The binding of protein A to IgG was previously studied with BSI[1]. A series of protein A – IgG samples were mixed in Eppendorf tubes. The concentration of Protein A was held constant at 1 µM and the concentration of the IgG was varied, 0, 10, 20, 40, 60, 80, and 100 nM (concentrations after mixing). The samples were introduced into the two channel system and the results are shown in Figure 3.15. A hyperbolic curve, Equation 1:

$$Y = \frac{\left(B_{Max} \times X\right)}{\left(K_D + X\right)} \tag{1}$$

was fit to the data and the K_D was calculated as 31.7 nM, which is within literature values, which rage from 5-34.5 nM[19,20].

3.6 Summary

A two-channel BSI instrument was designed, constructed and tested. Detection limits of 8 x 10^{-7} RIU were obtained using a sample and reference configuration for BSI, which is an approximately ten-fold improvement over previous on-chip detection limit (8.3 x 10^{-6} RIU). The two-channel configuration was able to compensate for large temperature changes (10^{-4} RIU) in BSI. Protein A-IgG binding pair was also studied with the two channel system and produced results within literature values. Two-channel BSI offers significant advancements in measurements of RI with high sensitivity in low volumes.

3.7 References

1. Bornhop, D.J. et al. Free-solution, label-free molecular interactions studied by back-scattering interferometry. *Science* **317**, 1732-1736 (2007).

2. Latham, J.C., Markov, D.A., Sorensen, H.S. & Bornhop, D.J. Photobiotin surface chemistry improves label-free interferometric sensing of biochemical interactions. *Angewandte Chemie-International Edition* **45**, 955-958 (2006).

3. Markov, D.A., Swinney, K. & Bornhop, D.J. Label-free molecular interaction determinations with nanoscale interferometry. *Journal of the American Chemical Society* **126**, 16659-16664 (2004).

4. Markov, D.A., Dotson, S., Wood, S. & Bornhop, D.J. Noninvasive fluid flow measurements in microfluidic channels with backscatter interferometry. *Electrophoresis* **25**, 3805-3809 (2004).

5. Bornhop, D.J. & Hankins, J. Polarimetry in capillary dimensions. *Analytical Chemistry* **68**, 1677-1684 (1996).

6. Swinney, K. & Bornhop, D.J. D-beta-Hydroxybutyrate reaction kinetics studied in nanoliter volumes using a capillary polarimeter. *Applied Spectroscopy* **54**, 1485-1489 (2000).

7. Swinney, K. & Bornhop, D.J. A chip-scale universal detector for electrophoresis based on backscattering interferometry. *Analyst* **125**, 1713-1717 (2000).

8. Swinney, K. & Bornhop, D.J. Miniaturization - Quantification and evaluation of Joule heating in on-chip capillary electrophoresis. *Electrophoresis* **23**, 8 (2002).

9. Swinney, K. & Bornhop, D.J. Noninvasive picoliter volume thermometry based on backscatter interferometry. *Electrophoresis* **22**, 2032-2036 (2001).

10. Swinney, K. & Bornhop, D.J. Quantification and evaluation of Joule heating in on-chip capillary electrophoresis. *Electrophoresis* **23**, 613-620 (2002).

11. Swinney, K. & Bornhop, D.J. Detection in capillary electrophoresis. *Electrophoresis* **21**, 1239-1250 (2000).

12. Swinney, K., Hankins, J. & Bornhop, D.J. Laser-Based Capillary Polarimetry. *J. Cap. Elec. and Microchip Tech.* **006: 3/4**(1999).

13. Swinney, K., Markov, D. & Bornhop, D.J. Chip-scale universal detection based on backscatter interferometry. *Analytical Chemistry* **72**, 2690-2695 (2000).

14. Swinney, K., Markov, D. & Bornhop, D.J. Ultrasmall volume refractive index detection using microinterferometry. *Review of Scientific Instruments* **71**, 2684-2692 (2000).

15. Wang, Z.L. & Bornhop, D.J. Dual-capillary backscatter interferometry for high-sensitivity nanoliter-volume refractive index detection with density gradient compensation. *Analytical Chemistry* **77**, 7872-7877 (2005).

16. Ymeti, A. et al. Realization of a multichannel integrated Young interferometer chemical sensor. *Applied Optics* **42**, 5649-5660 (2003).

17. Markov, D., Begari, D. & Bornhop, D.J. Breaking the 10-7 Barrier for RI Measurements in Nanoliter Volumes. *Analytical Chemistry* **74**, 5438-5441 (2002).

18. http://www.micronit.com/en/home.php.

19. Langone, J.J. Protein-a of Staphylococcus-Aureus and Related Immunoglobulin Receptors Produced by Streptococci and Pneumococci. *Advances in Immunology* **32**, 157-252 (1982).

20. Saha, K., Bender, F. & Gizeli, E. Comparative study of IgG binding to proteins G and A: Nonequilibrium kinetic and binding constant determination with the acoustic waveguide device. *Analytical Chemistry* **75**, 835-842 (2003).

CHAPTER IV

SOLUBILITY STUDIES

4.1 Introduction

Solute solubility is an intrinsic property that must be known to fully understand a chemical or biochemical reaction. In enzyme-catalyst studies, solubility can affect the efficiency of a reaction[1]. The determination of solubility is especially necessary for drug development, in toxicity testing, for bioavailability evaluation, and in clinical applications[2]. It is well known that the solubility of a drug, in the formulation used for delivery, can have a drastic effect on the therapeutic properties as well as its stability. At the current time multi-well drug activity screening methods allow the analysis of many samples in an automated fashion. However, without knowledge of the solubility of the compounds being tested, the results from the activity studies can be flawed allowing for potential drug leads to be missed. At the current time solubility analysis of potential drugs remains slow[3], cumbersome and inaccurate. Therefore a high throughput, low volume, rapid and highly sensitive solubility test would be an invaluable tool. It would speed the drug development process, saving considerable funds and improving efficacy profile of drug candidates, while enabling biochemical research previously not possible.

There are several methods currently used for determining solubility, ranging from potentiometric determinations to light scattering. The technique based on light scattering depends on the formation of particles in samples. One drawback of this method is that the scattering of the beam may be quenched by high concentrations of particles[4], while another is that the solute must form a particle large enough to be detected. Even though the shake flask method provides accurate measurements of solubility, it requires mixing for days, centrifugation, and analysis by HPLC[5,6]. "Potentiometric analysis determines the intrinsic solubility by extracting logarithm of the octanol-water partition (log P) and pK_a parameters from a titration curve of the compound with KOH and is not amenable to high-throughput screening[7,8]."

Solubility is an intrinsic property and it is known that as a species is dissolved in a solvent, the refractive index (RI) of that solution changes. It is also understood that as the saturation limit (solubility point) is reached for a solute, the compound will no longer dissolve. At this point the RI of the mixture should stop changing even though more solute is added. Given this scenario, it should be possible to determine the solubility of a material in essentially any matrix by simply measuring the RI of the solution as a function of added solute concentration. This is the case, and here we demonstrate that Backscattering Interferometry (BSI), a highly sensitive[9], low-volume[10], micro-fluidic based RI sensor[11] can be utilized to perform such a solubility analysis. In this work we have been able to measure aqueous-phase solubility of phenylalanine, cinnamic acid, and hydrocortisone in BSI rapidly, with high sensitivity, and in nanoliter volumes. Furthermore BSI technology employs a simple optical train that consists of a laser, channel in a microfluidic chip, and a transducer. It is therefore inherently amenable to high throughput and realizes the advantages of low sample requirements.

4.2 Experimental Section

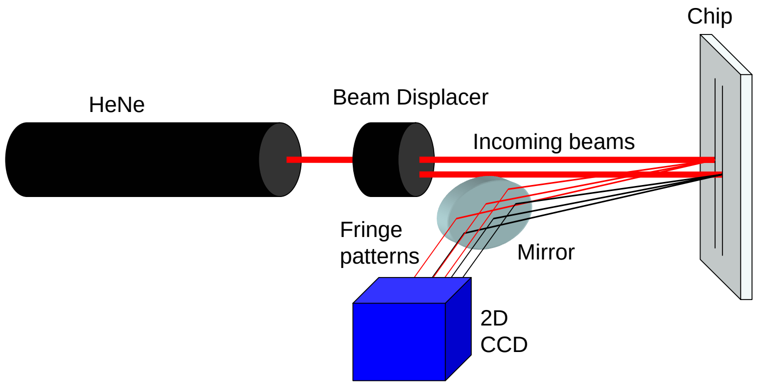

One of the two fringe patterns is shown in black for ease of viewing.

Figure 4.1. Block diagram of two channel experiment

A two channel BSI system was utilized to perform the solubility studies described here. Figure 4.1 displays the basic optical train consisting of a He-Ne laser, beam displacer, microfluidic chip, mirror, and a 2D CCD. The beam displacer creates two beams based on polarization. The two beams hit separate channels on the microfluidic chip providing sample and reference channels so that environmental changes can be eliminated. A portion of the fringe pattern from both channels is directed by the mirror onto a 2D CCD. This technique allows for measurement of RI by monitoring the positional shift of the fringe pattern. Using software written in house (see Chapter 2), the positional shift of the fringe is quantified by measuring the number of (or portion of) pixels that the fringes shifts with changes in RI, calculated in real time. By observing the change of the fringe pattern as solutions of increasing concentration of the solute are introduced (after sonication and equilibration at 25°C), a calibration curve of pixel shift vs. change in RI was generated. When the samples reach the solubility point, the solution is saturated. Any additional solute added will not dissolve in the sample.

4.2.1 Methods

Three solutes were studied to show that RI changes can be used to determine solubility. These were phenylalanine (Sigma, purity ≥98%), cinnamic acid (Fluka, purity ≥99%), and hydrocortisone (Sigma, purity ≥98%,). In all cases samples were prepared with masses of the solute that exceeded the solubility limit and without concern of saturation point, e.g. we prepared phenylalanine samples at a "target" concentration > 0.16M. For each of the solutes several saturated samples were created.

For the phenylalanine solutions an appropriate mass in order to prepare 25 mL solutions ranging in *targeted concentration* of 0.14-0.195 M, 0.005M increments, was placed into volumetric flasks and diluted with DI water. The flasks were sonicated for approximately 40 min and placed into a water bath at 25°C for two hours.

To prepare the cinnamic acid solutions, an appropriate mass was placed into 50 mL flasks to make concentration of 0.5 to 5.0 mM in 0.5 mM increments. The samples were diluted with DI water and were sonicated then allowed to reach equilibrium in a water bath at 25°C.

The hydrocortisone solutions were prepared by adding the appropriate mass of solute to make 1 L solutions of 500-950 μM concentration (50 μM increments). DI water was used to dilute the samples and the solutions were sonicated and placed into a water bath at 25°C.

DI water served as the blank and all samples were introduced into the BSI system, allowed to stabilize, equilibrate in the channel and then the RI signal was monitored for one minute. The lowest-concentration solution of the calibration curve (for example 0.14 M for phenylalanine) was introduced first, the channel was rinsed and then next higher concentration solution analyzed. The entire concentration series was measured in triplicate for each solute system.

The signal in BSI is an average pixel shift, which is related to the RI change that gives rise to a fringe shift. This pixel shift value was observed for 60 seconds and was used to represent the signal. The three-trial pixel-shift averages were plotted versus concentration. Error bars are the standard deviation of the three independent runs.

4.3 Results and Discussion

Figure 4.2 shows the response of the BSI system for the solutions of phenylalanine. This determination shows that the RI (fringes shift measured as a pixel shift) continues to change with increasing concentrations until the saturation point. As more solute is added to a saturated solution, there is an intersection point in the plot. At this point no additional change in the RI is detected, indicating that the composition of the mixture is not changing, and that the added mass is not soluble, indicating that the solubility limit has been reached. To our knowledge, this is the first report showing that by simply measuring the concentration dependence of the RI of a solution, the solubility can be quantified. The average and

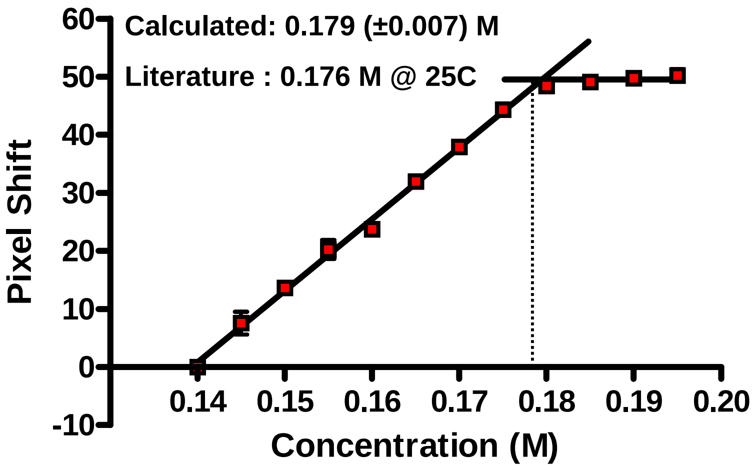

Figure 4.2. BSI results from the solubility of Phenylalanine

standard deviation for all points were calculated and are plotted in Figure 4.2. Note that the reproducibility of the measurement is excellent. The slope and intercept (with calculated errors) of the line for the values which are obtained when the samples are obviously not saturated was calculated (slope = 1240.1, Intercept = -172.9). Next we assume that the point of saturation can be determined by finding the location where the signal ceases to change with increasing concentration. For our determination, this is where the fringe stops shifting, or on the plot, where no additional change in pixel position occurs with an increase in added solute. So by determining the intersection point for the two data sets, those with a constant change and those with no change, the y value (pixel shift position) can be determined. Then using this value the concentration for the solubility limit can be extracted (the X value). This process is done by taking the average pixel shift and standard deviation values from unchanging data points to determine the intersection point (the Y value). Then this Y value is used in the line equation from above to determine the new X value, or the solubility point. Standard statistical evaluations yield the error in this measurement. Therefore by simply measuring where the RI stops changing as a function of concentration with BSI (Figure 4.2) we

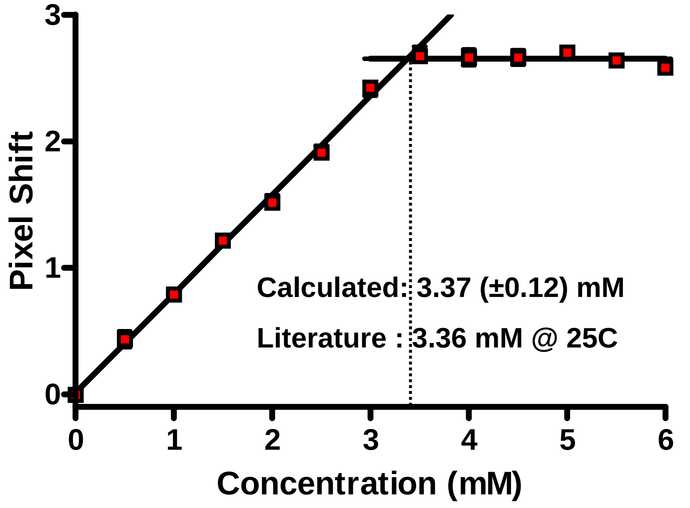

Figure 4.3. Cinnamic acid results from BSI

determine or calculate the solubility for Phenylalanine to be 0.179 (±0.007) M at 25°C. This solubility value corresponds well with the value reported in the literature of 0.176M at 25°C[12] and was determined rapidly with just nanoliters of sample.

Results from the second solubility experiment, performed with cinnamic acid, are displayed in Figure 4.3. Using the same approach for determining the intersection point of the plot(s) as noted above, the solubility was determined by BSI to be 3.37 (±0.12) mM. The literature value for the solubility of cinnamic acid is 3.36 mM[12]. Again, this resulted in excellent agreement with the published solubility value. Hence by simply monitoring the RI change as a function of solute concentration the solubility point of the sample can be rapidly determined.

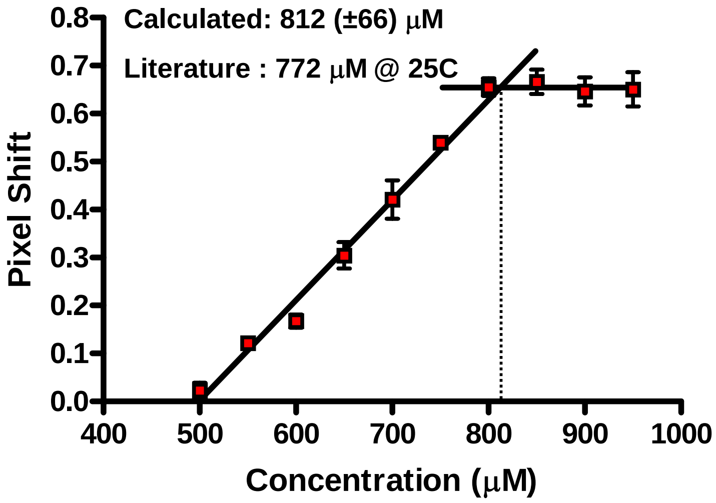

Figure 4.4. Hydrocortisone results from BSI

To test our approach with a more challenging system, we chose to determine the solubility point of hydrocortisone, a sample with a much lower solubility than cinnamic acid or phenylalanine. Hydrocortisone was analyzed similarly, and the data from this BSI solubility determination is displayed in Figure 4.4. Here we determine the solubility to be 812(±66) μM. The solubility literature value of hydrocortisone is 772 μM[12].

Measurement uncertainties in Figure 4.4 indicate that the low concentrations of hydrocortisone produce a BSI signal. While the hydrocortisone measurement is within literature values, the increased uncertainties in the measurements of the samples, particularly observed in the saturated samples, demonstrates the noise limitation of the analysis technique. Filtering samples and additional rinsing of the channel would ensure more accurate measurement of the individual samples. It may also be possible to reduce the uncertainty of the solubility point by analyzing samples closer to the solubility point. The results from the BSI solubility experiments are summarized in Table 4.1.

Table 4.1. Summary of BSI solubility point calculations

Sample	BSI Calculated	Literature
Phenylalanine	0.179 (+/-0.007) M	0.176 M
Cinnamic acid	3.37 (+/- 0.12) mM	3.36 mM
Hydrocortisone	812 (+/- 66) μM	772 μM

4.4 Summary

The experiments presented here demonstrate that solubility can be determined rapidly, with reasonable accuracy and using just nanoliter volumes with BSI. By determining the intersection of the line of the calibration curves before the solubility point and the average of points after, it is possible to determine solubility by monitoring refractive index changes. We have demonstrated the determination of solubility of phenylalanine, cinnamic acid, and hydrocortisone (hundreds of mM to hundreds of μM) can be found using BSI as an RI detector. The solubility points measured correspond well to literature values. These examples demonstrate the potential of BSI to rapidly measure solubility points in nanoliter volumes.

4.5 References

1. Faber, K. *Biotransformations in Organic Chemistry*, (Springer, Berlin, 2000).

2. Thomas, G. *Medicinal Chemistry: An Introduction*, (John Wiley & Sons, Ltd., Chichester, England, 2000).

3. Lloyd, D.K., Goodall, D.M. & Scrivener, H. Diode-Laser-Based Optical-Rotation Detector for High-Performance Liquid-Chromatography and Online Polarimetric Analysis. *Analytical Chemistry* **61**, 1238-1243 (1989).

4. Bevan, C.D. & Lloyd, R.S. A high-throughput screening method for the determination of aqueous drug solubility using laser nephelometry in microtiter plates. *Analytical Chemistry* **72**, 1781-1787 (2000).

5. Bergstrom, C.A.S., Norinder, U., Luthman, K. & Artursson, P. Experimental and Computational Screening Models for Prediction of Aqueous Drug Solubility. *Pharmaceutical Research* **19**, 182-188 (2002).

6. Venkatesh, S., Li, J.M., Xu, Y.H., Vishnuvajjala, R. & Anderson, B.D. Intrinsic solubility estimation and pH-solubility behavior of cosalane (NSC 658586), an extremely hydrophobic diprotic acid. *Pharmaceutical Research* **13**, 1453-1459 (1996).

7. Avdeef, A., Berger, C.M. & Brownell, C. pH-metric solubility. 2: Correlation between the acid-base titration and the saturation shake-flask solubility-pH methods. *Pharmaceutical Research* **17**, 85-89 (2000).

8. Takacs-Novak, K. & Avdeef, A. Interlaboratory study of log P determination by shake-flask and potentiometric methods. *Journal of Pharmaceutical and Biomedical Analysis* **14**, 1405-1413 (1996).

9. Bornhop, D.J. et al. Free-solution, label-free molecular interactions studied by back-scattering interferometry. *Science* **317**, 1732-1736 (2007).

10. Swinney, K., Markov, D. & Bornhop, D.J. Chip-scale universal detection based on backscatter interferometry. *Analytical Chemistry* **72**, 2690-2695 (2000).

11. Wang, Z.L. & Bornhop, D.J. Dual-capillary backscatter interferometry for high-sensitivity nanoliter-volume refractive index detection with density gradient compensation. *Analytical Chemistry* **77**, 7872-7877 (2005).

12. Budavari, S. (ed.) *The Merck Index*, (Merck Research Laboratories, 1996).

CHAPTER V

ACRYLIC CHIPS

5.1 Introduction

Several different types of fluidic systems have been used in BSI; capillaries, glass chips, and PDMS chips[1-3]. The differences between the three categories are the geometry of the fluidic channel, material compliance, reactivity (protein adsorption), transparency, and refractive index (RI). Shape of the channel is an important parameter toward determining the fringe pattern, and therefore the sensitivity of BSI[2]. Capillaries can be viewed as a circular channel within a circular container[1]. Glass chips are isotropically etched and have a semi half circle geometry (a half circle with a small flat portion in the center) contained in a flat wafer[2], while PDMS chips have rectangular channels contained in a rectangle of elastomer[3]. Even though there are many differences between these BSI optics, all three types of fluidic systems produce fringe patterns that have been utilized to effectively monitor the RI of samples contained in the channel. This chapter presents a new fluidic system for BSI that was created and analyzed.

Microfluidics has been used in a variety of applications including fabrication of valves, pumps, and flow sensors[4] as well as in analytical techniques including chromatography, fluorescence, and electrophoresis[5]. To date three approaches have been used for preparation of microfluidic systems: (1) isotopic etching in glass or fused silica; (2) bead blasting in glass; and (3) molding in plastic. Isotropically etched glass chips are useful but are expensive and difficult to manufacture. Furthermore the types of shapes that can be formed in glass or fused silica somewhat limit the applications, for example using etching techniques it is hard to make chips that have variable channel depths or a short restriction. While the PDMS work culminated in a paper in *Science*[6], PDMS chips are also limited. First the PDMS manufacturing process can take days and second the final product is somewhat compliant (soft) so that the channel dimensions can change leading to erroneous signals in our interferometer.

Because of these and other limitations, such as the growing need for different channel designs and rapid production/prototyping, a new method of chip manufacturing was introduced. To further the field of microfluidics, we have set out to create microfluidic chips out of acrylics in a process that is rapid, inexpensive and which produces an optical quality device. It is also desirable that the chips be cheap enough to be disposable and rapid to manufacture. Using the process developed, it will also be possible to prepare chips with variable physical properties such as rigidity and clarity.

5.2 Acrylic Chip – Fabrication of Cylindrical Channels

As noted previously and shown with theory and experimental data [2], BSI has the best performance when the shape of the channel or illuminated object is fully cylindrical. Therefore channels with this shape are desirable. One approach would be to make two chips with identical half circle cross sections and fuse them together. Alignment and other tolerance problems make this approach unattractive. As an alternative procedure an assembly was made to hold a rod/wire (Figure 5.1), allowing acrylic to be cured around the wire. Removal of the wire produces an acrylic cube with circular channel.

PDMS was poured into a Petri dish, degassed, and put in the oven at about 70°C over night. Four rectangles were cut out of the PDMS (2 of 22 x 13 mm and 2 of 18 x 13 mm). On a standard glass slide (clean 75.6 x 25 x 1 mm) the four rectangles of the PDMS were placed to create a box (a small amount of acrylic was used on each corner to hold the box together), Step 1 of Figure 5.1. A wire (0.26 mm diameter) was punched through the two end pieces, suspending the wire in the air (height of wire can vary), Step 2 of Figure 5.1.

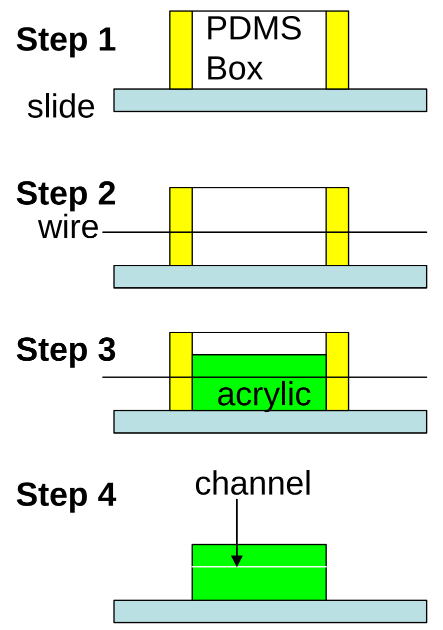

Figure 5.1. Steps for acrylic chip. Step 1: Create PDMS box on slide. Step 2: Place wire through box. Step 3: Pour acrylic and cure. Step 4: Remove wire and PDMS box.

Acrylic (DYMAX® Corporation) was poured over the wire in the box to a depth of about 2-3 mm (Step 3 of Figure 5.1). The apparatus was exposed to UV light for 30 seconds. Next the PDMS was pealed off of the chip and the wire was removed (Step 4 of Figure 5.1). The result of these procedures was a chip with dimensions of about 22mm x 17mm x 2mm (dependent on the box and acrylic depth) with a channel with a circular cross section that has a diameter approximately the size of the wire (0.26 mm). Both the wire (if cleaned) and PDMS pieces can be reused. Final chips are ready for use in about two hours.

Two different methods for accessing the channel have been utilized, producing wells or utilizing PEEK tubing. Well creation is done before the curing process by positioning the wire through tall, thin blocks of PDMS. In step 2 of Figure 5.1, the blocks of PDMS would be inside the PDMS box with the wire through the two blocks.

After curing, the wire and blocks in the center of the chip are removed, leaving holes that have access to the channel. With the well access in these chips, the channel exits at the end of the chip are unnecessary and are sealed with acrylic to ensure that solutions flow through the channel. For the use of PEEK tubing to access the channel, the acrylic chip is created as described in Figure 5.1 and then PEEK tubing is inserted into each end of the channel. Acrylic is used to seal the channel ends around the PEEK tubing allowing solutions to easily flow through the channel (Figure 5.2). While the PDMS box method has produced functioning chips, a device to hold the wire and create wells will make the process easier and more reproducible.

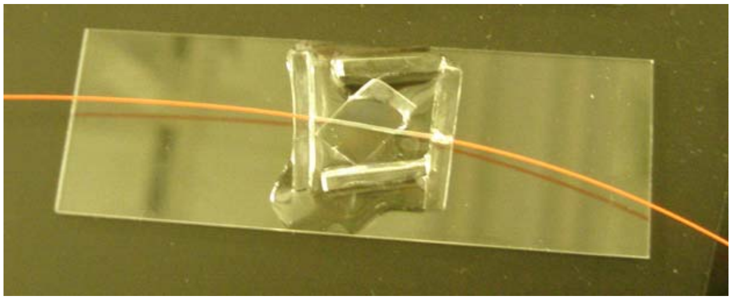

Figure 5.2. Acrylic chip with PEEK tubing connected

To ensure a region of the chip has a flat surface with good clarity for the probe beam of BSI, a piece of Mylar film is placed on top of the chip before the curing process (the film is removed after curing). The Mylar has been especially useful for improving the clarity of certain acrylics. Some acrylic samples turn a slight yellow when exposed to UV, but with the piece of Mylar film, it is possible to create a clear window to utilize as a detection zone.

5.3 Acrylic Chip Testing

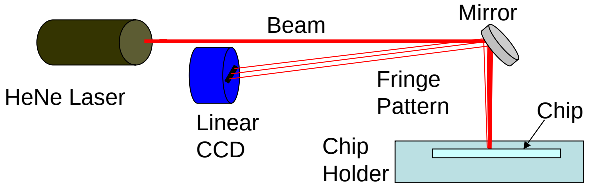

Figure 5.3. Diagram of BSI setup

An acrylic chip was created using the procedure described above utilizing a 0.26 mm diameter wire and PEEK tubing for sample introduction. The chip was placed into the BSI system (Figure 5.3). A He-Ne laser beam was directed onto the chip by a mirror. A fringe pattern was created and directed onto a linear CCD (Ames Photonics). A Fourier transform program written in LV (NI) was used to monitor the fringe pattern shift as the refractive index (RI) of the sample inside the channel changed. The fringe pattern generated by the acrylic chip is shown in Figure 5.4. The fringe pattern has a high contrast ratio and produced a single frequency (as shown in the insert of Figure 5.4) monitored with the Fourier transform program.

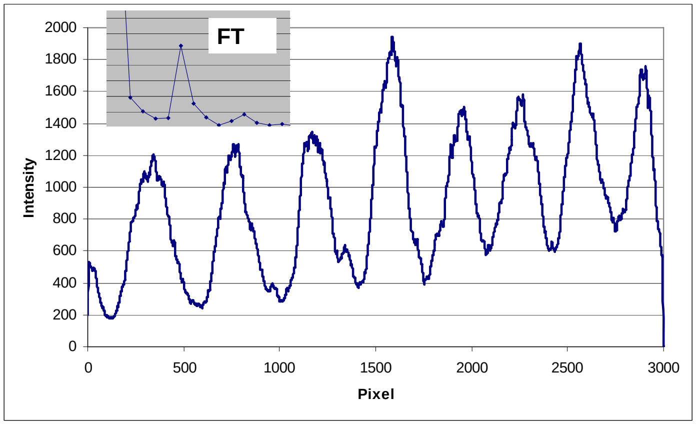

Figure 5.4. Fringe pattern from acrylic chip

Samples of glycerol, 0-25 mM, were introduced into the system utilizing a syringe adaptor at the end of the PEEK tubing and solutions were injected by a syringe. The reproducibility of the signal is demonstrated in the inset of Figure 5.5. Three samples were measured: 25 mM glycerol, water, and again 25 mM glycerol. A detection

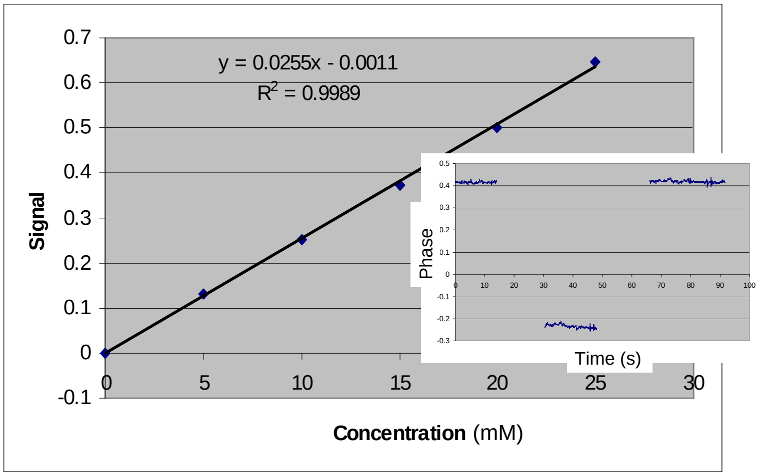

Figure 5.5. Data from acrylic chip on BSI

limit of 0.87mM (8.7 x 10^{-6} RIU) glycerol was calculated. The probe volume of the acrylic chip was 170 nL.

5.4 Summary

The preliminary data shown here demonstrates a new method of chip fabrication in acrylics, creating cylindrical channels. It is also demonstrated that the acrylic chips are functional in BSI. Further development of these procedures will provide acrylic chips that could take the place of many PDMS or glass chips. Inexpensive, disposable, rapidly produced acrylic chips are an advancement in the field of microfluidics.

5.5 References

1. Tarigan, H.J., Neill, P., Kenmore, C.K. & Bornhop, D.J. Capillary-scale refractive index detection by interferometric backscatter. *Analytical Chemistry* **68**, 1762-1770 (1996).

2. Swinney, K., Markov, D. & Bornhop, D.J. Chip-scale universal detection based on backscatter interferometry. *Analytical Chemistry* **72**, 2690-2695 (2000).

3. Latham, J.C., Markov, D.A., Sorensen, H.S. & Bornhop, D.J. Photobiotin surface chemistry improves label-free interferometric sensing of biochemical interactions. *Angewandte Chemie-International Edition* **45**, 955-958 (2006).

4. Gravesen, P., Branebjerg, J. & Jensen, O.S. Microfluidics-a review. *Journal of Micromechanics and Microengineering* **3**, 168-182 (1993).

5. Regnier, F.E., He, B., Lin, S. & Busse, J. Chromatography and electrophoresis on chips: critical elements of future integrated, microfluidic analytical systems for life science. *Trends in Biotechnology* **17**, 101-106 (1999).

6. Bornhop, D.J. et al. Free-solution, label-free molecular interactions studied by back-scattering interferometry. *Science* **317**, 1732-1736 (2007).

CHAPTER VI

ON-CHIP POLARIMETRY

6.1 Introduction

If two isomers of a molecule differ only by being non-superimposable mirror images, they are called optical isomers or enantiomers. Because of their handedness, or chirality, enantiomers and solutions of them exhibit optical activity. That is, they rotate the plane of polarized light. One enantiomer rotates the plane of polarization clockwise (as seen by an observer looking toward the light source) and is labeled (+), or (d-) for dextrorotatory; while the other enantiomer rotates the plane of polarization counter-clockwise and is labeled (-), or (l-) for levorotatory. R- and S- are also used to specify enantiomeric pairs, based on their structures. In chemical reactions the enantiomers behave identically, but when reacting with other chiral compunds, the d- can react differently than the l- enantiomer. Examples of chiral molecules in nature are numerous. Smell and taste are based on olfactory receptors which are themselves chiral, and thereby discriminate enantiomers. In fact the reaction selectivity or specificity commonly seen in many biological systems can lead to life or death[1]. Often for pharmaceuticals one enantiomer will be ineffectual, or even toxic, while the other elicits the desired therapeutic outcome[2].

Measurement of optical activity is essential in the pharmaceutical, biotechnology, and food industries. It is particularly important in the development of new drugs[3], with the vast majority of medicines and drug metabolites being chiral and the worldwide sale of single-enantiomer dosages exceeding $147 billion in 2002[2]. Increasingly stringent guidelines by the FDA for single-enatiomer drugs will necessitate efficient methods for measuring chirality. High throughput screening, coupled with combinatorial chemical methods and parallel synthesis, is accelerating the number of leads in drug discovery[4-8]. "Directed evolution" methodologies[8-10] are being applied to the development of modified enzymes, which are used as biocatalysts to facilitate synthesis of precursors, intermediates, and important end product compounds. A significant number of chiral drug precursors are now produced by these enzyme catalyzed processes. As noted by Reetz and others[11-13], one of the main challenges of combinatorial asymmetric catalysis and directed evolution is the requirement to screen enzyme libraries with 10^4 to as many as 10^7 members[14]. Recent C&E News reports[3,15] emphasize the need for accessible tools for the production and analysis of chiral compounds. M.G. Finn[16] as well as M. Tsukamoto and H.B. Kagen[17] have published reviews outlining advancements in methodologies for the determining enantiomeric excesses (ee), noting the significant analytical challenges of all things combinatorial. Here we report an analytical tool, the on-chip polarimeter, as part of the solution for moving this field from its infancy to common industrial practice.

Polarimetry is a well-known optical technique that has been used to characterize optically active compounds since Biot's work in 1815. It can provide quantitative measurement of optical activity or chirality which is proportional to concentration of the chiral molecule and is nondestructive. In a conventional polarimeter, plane-polarized light passes through the sample region and the analyzer, a second polarizer, is rotated to block the light, producing minimal signal at a photo-transducer. Adding an optically active sample rotates the plane of polarization, allowing more light to be transmitted by the analyzer, resulting in a detector signal increase. To quantify the optical rotary power of the sample, the analyzer is rotated to again minimize the detector signal giving an angle between the original and final orientations of the analyzer. The signal in polarimetry is proportional to the optical activity of the molecule, its concentration, and the optical path length. To have adequate rotation angle sensitivity, conventional polarimeters employ large cells with path lengths of 10-20 cm. In addition they have moving parts limiting applicability and miniaturization.

A number of groups have worked towards improving sensitivity while reducing sample size of polarimetry systems and assays. Yeung and Bobbitt made one of the first attempts to miniaturize polarimetry, by adding a Faraday rotator to the optical train to modulate the polarization state of the beam and then using a lock-in-amplifier to obtain the optical activity measurements. This system was used with microbore liquid chromatography and was able to detect 11 ng of fructose[18]. Bruno and co-workers used a refractive index equalizer for polarimetry in HPLC[19], improving accuracy in determining enantiomeric excess (ee) of (R,S)-1-phenyl-ethanol by eliminating pseudo-rotation. A commercial laser-based polarimetric detector made by PDR-CHIRAL, Inc., similar to the one reported by Yeung and Bobbitt has been reported to have detection limits of 25 microdegrees and has a variety of sample volumes, depending on the sample cell[20].

In 1996, our group demonstrated for the first time that polarimetric measurements could detect changes in optical activity at the micromolar level in nanoliter volumes with no sensitivity to refractive index perturbations[21]. The capillary polarimetric detector (CPD) has a simple optical train based on a 4-mW polarized He-Ne laser, a Polarcor™ polarizing plate with an extinction ratio of 1:10,000 to further purify the polarization state of the beam, a fused silica capillary tube, and a transducer. The device has been used to analyze D-β-hydroxybutyrate at the picomole level[22], for the determination of absolute optical activity[23], and for flowing stream analysis[24]. We also showed that CPD fringes could be interrogated using an FFT[25] for real-time nanoscale polarimetry. The polarimetry work done by the Bornhop research group has been heralded as "a quantum leap in sensitivity"[3,16].

Recently, there have been two reports demonstrating medium-high throughput polarimetry[26,27]. Gibbs, et. al.[26] reported on the development of an imaging polarimeter for chiral screening. A 575W diffused theatrical spotlight was polarized prior to traversing an array of wells. The exiting light traverses an analyzing polarizer before being imaged onto a camera with a telecentric lens. The investigators show that with a relatively large volume cell (3.53 mL), a path length of 12 cm, ±0.08° rotation can be quantified and that dextrose solutions of 0.5° and 1.0° rotations could be discriminated from water in denser plates including 384 and 1536-well plates. Sucrose invertase converting sucrose to dextrose and fructose (a reduction of optical rotation) could be monitored as a function of time. The authors note limitations suggesting that; a) better light sources (laser) and b) higher crossed-polarizer extinction coefficients would be necessary to improve the polarimetric resolution and facilitate determination with short path length, standard multi-well plates. Bornscheuer and Schonfeld used a commercial micro-polarimeter in concert with a pipetting robot to enable the assay of α-amino acid

Table 6.1. Figures of merit for recently developed small-volume polarimeters

Work performed by	System	Sample volume (microliters)	Detection limit (microdegrees)	Measurements performed in	System complexity
Gibbs, Uehara, Nguyen, and Willson	Imaging polarimeter [26]	75	80000	Multi-well plates or sample array	Low
PDR-Chiral	Advance laser polarimeter [20]	43	25	Flowcell	High
Schonfeld and Bornscheuer	Medium throughput polarimeter [27]	40	1000	Flowcell	Medium
Bobbitt and Yeung	Detection in microbore LC [18]	1	15	Flowcell	Medium
Bornhop and Hankins	Capillary Polarimetric Dectector [21]	0.03	100	Capillaries	Low
Dotson and Bornhop	On-Chip Polarimeter (Data shown here)	0.0018	18000	Microfluidic channels	Low

racemase activity[27] from a model enzyme, glutamate racemase, from *Lactobacillus fermintii*. The specific activity was determined to be 111.4 mdeg/min, which corresponds to 45.7 µmol/min per mg of purified enzyme. Racemase activity could be measured in a 96-well plate using purified enzymes. Here the limitations are modest sensitivity and microliter volume requirements.

Here we build on our successes with CPD by demonstrating on-chip polarimetry (OCP) in two formats, one completely devoid of an analyzer optic. OCP has a very simple optical train, excellent sensitivity, nanoliter detection volume, is relatively insensitive to solute refractive index changes, and is compatible with HT formats.

6.2 Experimental

Preliminary evaluation of the on-chip polarimeter interference pattern indicated an absence of high frequency fringes as seen in CPD[21]. The direct backscatter on-chip polarimeter (DOCP) was therefore designed similarly to conventional polarimetry in that it utilizes an analyzing plate. DOCP (Figure 6.1A) consists of a helium neon (He-Ne) laser (632.8nm), two Glan-Thompson polarizers, a half-wave plate, a fused silica chip with an isotropically etched channel, and a detector. Despite the lack of high frequency fringes, the multipass advantage of backscattering interferometry is realized with this unique polarimetry configuration giving excellent sensitivity to changes in optical activity, even in 90 µm wide by 40 µm deep microfluidic channels.

In DOCP, an isotropically etched channel, with a 40 µm radius and a 10 µm flat section channel (Figure 6.1B), was illuminated with the laser beam. Employing a He-Ne laser with a beam diameter of 0.6 mm yields a polarimeter with a 1.8 nL probe volume. The beam passes through a neutral density filter (to attenuate intensity), a Glan-

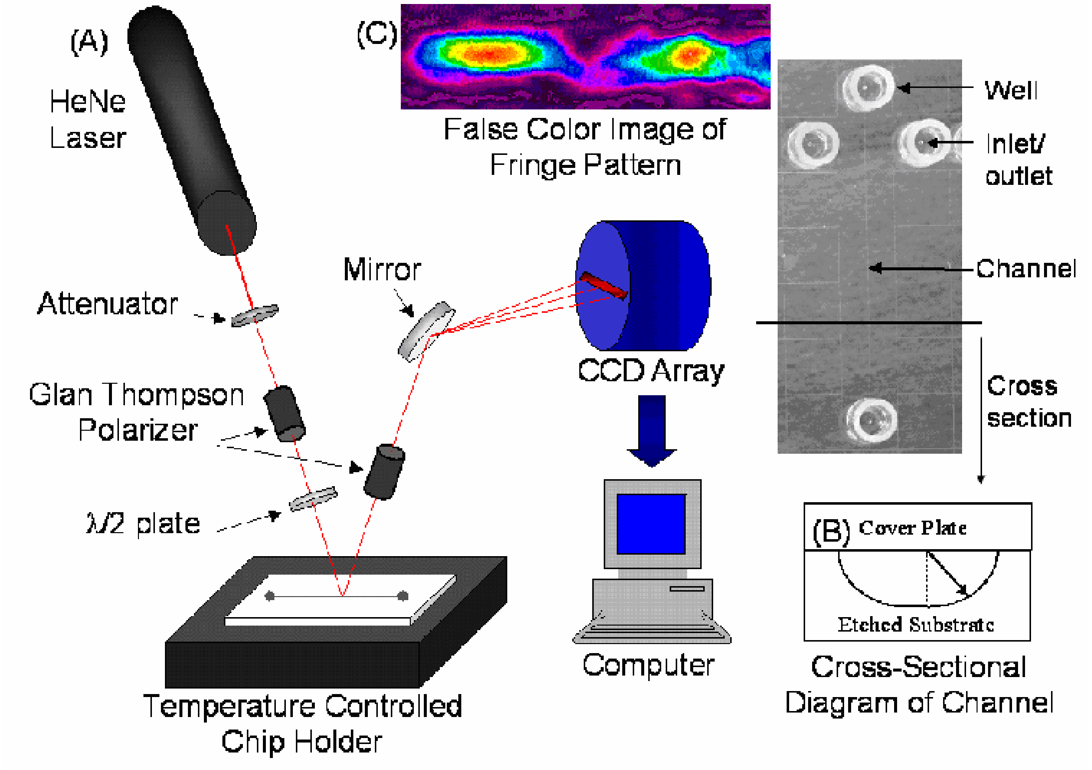

Figure 6.1. (A) Block diagram for on-chip polarimeter; (B) chip cross-section (C) false color fringe pattern (two fringes)

Thompson polarizer to further purify the beam polarization, and a half-wave plate for rotation of the plane of polarization. Typical fringe patterns are displayed in Figure 6.1C. The chip was securely mounted onto an aluminum black anodized block with a Peltier cooler regulated by a high precision temperature controller in order to minimize temperature perturbations.

In DOCP, a section of the fringe pattern, the first three fringes adjacent to the centroid (bright fringe in the direct backscatter from laser), was passed through the analyzing polarizer and then directed onto a linear charge-coupled device (CCD) that is connected to a computer for storage and characterization. Since this system uses a two-polarizer configuration, the polarimetric signal is encoded in the intensity of the fringe pattern.

To demonstrate how DOCP performs well as a polarimeter, Malus' Law response was evaluated by measuring the intensity output (sensitivity of the system) as a function of polarization state of the incoming beam. With water in the microfluidic channel, the half-wave plate was rotated in five degree increments to impart a change in polarization plane of the laser beam with respect to the channel. This plot (shown in Figure 6.2) of intensity versus polarization state illustrates that DOCP response follows a $\cos^2$ function with the rotation in plane of polarization as predicted by Malus' Law. This plot also allows us to determine the positioning of maximum intensity change for any induced rotation, providing the optimal location for quantifying solute induced rotation.

The system was then used to discriminate between R and S isomers using the relative increase or decrease of intensity caused by the rotation of the plane of polarization in opposite directions by each isomer. S- and R- mandelic acid are well-characterized and have a high specific rotation, $[\alpha]^{25} = +154^{\circ}$ and $[\alpha]^{25} = -153^{\circ}$ respectively, and were therefore selected to test the response of this system. Solutions of 1 to 5 mM glycerol, R- or S-mandelic acid, were drawn into the channel and the change in the polarimetric signal (integrated intensity of the first three fringes in the pattern) was recorded. Glycerol solutions were used to demonstrate that OCP is insensitive to RI changes. Water was used as a reference (0 mM).

To expand on these observations, we slightly modified the system to employ a CCD-based laser beam analyzer (LBA) as a detector. R-mandelic acid at concentrations of 1, 2, 3, 4, 5, 25, 50, 75, and 100 mM were analyzed.

An enzymatic reaction was chosen to further demonstrate the applicability of DOCP. By using the Michaelis-Menten model[28,29], the enzyme – substrate (E-S) interaction is described as

$$E + S \underset{k_{-1}}{\overset{k_1}{\rightleftarrows}} ES \xrightarrow{k_2} E + P \quad , \tag{1}$$

where P is the product. The velocity of the reaction in Eq. 1 is defined by the Michaelis-Menten equation,

$$Velocity = \frac{V_{MAX} \cdot [S]}{[S] + K_M} \quad , \tag{2}$$

where V_{max} is the maximum velocity and K_m is the Michaelis constant. The Lineweaver-Burke equation,

$$\frac{1}{V} = \frac{1}{V_{MAX}} + \frac{K_M}{V_{MAX}} \cdot \frac{1}{[S]} \quad , \tag{3}$$

derived from Eq.2, demonstrates how V_{max} and K_m are determined by varying the substrate concentration and constructing a double reciprocal plot (1/V versus 1/[S])[28,29].

To test our system, phenylalanine ammonia lyase (PAL) has been used to convert L-phenylalanine, an optically active molecule (α = -34°)[30], to trans-cinnamic acid (optically inactive) and ammonia. This reaction was selected because it can also be monitored on a spectrometer measuring the absorbance of the product, cinnamic acid, at 290 nm[31-33].

The PAL (from Rhodoturula glutinis) enzyme (Sigma-Aldrich) was placed into a 50mM Tris-HCl buffer (pH = 8.5) at 45 mUnits/mL. A solution of 15 mM L-phenylalanine (Sigma-Aldrich) and a 300 mM Tris buffer were also created. Five reactions were created with 300 uL of varying substrate concentrations, 300 uL of 300 mM Tris buffer, and 300 uL of 45 mu/mL PAL in 50 mM Tris. Final L-phenylalanine concentrations were 3.33, 2.5, 1.67, 0.83, and 0.083 mM. The solutions were mixed and 20 μL was then introduced into the on-chip polarimeter to fill the well and then a portion was pulled into the microfluidic channel. A 300 μL portion of the mixture was introduced into a small-volume cuvette and the change in absorbance was monitored on a conventional UV-Vis spectrometer (Shimadzu PharmaSpec UV-1700). Spectrometric measurements were taken every 30 seconds for 30 minutes.

6.3 Results and Discussion

Intensity of the fringe pattern vs. half-wave plate angle was plotted (Figure 6.2) to demonstrate Malus' Law. DOCP response was fitted to a $\cos^2$ function, producing an R^2 value of 0.999, indicating excellent correlation with Malus' Law[34].

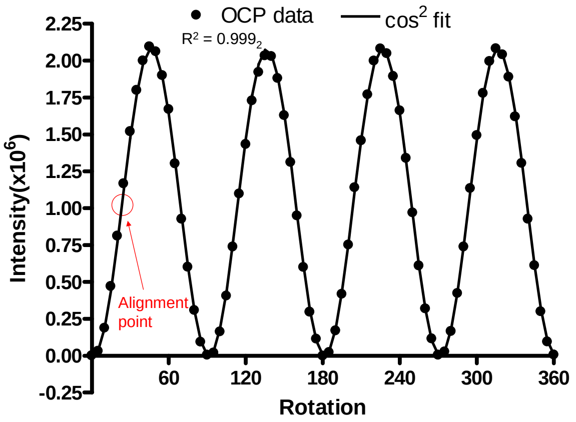

Figure 6.2. Response of DOCP to rotation of plane of polarization

The solutions of R-, S- mandelic acid and glycerol were also analyzed utilizing intensity measurements. The resulting plot of intensity versus concentration is shown in Figure 6.3 where the error bars are the standard deviations of four replicates in less than 1 second. The trend seen in the blue plot indicates that increasing glycerol concentrations and thus the RI substantially results in a nominal signal change, an exciting observation given that RI changes fundamentally limit the performance of conventional optical activity measurements[19].

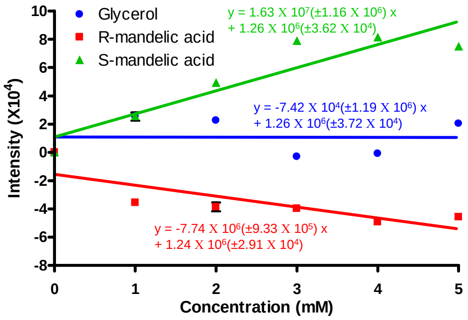

Figure 6.3. Results from glycerol, R- and S-mandelic acid solutions

Figure 6.3 also illustrates that DOCP is functioning as a polarimeter. The green and red plots show that the R-mandelic acid has a negative slope and the S-mandelic acid has a positive slope. This observation demonstrates that: 1) the system can detect an optically active molecule with a signal increase that is concentration dependent; 2) the R and S enantiomers produce opposite effects in the system. We attribute the presence of noise to poor control of environmental conditions and the inherent intensity instability produced by He-Ne lasers. This data demonstrates that polarimetric measurements have been accomplished on-chip with backscatter interferometry.

Once the linear CCD array was replaced with the LBA, the resolving power of the new system was evaluated using the micro rotation stage mounted Glan Thompson polarizer. Rotation of the polarization plane in one-degree increments, starting at the alignment point, yields a graph (not shown) of intensity versus degree change ($y = 1.96E+06x + 8.22E+06$, $R^2 = 0.999$). Then, an intensity versus concentration {R-mandelic acid at 1, 2, 3, 4, 5, 25, 50, 75, and 100 mM} plot was generated (not shown), which gave a linear response ($y = 42532x + 1E+07$, $R^2 = 0.991$). Using these two plots, the response of the DOCP in degrees changed vs. concentration can be generated, seen in Figure 6.4. Error bars on the plot are the standard deviation from four independent runs with R-mandelic acid, giving a 3σ detection limit of 1.55mM glycerol or 0.018 degrees, which corresponds to 0.42 ng of mandelic acid.

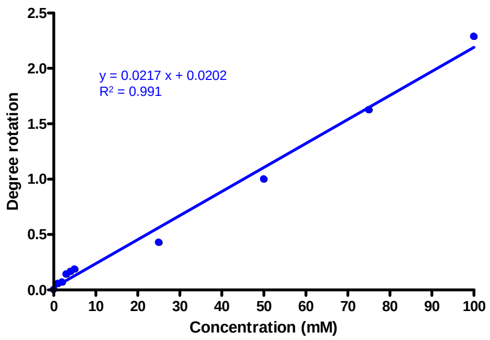

Figure 6.4. Concentration of R-mandelic acid response of DOCP

This detection limit represents a 4-fold improvement in sensitivity over other multiplex systems (0.08 degrees)[26]. Conventional polarimetry has better performance than DOCP, but for example the factor of 720 sensitivity that is lost compared to the PDR-Chrial system but accompanied by a factor of 2.4×10^4 reduction in volume[35].

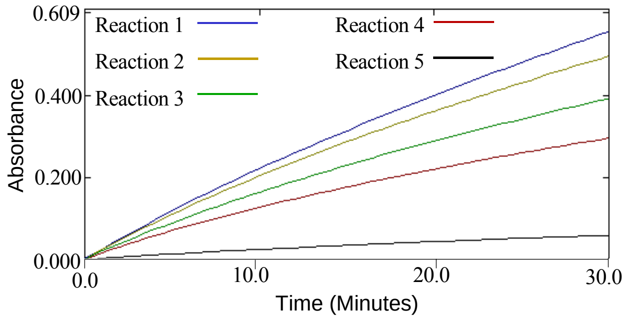

Figure 6.5. Results from PAL reactions in spectrometer (290 nm)

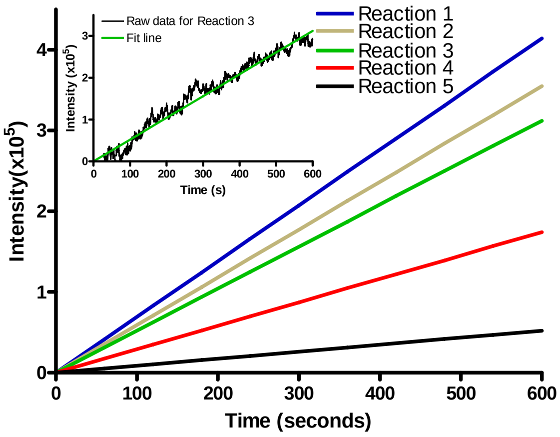

Figure 6.6. PAL reaction with five different concentration of L-phenylalanine measured in OCP, raw data for reaction 3 shown in insert

Enzyme catalysts are important because chemical reactions in biological system rarely occur without them[36]. Enantioselective enzyme reactions serve as an excellent evaluation platform for DOCP as the change in optical activity can be monitored in a microfluidic channel utilizing small amounts of sample. Here an enzyme reaction, phenylalanine ammonia lyase (PAL) with L-Phenylalanine to produce trans-cinnamic acid and ammonia was performed simultaneously on both the UV-vis spectrometer and DOCP. Five solutions were made with a final concentration of 3.33, 2.5, 1.676, 0.83, and 0.083 mM L-phenylalanine when combined with PAL and the reactions were then measured. Figure 6.5 shows the results of the five reactions from the UV-vis spectrometer. For the DOCP, intensity changes of three fringes were integrated and measurements were taken at 0.5 Hz for 10 minutes. Figure 6.6 shows the results from the DOCP, with raw data shown for reaction 3.

The plots of velocity vs. substrate concentration for each reaction and both detection schemes are shown in Figure 6.7 which indicates that response as a function of time follows the same trend. Normalization (for reaction 1, velocity = 1) of these two plots allows direct comparison of DOCP response and UV-Vis absorption (not shown, similar to Figure 6.7). To determine K_m and V_{max} it was necessary to plot $1/V_0$ vs. 1/[S]. The Lineweaver-Burke reciprocal plots of the normalized data for both determination methods should and do give a linear response seen in Figure 6.8 (normalized). Measurement for the reactions as determined by DOCP closely follows that produced by the established method using UV absorption. K_m values can be calculated by extracting the linear equations in Figure 6.8, solving for the x intercept and then taking the negative inverse of this value. Performing this calculation yields a K_m of 0.94 mM using UV-absorption and 0.52 mM using DOCP. These values are both within the range reported in the literature for such determinations (0.12-5 mM). UV-Vis

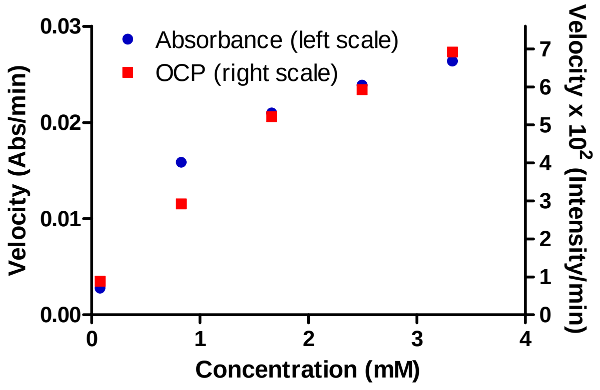

Figure 6.7. PAL velocities in OCP and UV-vis

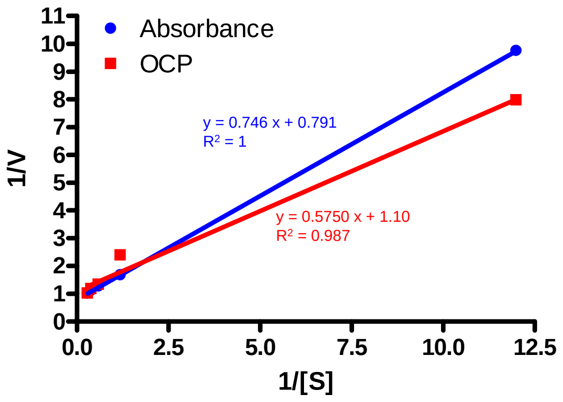

Figure 6.8. Double reciprocal plot of normalized PAL reactions

with DOCP clearly demonstrates the potential for using DOCP for monitoring quantifying kinetics of enzyme transformation reactions in ultra-small volumes.

6.4 Side Scatter Embodiment of OCP (SOCP):

A more detailed evaluation of the OCP interference pattern has indicated that at wider scattering angles, ~80°, (Figure 6.9) there are regions of the pattern ***dominated*** by high frequency fringes. As shown in Figure 6.10, these high frequency fringes (dashed lined) attenuate when the incoming polarization plane is rotated. This preliminary observation is extremely important and suggests that a side scatter embodiment of OCP could be constructed, facilitating polarimetry **without** a second polarizer (analyzer). SCOP would have an even simpler transduction method than CPD, because the absence of low frequency fringes allows the total intensity to be measured rather than extracting the high frequency component as in CPD[21]. Currently the SOCP configuration does not allow the determination of absolute optical activity, yet as shown below, it does allow for discrimination between R- and S-isomers.

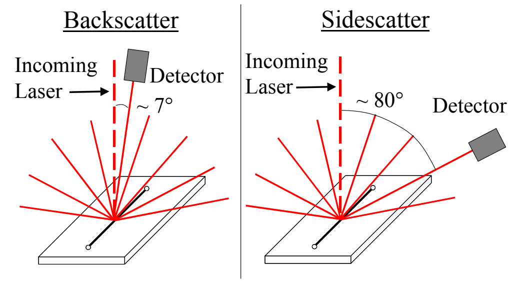

Figure 6.9. D- vs. S- OCP

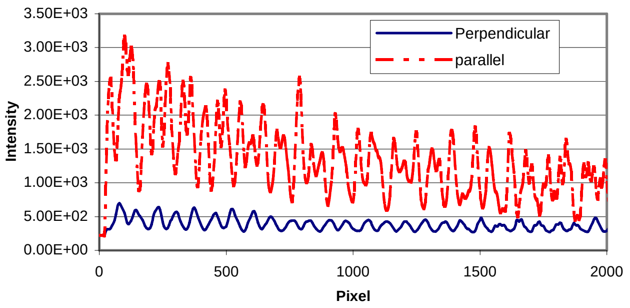

Figure 6.10. Sidescatter fringe pattern response to polarization state

For SOCP, rotation of the half-wave plate produced a $\cos^2$ relationship as predicted by Malus' Law (Figure 6.11). Further evaluation of SOCP was performed with the half-wave plate positioned at 134°. Again solutions of glycerol, R- and S-mandelic

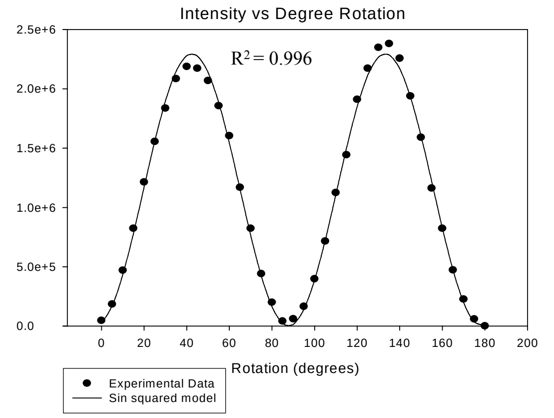

Figure 6.11. Results from rotation of plane of polarization in sidescatter-OCP

were employed. Figure 6.12 depicts the results showing that SOCP has little sensitivity to RI changes, and responds oppositely to the two enantiomers as desired. Interestingly, the intensity for R- increases in this half-wave plate configuration. Rotating the half-wave plate to 44° would produce a negative slope for R-mandelic acid as before (Figure 6.3).

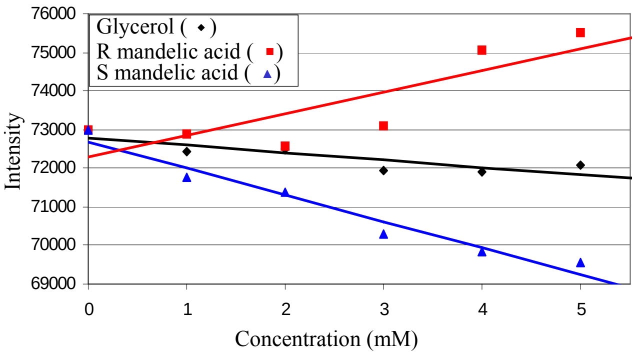

Figure 6.12. Results from sidescatter-OCP

The concentration detection limits were determined to be 0.04 mM for S-mandelic acid, which is about 20 times higher than the best commercial instrument but was accomplished in a 30,000 times smaller volume (1.8 nL probe volume). Mass detection limits of 7.2 x 10^{-14} moles were determined for SOCP, 1,500 times better than any reported optical activity determination. Improvements are predicted to facilitate 10-100 times better performance for SOCP, by compensating for intensity fluctuations of the laser by utilizing a sample and reference system.

Performing ee measurements in nanoliter volumes is of paramount importance [11] because of the need to ensure the purity of samples, as it is possible for only one enantiomer can be useful as a therapeutic. In order to evaluate the potential of performing ee determinations with SOCP, mixtures of R- and S-mandelic acid in proportions of 9:1, 7:3, 5:5, 3:7, and 1:9 (at a total solute concentration of 5 mM) were prepared. The half-wave plate positioned at 134°, and the response of SOCP measured for these solutes as were solutions of the pure solutes. Results are shown in Figure 6.13. As expected the R-mandelic acid gave the highest intensity corresponding to the data observed in Figure 6.12. Also as desired the SOCP intensity decreases with decreasing concentration of R-mandelic acid. While a very preliminary result, Figure 6.12 indicates that enantiomeric excess can be measured utilizing the SOCP.

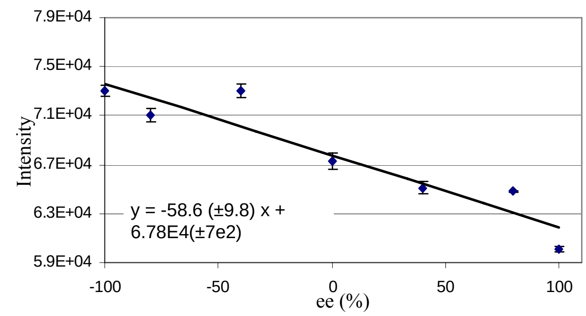

Figure 6.13. Enantiomeric excess study (SOCP), ee is with respect to S enantiomer

6.5 Conclusions

These results represent a first attempt to perform polarimetry on-chip. Using a version of backscattering interferometry[37-39], it was possible to quantify 0.02 degrees or concentrations of 0.04 mM for S-mandelic acid or 7.2 x 10^{-14} moles within a probe volume of merely 1.8 nL. The short term noise detection of 0.02 degrees indicates that there is room for improvement in the system, and modifications are in progress that should provide greater stability and improved reproducibility for both configurations of OCP, including the implementation of a sample and reference channel configuration. Our observations of fringes in the side-scatter configuration indicate that an exceedingly simple optical train could be employed for very high sensitivity, ulta-low volume polarimetry. A preliminary study of enantiomeric excess was studied with the side-scatter polarimeter. We are confident that the sample and reference modification will increase the sensitivity of this instrument and allow for the realization of a powerful technique with broad industrial application.

6.6 References

1. Buhot, C. et al. Alteration of the tertiary structure of the major bee venom allergen Api m 1 by multiple mutations is concomitant with low IgE reactivity. *Protein Science* **13**, 2970-2978 (2004).

2. Rouhi, A.M. Chiral roundup - As pharmaceutical companies face bleak prospects, their suppliers diligently tend the fertile fields of chiral chemistry in varied ways. *Chemical & Engineering News* **80**, 43-50 (2002).

3. Rouhi, A.M. Taking a measure of chiral riches - Researchers respond to high demand for ways to measure enantioenrichment quickly. *Chemical & Engineering News* **80**, 51-57 (2002).

4. Borman, S. Combinatorial chemistry. *Chemical & Engineering News* **80**, 43-57 (2002).

5. Fox, S.J., Yund, M.A. & Jones, S.F. Assay Innovations Vital to Improving HTS. *Drug Discovery and Development*, 40-43 (2000).

6. Kuhlmann, J. Drug Research: From the Idea to the Product. *International Journal of Clinical Pharmacology and Therapeutics*, 541-552 (1997).

7. Resetar, S. & Eiseman, E. Anticipating Technological Change: Combinatorial Chemistry and the Environment. (EPA, 2001).

8. Reetz, M.T. Combinatorial and evolution-based methods in the creation of enantioselective catalysts. *Angewandte Chemie-International Edition* **40**, 284-310 (2001).

9. May, O., Nguyen, P.T. & Arnold, F.H. Inverting enantioselectivity by directed evolution of hydantoinase for improved production of L-methionine. *Nature Biotechnology* **18**, 317-320 (2000).

10. Arnold, F.H. Design by directed evolution. *Accounts of Chemical Research* **31**, 125-131 (1998).

11. Reetz, M.T. New methods for the high-throughput screening of enantioselective catalysts and biocatalysts. *Angewandte Chemie-International Edition* **41**, 1335-1338 (2002).

12. Abato, P. & Seto, C.T. EMDee: An enzymatic method for determining enantiomeric excess. *Journal of the American Chemical Society* **123**, 9206-9207 (2001).

13. Korbel, G.A., Lalic, G. & Shair, M.D. Reaction microarrays: A method for rapidly determining the enantiomeric excess of thousands of samples. *Journal of the American Chemical Society* **123**, 361-362 (2001).

14. Cohen, N., Abramov, S., Dror, Y. & Freeman, A. In vitro enzyme evolution: the screening challenge of isolating the one in a million. *Trends in Biotechnology* **19**, 507-510 (2001).

15. Rouhi, A.M. Chiral chemistry. *Chemical & Engineering News* **82**, 47-62 (2004).

16. Finn, M.G. Emerging methods for the rapid determination of enantiomeric excess. *Chirality* **14**, 534-540 (2002).

17. Tsukamoto, M. & Kagan, H.B. Recent advances in the measurement of enantiomeric excesses. *Advanced Synthesis & Catalysis* **344**, 453-463 (2002).

18. Bobbitt, D.R. & Yeung, E.S. Direct and Indirect Polarimetry for Detection in Microbore Liquid-Chromatography. *Analytical Chemistry* **56**, 1577-1581 (1984).

19. Maystre, F., Bruno, A.E., Kuhner, C. & Widmer, H.M. Enhanced Polarimetric Detection in Hplc Using a Refractive-Index Equalizer. *Analytical Chemistry* **66**, 2882-2887 (1994).

20. PDR-CHIRAL. Development of a New Laser Based Polarimetric Detector and Its Application to High-performance Liquid Chromatography. in *HPLC* (1998).

21. Bornhop, D.J. & Hankins, J. Polarimetry in capillary dimensions. *Analytical Chemistry* **68**, 1677-1684 (1996).

22. Swinney, K. & Bornhop, D.J. D-beta-Hydroxybutyrate reaction kinetics studied in nanoliter volumes using a capillary polarimeter. *Applied Spectroscopy* **54**, 1485-1489 (2000).

23. Swinney, K., Nodorft, J. & Bornhop, D.J. Nanoliter volume polarimetry. *Applied Spectroscopy* **56**, 134-138 (2002).

24. Swinney, K., Nodorft, J. & Bornhop, D.J. Capillary-scale polarimetry for flowing streams. *Analyst* **126**, 673-675 (2001).

25. Markov, D.A., Swinney, K., Norville, K., Lu, D. & Bornhop, D.J. A Fourier analysis approach for capillary polarimetry. *Electrophoresis* **23**, 809-812 (2002).

26. Gibbs, P.R., Uehara, C.S., Nguyen, P.T. & Willson, R.C. Imaging polarimetry for high throughput chiral screening. *Biotechnology Progress* **19**, 1329-1334 (2003).

27. Schonfeld, D.L. & Bornscheuer, U.T. Polarimetric assay for the medium-throughput determination of alpha-amino acid racemase activity. *Analytical Chemistry* **76**, 1184-1188 (2004).

28. Faber, K. *Biotransformations in Organic Chemistry*, (Springer, Berlin, 2000).

29. Fersht, A. *Structure and Mechanism in Protein Science: A Guide to Enzyme Catalysis and Protein Folding*, (W. H. Freeman and Company, New York, 1999).

30. *Handbook of Chemistry and Physics*, (CRC Press, Inc., Boca Raton, 1984-85).

31. Rother, D., Poppe, L., Morlock, G., Viergutz, S. & Retey, J. An active site homology model of phenylalanine ammonia-lyase from Petroselinum crispum. *European Journal of Biochemistry* **269**, 3065-3075 (2002).

32. Gloge, A., Langer, B., Poppe, L. & Retey, J. The behavior of substrate analogues and secondary deuterium isotope effects in the phenylalanine ammonia-lyase reaction. *Archives of Biochemistry and Biophysics* **359**, 1-7 (1998).

33. Gloge, A., Zon, J., Kovari, A., Poppe, L. & Retey, J. Phenylalanine ammonia-lyase: The use of its broad substrate specificity for mechanistic investigations and biocatalysis - Synthesis of L-arylalanines. *Chemistry-a European Journal* **6**, 3386-3390 (2000).

34. Ditchburn, R.W. *Light*, (Academic Press, New York, 1976).

35. www.pdr-chiral.com.

36. Stryer, L. *Biochemistry*, (W. H. Freeman and Company, San Francisco, 1975).

37. Bornhop, D.J. et al. Free-solution, label-free molecular interactions studied by back-scattering interferometry. *Science* **317**, 1732-1736 (2007).

38. Swinney, K., Markov, D. & Bornhop, D.J. Chip-scale universal detection based on backscatter interferometry. *Analytical Chemistry* **72**, 2690-2695 (2000).

39. Latham, J.C., Markov, D.A., Sorensen, H.S. & Bornhop, D.J. Photobiotin surface chemistry improves label-free interferometric sensing of biochemical interactions. *Angewandte Chemie-International Edition* **45**, 955-958 (2006).

APPENDIX – PROGRAM CODES IN LabVIEW™

Four different programs are demonstrated:

1) Fourier transform program for BSI with Garry 3000 or Garry 3000SD linear CCD (Ames Photonics)

2) Temperature control program (TCP) for Wavelength Electronics Inc. temperature controller

3) Correlation program (CP) for BSI with 2D CCD

4) Data analysis program for data generated by Fourier transform and correlation programs

Due to the complex nature of the correlation and data analysis programs, the LV code shown has little detail. An electronic copy of the images provides much more information and is available upon request.

1) Fourier transform program for BSI with Garry 3000 or Garry 3000SD linear CCD (Ames Photonics)

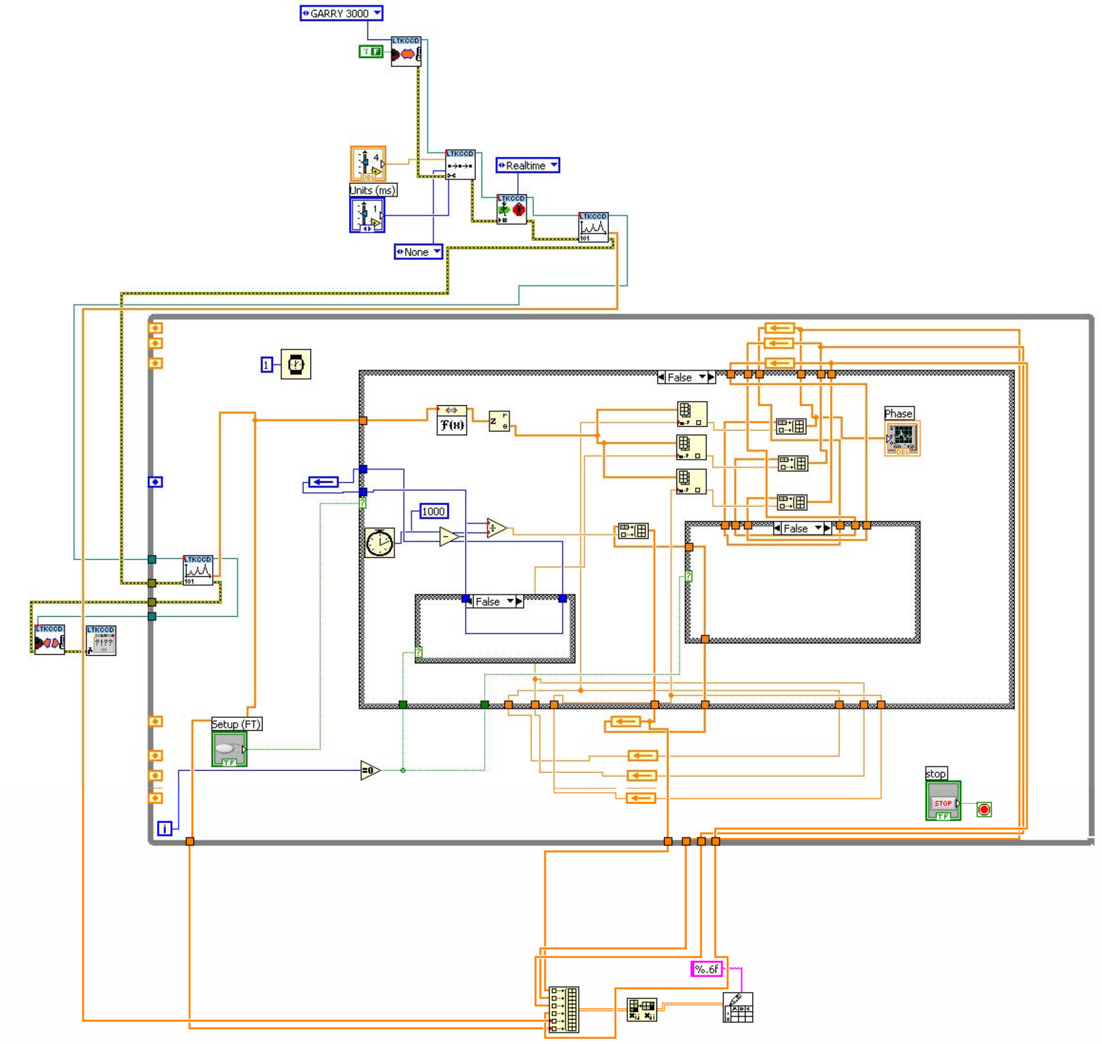

2) Temperature control program (TCP) for Wavelength Electronics Inc. temperature controller

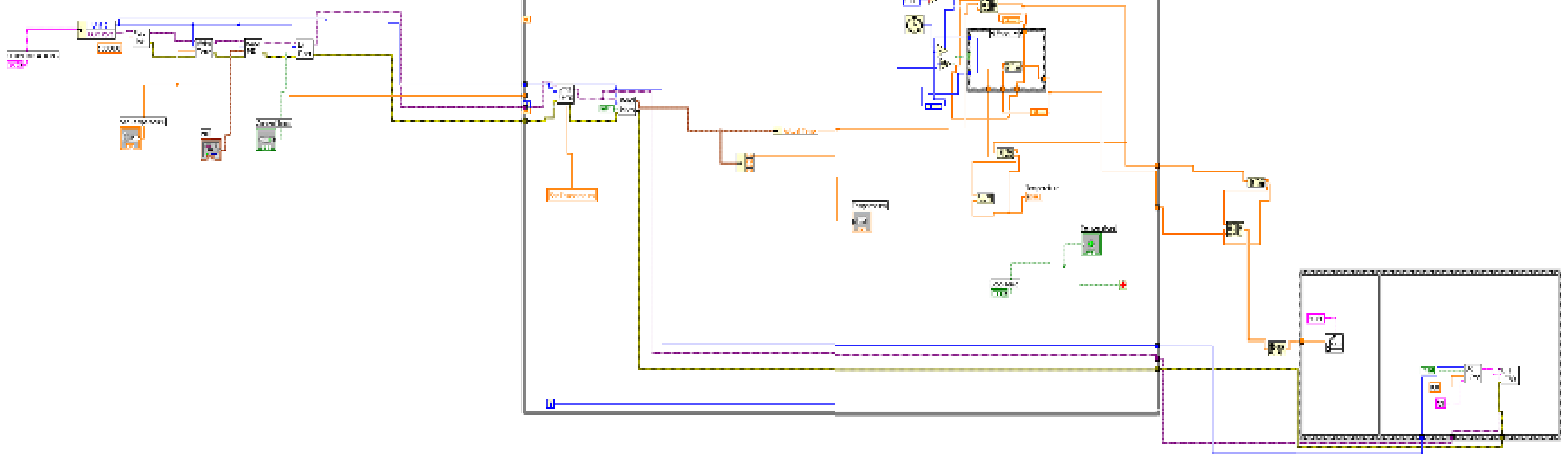

3) Correlation program (CP) for BSI with 2D CCD

CP – Setup false mode (data acquisition and pixel shift calculation)

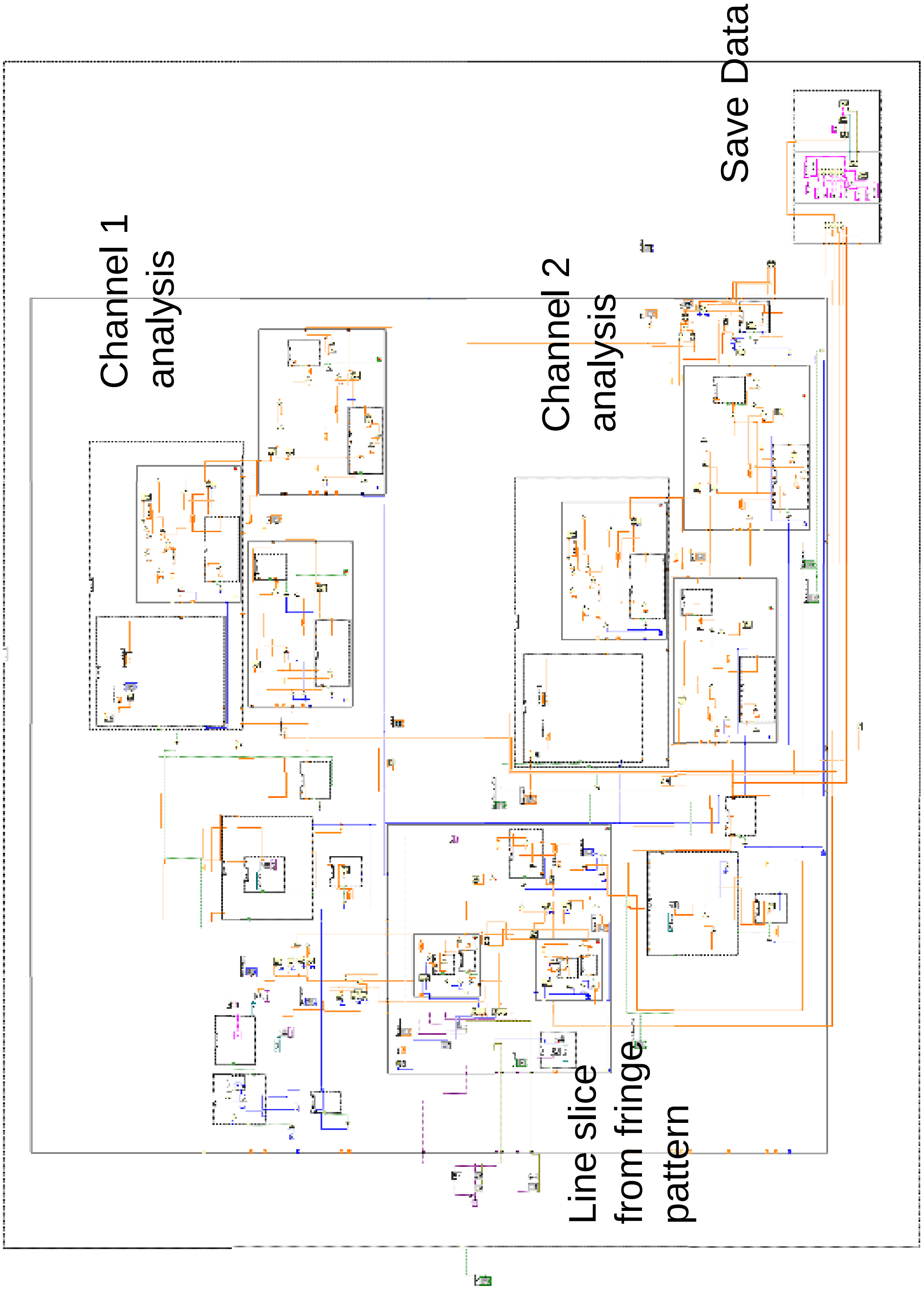

CP – setup true mode

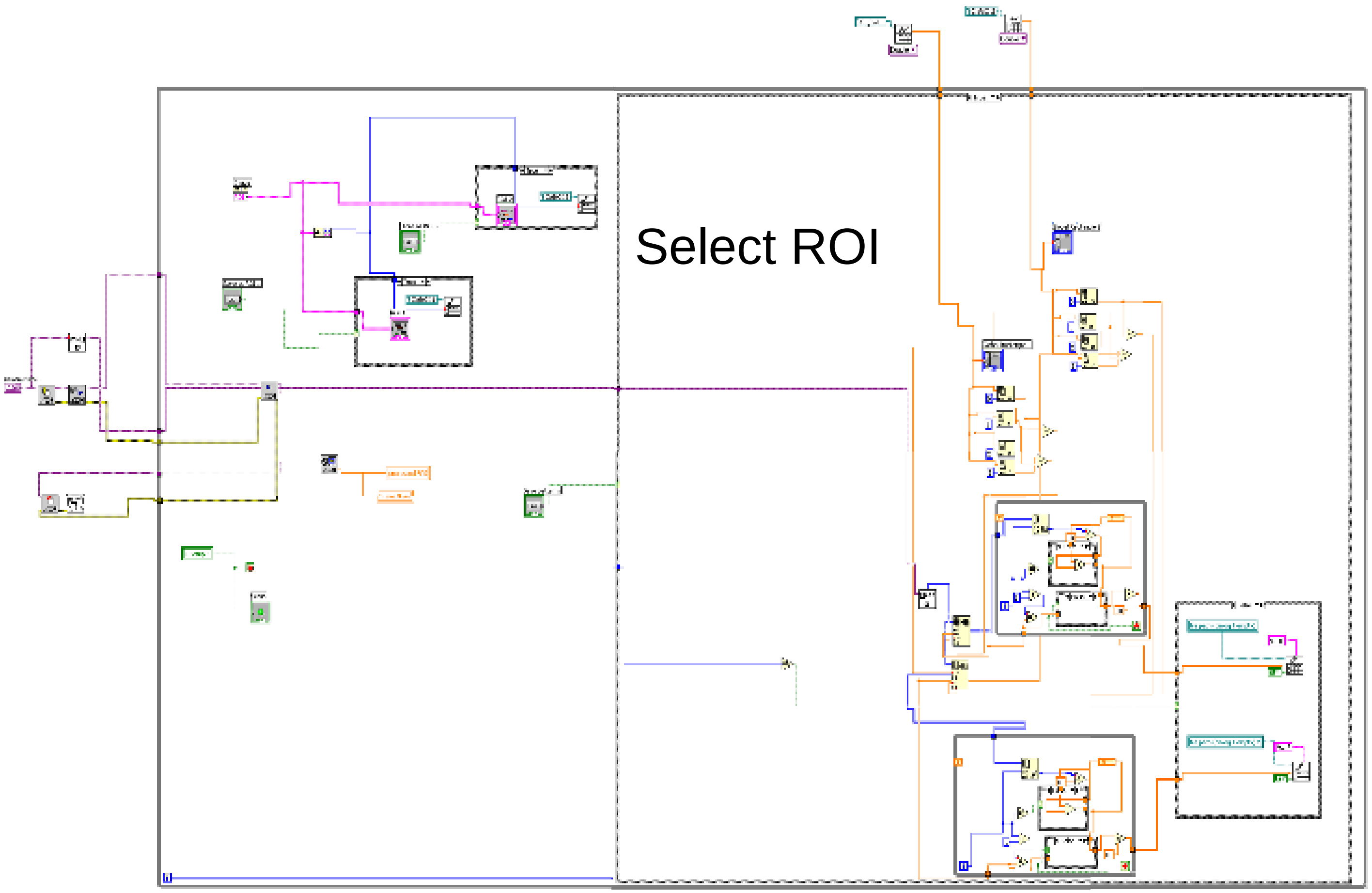

4) Data analysis program for data generated by Fourier transform and correlation programs